Modification of MnO_2-based Cathode Materials for Rechargeable Alkaline Batteries

by

Farhang Nesvaderani

B.A.Sc., The University of British Columbia, 2014

A THESIS SUBMITTED IN PARTIAL FULFILLMENT OF
THE REQUIREMENTS FOR THE DEGREE OF

MASTER OF APPLIED SCIENCE

in

The Faculty of Graduate and Postdoctoral Studies

(Chemical and Biological Engineering)

THE UNIVERSITY OF BRITISH COLUMBIA

(Vancouver)

August 2017

Abstract

Aqueous batteries like the alkaline battery, which utilizes the MnO_2/Zn chemistry, are recently receiving renewed attention due to an urgent desire to develop advanced batteries for storage of energy. MnO_2/Zn batteries offer high energy density, lower cost, and excellent shelf life. The cycleability of such batteries is, however, challenging due to the poor performance of the MnO_2 cathode. Therefore, various phases of MnO_2 materials were synthesized to investigate their cycling performance. A series of electrolytic MnO_2 (EMD) samples were synthesized using different concentrations of sulfuric acid-based electrolysis baths. EMD samples synthesized at a relatively high acidic concentration (2M H_2SO_4), had a 30% higher energy efficiency over a cycling period of 100 cycles and 35% higher capacity at the end of the cycling period. The better cycling performance is attributed to higher surface area, higher structural water content (essential for proton diffusion), and a larger fraction of ramsdellite phase in the 2M EMD structure. Pure ramsdellite MnO_2 was also synthesized and tested. It displayed an improved energy delivery and efficiency over all the EMD samples and its final specific capacity was very comparable to the 2M EMD sample.

An alternative electrolyte solution (zinc sulfate) was examined for the cycling performance MnO_2 versus a zinc electrode. Addition of manganese sulfate to the electrolyte, which is reported to inhibit manganese dissolution during cycling, was also studied. This led to a discovery that the manganese sulfate additive leads to deposition of additional MnO_2 on the cathode substrate during the charge step of the cycling regime. Based on this observation, a novel method of producing EMD was designed in the zinc sulfate electrolyte that provides a milder environment

for producing the material. This form of EMD, named “neutral” EMD or NEMD, exhibits a specific capacity 3x higher than that of commercial EMD when cycled in the zinc sulfate electrolyte. Furthermore, it was possible to retain at least 67-80% of its capacity after 100 cycles. Although MnO_2 cycled in zinc sulfate can only be utilized with low gravimetric loading of the material, this thesis exhibits a possible method of improving this factor.

Lay Summary

The demand for the development of advanced battery systems is growing with the expanding market for technologies that require energy storage (electric vehicle, solar power, etc.). Although Li-ion batteries receive the highest attention, there is an ongoing research on safer and inexpensive alternatives. Alkaline batteries that use abundant resources with low toxicity are considered as an option. Alkaline batteries are, however, not easily rechargeable. This thesis aimed to improve their performance by enhancing the production method of its different components and testing alternative materials used inside the battery system. Results showed that slight adjustments in the production method of certain components can improve performance by up to 30%. The use of alternative materials further improved performance by up to 80%. The research also led to the development of highly rechargeable alkaline batteries that can be produced in a single step without the need to produce the various components separately.

Preface

The work presented in this thesis was conducted under the supervision of Dr. David P. Wilkinson and Dr. Arman Bonakdarpour. Greg Afonso was responsible for the design and manufacturing of the cell hardware used for the experimental work.

Portion of the results from Chapter 3 has been presented at the following conferences and meetings:

- 2015 International Conference on Electrochemical Energy Science and Technology (**EEST 2015** in Vancouver, BC, CA)
- 2016 Pacific Rim Meeting on Electrochemical and Solid-State Science (**Prime 2016** in Honolulu, HI, US)
- 5th Annual Young Electrochemists Symposium (**YES 2016** in Vancouver, BC, CA)

The presented materials at the Prime 2016 was published in the conference proceedings:

- **Nesvaderani, F**., Bonakdarpour, A., & Wilkinson, D. P. (2017). pH-Controlled Synthesis of Electrolytic Manganese Dioxide Materials for Alkaline MnO2/Zn Batteries. *ECS Transactions*, *75*(18), 147-153.

and also in the Electrochemical Society Journal of Electrochemical Society:

- **Nesvaderani, F.,** Bonakdarpour, A., & Wilkinson, D. P. (2017). pH-Controlled Electrolysis of Electrolytic Manganese Dioxide (EMD) for Improved Cycle Life of Rechargeable MnO_2/Zn Batteries. *Journal of The Electrochemical Society*, *164*(4), A810-A819.

A manuscript is also being written for a portion of results from Chapter 4:

- **Nesvaderani, F.,** Bonakdarpour, A., & Wilkinson, D. P. (2017). In- and Ex-Situ Synthesis of Highly Rechargeable Electrolytic MnO_2 in Near-Neutral Electrolytes. *In Progress*

Table of Contents

List of Tables

List of Figures

List of Abbreviations

- **BCE** – Before the Common Era
- **USD** – US Dollar
- **Ni-Cd** – Nickel-Cadmium Battery
- **NiMH** – Nickel-Metal Hydride Battery
- **Li-ion** – Lithium Ion Battery
- **RAM** – Rechargeable Alkaline Manganese Battery
- **BTI** – Battery Technologies, Inc.
- **EMD** – Electrolytic Manganese Dioxide
- **NEMD** – Neutral Electrolytic Manganese Dioxide
- **CMD** – Chemically Synthesized Manganese Dioxide
- **WE** – Working Electrode
- **CE** – Counter Electrode
- **REF** – Reference Electrode
- **PTFE** – Polytetrafluoroethylene
- **CMC** – Carboxymethyl cellulose
- **SRB** – Styrene-Butadiene Rubber
- **TGA** – Thermogravimetric Analysis
- **XRF** – X-Ray Fluorescent
- **XRD** – X-Ray Diffraction
- **BET** – Brunauer Emmett Teller
- **BJH** – Barrett-Joyner-Halenda
- **EIS** – Electrochemical Impedance Spectroscopy
- **CPE** – Constant Phase Element
- **EE** – Energy Efficiency
- **DoD** – Depth of Discharge
- **CD** – Current Density
- **Pr** – Pyrolusite Ratio
- **DP** – Differential Peaks
- **CV** – Cyclic Voltammetry

List of Symbols

Symbol	*Definition*	*Unit*
V	Voltage	V
V_{OC}	Open Circuit Voltage	V
V_{Cell}	Voltage of Cell	V
$E^0_{Cathode}$	Cathode Half Reaction Potential	V
E^0_{Anode}	Anode Half Reaction Potential	V
V_{SHE}	Voltage vs. Standard Hydrogen Electrode	V
E	Energy	Wh
I	Current	mA
t	Time	h
dt	Change in Time	h
Q	Capacity	mAh
dQ	Change in Capacity	mAh
e^-	Electron	--
g_{EMD}^{-1}	Per Gram of EMD	g
g_{MnO2}^{-1}	Per Gram of MnO_2	g
C_{H2SO4}	Concentration of Sulfuric Acid	M
SA_{EMD}	Surface Area of EMD	$m^2\ g^{-1}$
$W_{Structural}$	Percentage of Structural Water	%
R_{ct}	Charge Transfer Resistance	Ω
R_s	Series Resistance	Ω
f	Frequency	kHz

Acknowledgments

After graduating from my bachelor's degree, I was still unsure about direction of my career. That, however, quickly changed when I started my Master's program under the supervision of Dr. David Wilkinson and Dr. Arman Bonakdarpour. Their passion for the research and innovation truly made me appreciate the importance of this field of study and their continuous support and guidance created an environment where I could learn and thrive in. So for all that you have done – Thank You!

I have also been lucky to have had the opportunity to work with very talented colleagues during these past years. I wish to thank Greg Afonso and Sean Mehta for their contributions to this research and the co-op students (Faye, William, Shirley, and Beichen) for their help in this project.

Lastly, I need to express my deepest gratitude to my parents for their love and never-ending support, without which, I would not have been able to be where I am right now.

Chapter 1. Introduction

1.1 Energy Storage Technologies – Batteries

1.1.1 Overview of Different Battery Technologies (Primary and Secondary)

In the 1930s, a clay jar dating back to 250 BCE was discovered in an Iraqi city just outside of Baghdad (see Figure 1.1). The jar contained a copper metal and an iron rod that could spontaneously form electricity when filled with a vinegar solution [1]. Therefore, the apparatus was appropriately named the Baghdad Battery and was believed to be the first form of an electrical energy storage device for many years [1]. However, that theory has since been debunked due to the obvious lack of electrical devices 2000 years ago [1].

The first recorded milestone in batteries was set in 1800 by Alessandro Volta who invented the first wet battery known as the voltaic pile. The pile consisted of stacks of copper and zinc electrodes separated by pieces of carboard soaked in saltwater that acted as the electrolyte [2]. This invention was later improved in 1836 by John F. Daniell whose cell consisted of the electrodes immersed into their own distinct electrolyte solution separated by a permeable barrier [3]. The next major battery breakthrough was made by Georges Leclanché who invented the first form of an MnO_2/Zn cell in 1866. Leclanché's invention was later transformed into the first commercialized dry battery (zinc-carbon) in the early 1900's [4]. The beginning of the mass production of dry batteries introduced portable and convenient energy storage devices into people's lives. Therefore, the development of other non-rechargeable batteries was followed. Table 1.1 gives an overview of some of the commercialized single-use batteries available today

Figure 1.1 The Baghdad Battery. [5]

Table 1.1 Overview of available commercialized primary batteries. [2]–[4]

Battery Type	*Specific Energy (Wh/kg)*	*Description*
Carbon-Zinc (MnO_2/Zn)	50	Used for common household items. It is safe and cheap but has low energy density.
Alkaline (MnO_2/Zn)	150	It is used in similar applications to the carbon-zinc cell but has a higher energy density. It is inexpensive, available in many different geometries, and has a high shelf-life.
Lithium Primary (Li/MnO_2) [6]	300	High specific energy and capable of handling high drain rates. However, very expensive and less safe than MnO_2/Zn.
Zinc-Air Primary (Zn/O) [7]	500	Extremely high energy density, low cost, high shelf life. However, difficult to scale up due to oxygen acting as a limiting reagent. The most common type is the button sized cell used mostly in watches or hearing aids.

The first form of a secondary (rechargeable) battery was invented in 1859 by Gaston Planté who developed the lead-acid technology. A lead-acid cell consists of lead sulphate/lead oxide electrodes and sulfuric acid electrolyte solution. Despite the materials' high toxicity and the cell's low energy density, lead-acid batteries are still used today because the impressive reversibility of the reactions involved and the ability of the battery to handle high currents. Lead-acid batteries are mostly used in automotive application but are also used in grid and power backup systems leading to a huge global market (~50 billion USD in 2014) [8].

Following the lead-acid, the nickel–cadmium chemistry was invented in 1899. However, other well-known rechargeable batteries, i.e., nickel–metal hydride (1989) and lithium-ion (1990) are relatively recent developments [9], [10]. Table 1.2 gives an overview of some of the commercialized rechargeable batteries available today.

Table 1.2 Overview of available commercialized rechargeable batteries. [8]–[10]

Battery Type	*Specific Energy (Wh/kg)*	*Description*
Lead-Acid (Pb/PbO_2)	40	Used mainly as car batteries. High cycleability, but low energy density and efficiency, and high toxicity.
Nickle-Cadmium (Ni/Cd)	60	Used in landline telephones and power tools. High cycleability, but low energy density and high toxicity.
Nickel-Metal Hydride (NiMH)	80	Less toxic alternative to Ni-Cd with a higher energy density. However, more expensive to produce.
Lithium ion (Li-ion)	150	Used in electric vehicles, cell phones, laptops, and many other applications. High cycleability and high energy density. Expensive due to rarity of lithium and the requirement for a highly-engineered design due to the reactivity of lithium.

Currently, there is a great demand for development of advanced batteries for energy storage applications from portable (~5-50 Wh/year) and vehicular applications (~ 20 kWh/100 km) to large scale (grid-level) applications (~ 2000 GWh) [11]–[16]. In particular, the use of advanced Li-ion batteries for the electric vehicle market is anticipated to grow 20-fold by 2020 [17]. Although in general Li-ion batteries receive the highest attention and demand [18]–[20], aqueous batteries like redox-flow, lead-acid, and alkaline batteries are also under significant research [21]–[23]. Furthermore, a number of novel battery-capacitor approaches have been recently reported [24], [25]. These hybrid approaches combine the advantages of batteries (high energy density) and those of capacitors (rapid charge/discharge rates and long cycle life). Among the various battery technologies, the MnO_2/Zn alkaline chemistry, which forms the basis of the primary batteries, is receiving renewed attention with respect to rechargeable batteries. Rechargeable Alkaline Manganese (RAM) batteries could offer high energy density (see Figure 1.2), lower cost, and excellent shelf life in comparison to the widely commercialized batteries currently available. In particular, the cathodic materials or Electrolytic Manganese Dioxide (EMD or γ-MnO_2), has a low production cost, low toxicity, high capacity, low drain rate, and it is an abundant natural resource. The cycleability of the EMD, however, remains a challenge despite many efforts in the past to improve it [23], [26]–[28].

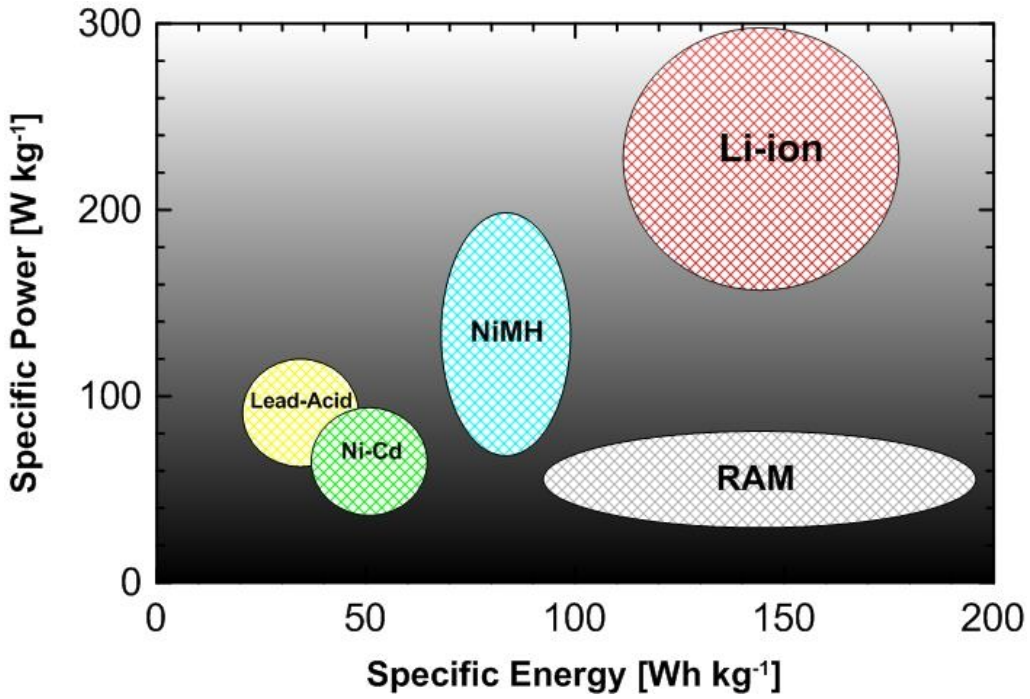

Figure 1.2 Specific energy and power comparison of different battery technologies. [29]

1.1.2 Basic Operation of an Electrochemical Cell

An electrochemical cell consists of a cathode and anode electrode pair with an ion-conducting solution (electrolyte) located inside the cell to carry out the oxidation (loss of electron(s) at anode) and the reduction (gain of electron(s) at cathode) reactions [30]. Figure 1.3 and Equations 1.1-1.3 display the basic operation of a galvanic cell (being discharged) using the MnO_2/Zn reaction as an example. In this case, zinc metal (anode) reacts with a hydroxide group, which is available in the electrolyte solution (i.e., potassium hydroxide – KOH), and oxidizes to $Zn^{(+2)}O$, producing an electric current which passes through an external load towards the cathode to reduce the $Mn^{(4+)}O_2$ (cathode) into $Mn^{(3+)}OOH$ [26].

$MnO_2 + H_2O + e^- \leftrightarrow MnOOH\ (groutite) + OH^-$ $E^o_{Cathode} = 0.36\ V_{SHE}$ **Equation 1.1**

$1/2Zn + OH^- \leftrightarrow 1/2ZnO + 1/2H_2O + e^-$ $E^o_{Anode} = 1.248\ V_{SHE}$ **Equation 1.2**

$1/2Zn + MnO_2 \leftrightarrow 1/2ZnO + MnOOH$ $E^o_{Cell} = 1.608\ V_{Cell}$ **Equation 1.3**

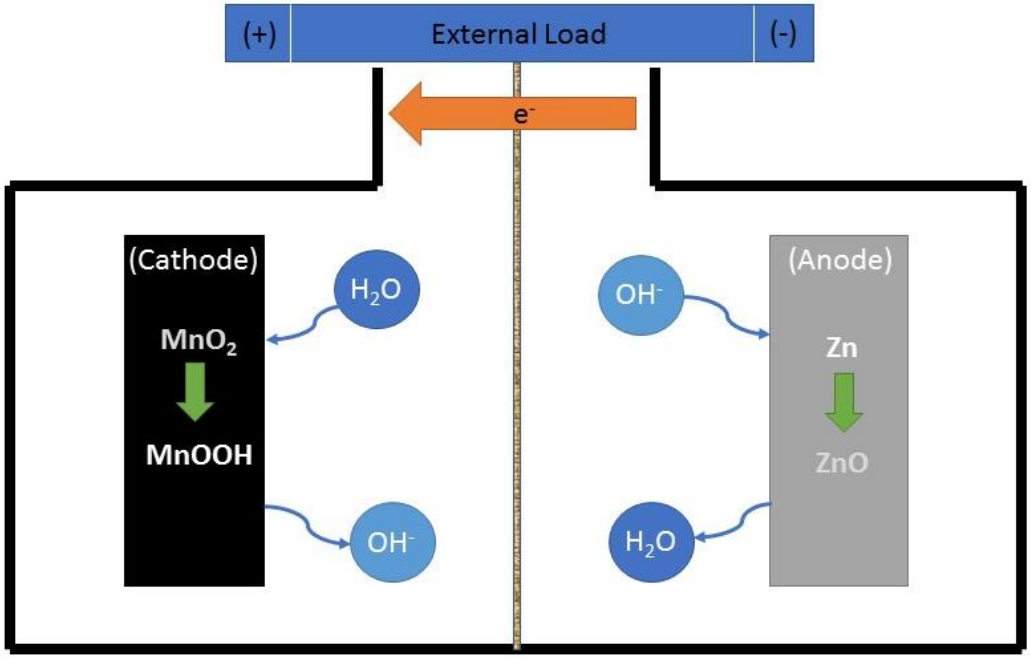

Figure 1.3 Working principles of an MnO_2/Zn cell.

During the discharge or charge reactions, a current (I) flows through an external circuit for a certain amount of time (t), during which time the cell voltage (V) is decreased or increased as the process continues [30]. The amount of charge (Q = current x time; measured in mAh) and electrical energy (E = potential x charge; measured in Wh) obtained or provided can be calculated using Equations 1.4-1.5:

$Q = \int I * dt$ **Equation 1.4**

$E = \int V * dQ$ **Equation 1.5**

1.1.3 Economical and Resource Implications

Figure 1.4 displays the elemental abundance and current market prices (2016) of the active materials used in various commercialized rechargeable batteries as well as the rechargeable alkaline battery [31]–[33].

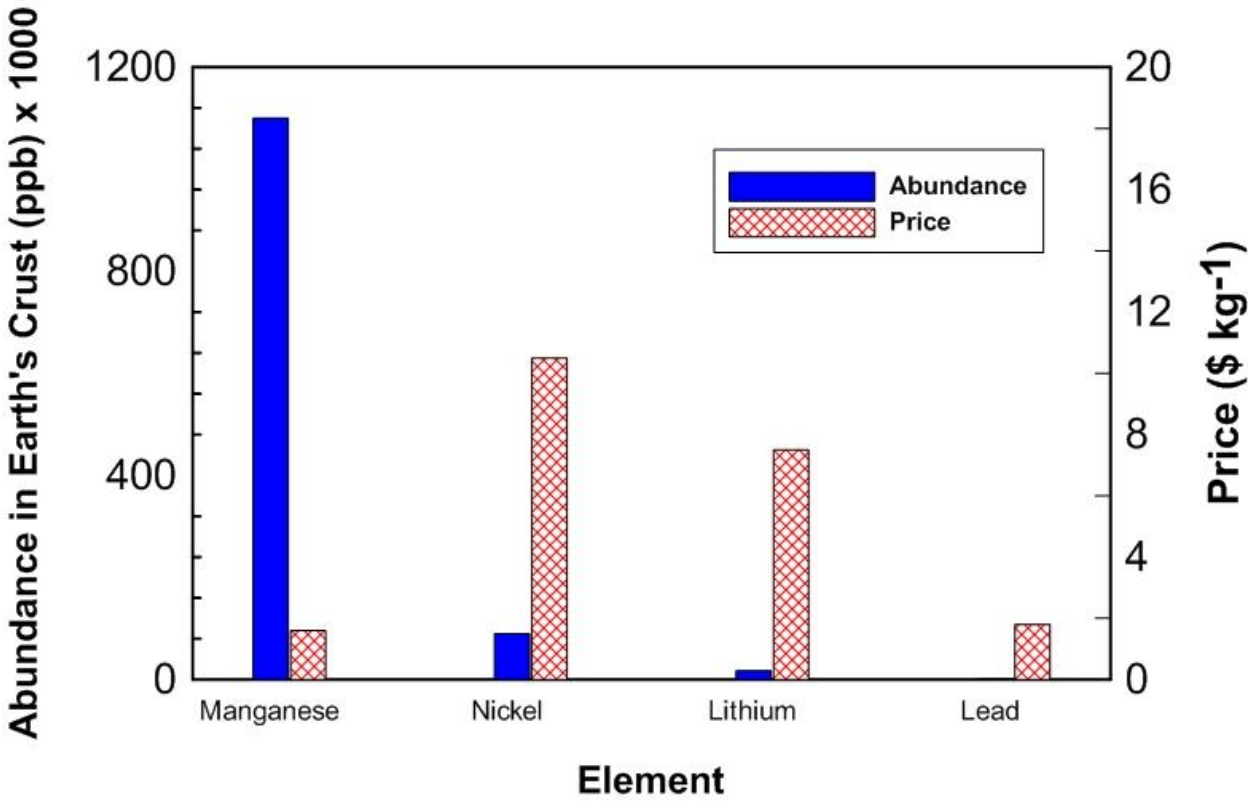

Figure 1.4 Abundance and price of elements used in various rechargeable battery technologies. [31]–[33]

Looking at these plots, the benefits of manganese-based energy storage devices are evident. However, for a rechargeable battery to be economically viable, hundreds to thousands of cycles are required [34], and the cycling performance of alkaline MnO_2 batteries has been limited to 100 cycles or less, with its initial capacity diminishing over its lifetime by approximately 80% in

an exponential manner [35]. Moreover, RAM batteries can only be cycled at relatively low C-rates. The C-rate describes the rate used to discharge or charge a battery based on its theoretical capacity. For example, a 1C discharge rate for a battery with a theoretical capacity of 100 mAh g^{-1} means applying 100 mA of current to discharge the battery in one hour. A rate of C/10 means discharging or charging in ten hours and a rate of 2C means discharging or charging in thirty minutes. While Li-ion and NiMH batteries can be cycled at C-rates as high as 5C, RAM has a maximum rate capability of C/2 meaning it can't be used in high power applications. Table 1.3 displays the performance of commercial rechargeable batteries [36]. Lithium- and nickel-based batteries offer hundreds of cycles with minimum energy loss as well as higher current loading capability, which make them more widely functional for many different applications: electric vehicles, electric grids, etc. However, RAM batteries are still of interest due to their lower cost, toxicity [26], and reactivity (excellent safety) [18]. These batteries are ideal for use in small personal electronics and applications that don't require high current loads. Furthermore, due to the comparable cost of the RAM battery to lead-acid per cycle, rechargeable alkaline batteries can become a more viable option especially for backup systems and for energy and low-demand applications.

Table 1.3 Comparison of different rechargeable battery technologies. [36]

Battery Type	Avg. Energy Density (Wh kg^{-1})	No. of Cycles	Max. C-rate	Price per Cycle (¢ $Cycle^{-1}$)
Li-ion	150	500-1000	2C	14
NiMH	100	300-500	5C	12
Lead-Acid	40	200-300	5C	10
RAM	80	>100	C/2	10-50

1.2 Alkaline Batteries as a Rechargeable Technology

1.2.1 History and Scientific Principles of Alkaline Batteries

Alkaline batteries entered the primary battery market in the 1960s as the higher energy density successor to the zinc-carbon cell. These new MnO_2/Zn batteries used a potassium hydroxide electrolyte, as opposed to ammonium and/or zinc chloride electrolyte, and utilized high surface area zinc powder for the anode [4], [37].

RAM batteries were introduced into the market in the 1970s by Union Carbide Corp., but were quickly taken down due to poor performance [26], [37]–[39]. Furthermore, gas evolution can occur in aqueous batteries at very high potentials while charging. Since early RAM batteries did not have any control parameters for the charging of the battery, safety concerns also led to its market failure [26], [37]–[39]. Research on the technology was however later continued in the 1980s at the Technical University of Graz, Austria, and it was soon commercialized by Battery Technologies, Inc. (BTI) in Canada. The new RAM batteries were very similar to primary alkaline batteries except that each cell contained a lower ratio of zinc to manganese. What made these RAM cells more rechargeable was that zinc was available in limited amounts and therefore it couldn't allow for the discharge of MnO_2 beyond its 1^{st} electron reduction reaction.

1.2.2 Challenges with RAM

Discharging an alkaline manganese cell beyond its first electron reaction creates irreversible phases of manganese oxide. Hausmannite (Mn_3O_4) and bixbyite (Mn_2O_3) form at a pH of 14 according to Equations 1.6-1.7 [26], [39].

$3MnOOH + e^- \rightarrow Mn(OH)_2 + OH^- + Mn_2O_3\ (bixbyite)$ $E_{Cathode}$ = -0.25 V_{SHE} **Equation 1.6**

$3MnOOH + e^- \rightarrow H_2O + OH^- + Mn_3O_4(hausmannite)$ $E_{Cathode}$ = -0.29 V_{SHE} **Equation 1.7**

The previous equations indicate that irreversible species are formed at theoretical cell potentials below approximately 1.0 V_{Cell}. Therefore, a voltage constraint is implemented when cycling RAM cells to avoid capacity fade. However, at the potentials and pH levels that RAM cells operate at, as indicated in Figure 1.5 by the red line, the bixbyite species is also stable. Therefore, reactions to form irreversible manganese oxide phases can occur at higher potentials where the groutite product forms.

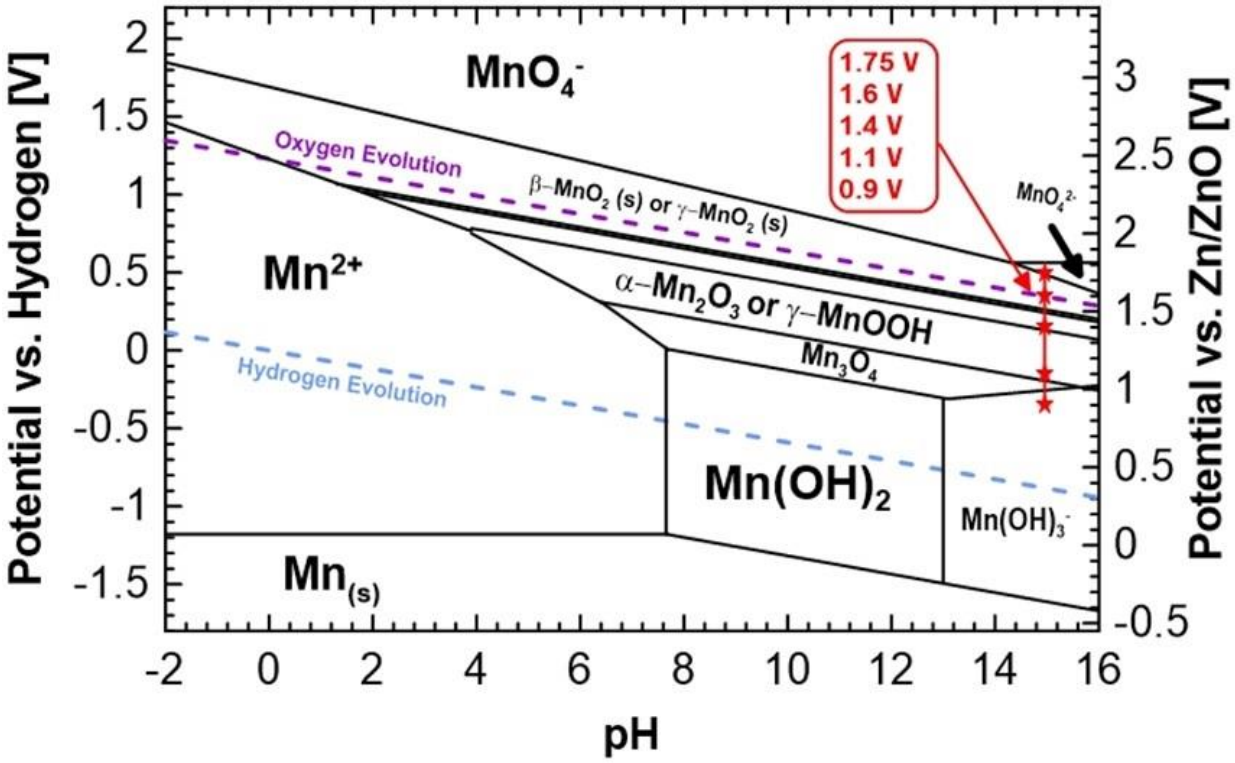

Figure 1.5 Modified Pourbaix diagram of manganese.

Furthermore, side reactions can also occur between manganese and zinc spices. The main side reaction forms a zinc manganese oxide complex (heterolyte – $ZnMn_2O_4$), that is irreversible and leads to additional capacity loss (see Equation 1.8).

$$Zn + 2MnO_2 \rightarrow ZnMn_2O_4$$ **Equation 1.8**

Problems that lead to capacity loss may also occur during the charging of a RAM cell. If the cell potential exceeds 1.85 V_{Cell}, the following reactions could occur, which would result in the formation of soluble manganate(VI) (MnO_4^{2-}) (see Equations 1.9-1.10) and permanganate species (MnO_4^-) (see Equations 1.11-1.12). Permanganate is a strong oxidizing agent that can split water and generate oxygen. This would also cause safety concerns due to the possible expansion of the cell.

$$MnO_2 + 4OH^- \rightarrow MnO_4^{2-} + 2H_2O + 2e^-$$ E_{Anode} = -0.62 V_{SHE} **Equation 1.9**

$$5MnO_4^{2-} + 8H^+ \rightarrow 4MnO_4^- + Mn^{2+} + 4H_2O$$ **Equation 1.10**

$$MnO_2 + 4OH^- \rightarrow MnO_4^- + 2H_2O + 3e^-$$ E_{Anode} = -0.60 V_{SHE} **Equation 1.11**

$$4MnO_4^- + 4H^+ \rightarrow 4MnO_2 + 2H_2O + 3O_2$$ **Equation 1.12**

Lastly at very high potentials (above 2 V_{Cell}), hydrogen gas can start forming at the anode which would cause further safety concerns (see Equation 1.13).

$$2H_2O + 2e^- \rightarrow 2OH^- + H_2$$ $E_{Cathode}$ = -0.828 V_{SHE} **Equation 1.13**

The aforementioned reactions indicate that with careful charge/discharge control methods, a fully rechargeable RAM cell should be possible. However, in the most ideal situation a cycling performance similar to the curve shown in Figure 1.6 can only achieved [26], [38], [39].

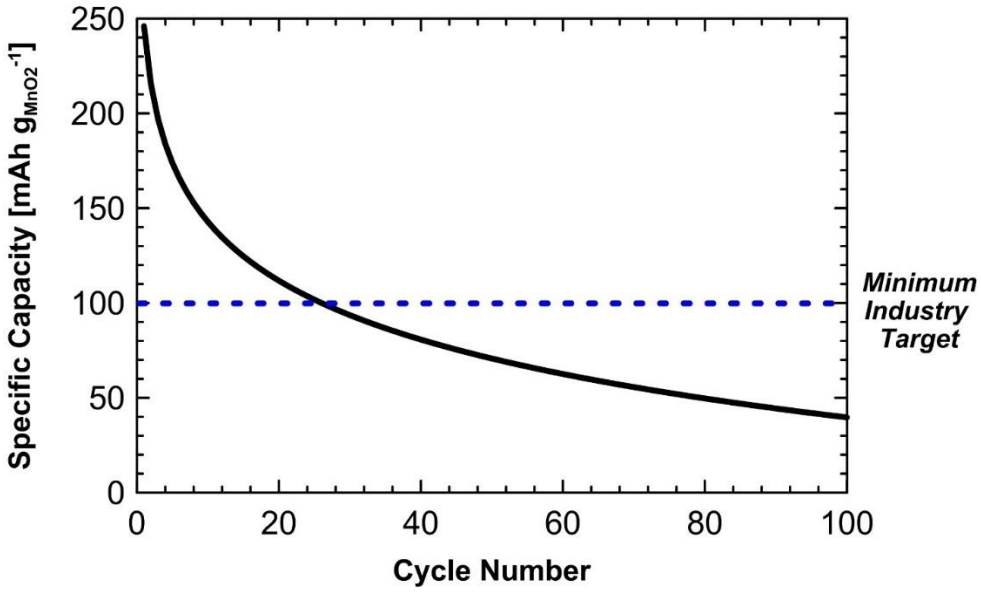

Figure 1.6 Cycling performance of a typical commercial RAM cell.

Much work has been dedicated to understanding the failure modes of the RAM cell [23], [26], [38]–[41]. In-situ and post cycling analyses of the cathode material indicate that irreversible phases do form regardless of the voltage constraints placed on the battery. A recently published work on analysing the electrolyte of cycled RAM cells does argue that dissolved manganese (that leads to loss of active cathode material) is the main culprit of capacity fade [42]. As a result of these investigations, many solutions to creating a rechargeable RAM cell have been proposed in literature.

1.2.3 Recent Advancements

A number of different approaches have been examined for improving the rechargeability of the RAM battery by: 1) incorporating chemical additives into the cathode [26], [38], [43], [44], 2) modifying the synthesis parameters of EMD for improving its physical and chemical properties [40], [45]–[51], and 3) using alternative MnO_2 products and phases or electrolyte solutions [41], [44], [52]–[55].

Alkaline earth metal additives such as $BaSO_4$, $Ba(OH)_2$, MgO, etc., have for instance been investigated as potential cathode additives [26], [38], [43], [44] but, their impact on cycling life is marginal [39]. In particular, $BaSO_4$ has been hypothesized to integrate into the lattice structure of EMD and act as a stabilizing agent of the reversible phases during the discharge reaction [26], [38]. $Ba(OH)_2$ as an additive has shown to reduce the dissolution of manganese ion and thus improve cycling in the short term, however, no long term cycling has been reported on this additive [43]. MgO has been reported to suppress the side reaction between manganese and zinc, thus, improving the capacity fade by 25% (again in short term cycling) [44]. Other cathode additives involving metal ions such as titanium, bismuth, silver, and cesium have also been investigated. Many different combinations of TiS_2, TiB_2 and Bi_2O_3 additives have been tested by Minakshi *et al.* and Raghuveer *et al.* [41], [52], [56], [57]. Small amounts of these additives (2-5%) have shown to improve cycling of EMD by retaining 50% more capacity after 25 cycles compared to EMD cycled without any additives. Similar arguments have been made for the benefits of these additives, i.e. inhibition of manganese dissolution and irreversible phases (hausmannite) [56]. Other more complex and rarer metal salts have furthermore been tested as potential additives.

These include Ag_3BiO_x [58] $BaBiO_3$ or $Ba_{0.6}K_{0.4}BiO_3$ [59], $NaBiO_3$ [60], and CeO_2 [53], [54] but, none are superior to the aforementioned chemicals in terms of capacity fade. $NaBiO_3$ [60] and CeO_2 [53], [54] have been argued to improve energy efficiency and columbic efficiency of the RAM battery, respectively, but have displayed no further benefits.

Table 1.4 Comparison of various cathode additives for RAM.

Additive	No. of Cycles	Initial Capacity (mAh g^{-1}_{EMD})	Final Capacity (mAh g^{-1}_{EMD})	Source
$BaSO_4$ (5 wt%)	25	190	125	[38]
MgO (2 wt%)	25	196	140	[44]
BaO (2 wt%)	25	265	106	[44]
$Ba(OH)_2$ (2 wt%)	10	242	173	[43]
Bi_2O_3 (5 wt%)	30	180	100	[56]
TiS_2 (1 wt%)	30	200	125	[56]
TiB_2 (1 wt%)	30	175	115	[56]
Bi_2O_3 (4.5 wt%) + TiB_2 (0.5 wt%)	30	210	130	[56]
Bi_2O_3 (4.5 wt%) + TiS_2 (0.5 wt%)	30	165	125	[56]
Ag_3BiO_x (5 wt%)	20	145	110	[58]
$Ba_{0.6}K_{0.4}BiO_3$ (5 wt%)	30	175	125	[59]
$BaBiO_3$ (5 wt%)	30	200	125	[59]
$NaBiO_3$ (3 wt%)	20	260	75	[60]
CeO_2 (2 wt%)	40	155	135	[54]

Alternative electrolyte solutions have also been investigated as a method of improving rechargeability. LiOH and NaOH electrolytes have been investigated to study the effect of other metal hydroxides on the reversibility of EMD [55], [61]–[63]. Although the irreversible manganese oxide phases do still form in presence of LiOH and NaOH, the majority of the discharged phases found ($NaMnO_2$ and $LiMnO_2$) are considered to be reversible [55], [62]. In

order to limit the reaction that creates irreversible phases (see Equations 1.6 and 1.7), the additives listed in Table 1.4 are utilized in conjunction with these electrolytes [41], [44], [52]–[55]. A summary of the findings mentioned is listed in Table 1.5.

Table 1.5 Comparison of cycling performance of RAM using alternative electrolytes.

Electrolyte	No. of Cycles	Initial Capacity (mAh g^{-1}_{MnO2})	Final Capacity (mAh g^{-1}_{MnO2})	Source
KOH (9M)	25	175	75	[38]
LiOH (7M)	50	150	70	[55]
NaOH (7M)	25	225	175	[62]

Other methods of reducing the capacity loss have been to synthesize altered EMD products. As mentioned before, there has been limited work on the use of chemically produced MnO_2 (CMD) in alkaline batteries. Therefore, most of the research found in literature focus on using EMD as the active material in RAM cells. The most common structures of manganese dioxides used in electrochemical storage are discussed in the next section.

1.3 Manganese Dioxide

1.3.1 Overview of Various Crystal Structures and Applications

MnO_2 has a number of applications in the field of electrochemistry, e.g., alkaline batteries [23], lithium batteries [64], supercapacitors [65], catalyst for oxygen reduction [66], etc. MnO_2 is composed of MnO_6 octahera units (1.89 Å in length) arranged in different ways leading to the numerous crystal structures of the compound, some of which include: α-, β-, R-, γ-, δ-, and λ-MnO_2 (see Figure 1.7) [67]. These structures are identified by the size of the "tunnels", i.e., spaces

between the rows of connected octahedra. For example, β- and R-MnO_2 (known as pyrolusite and ramsdellite, respectively) are clustered to form one dimensional 1 x 1 and 2 x 1 tunnels of MnO_6 octahera units, respectively. α-MnO_2 (hollandite) forms equal numbers of one dimensional 1 x 1 and 2 x 2 tunnels. The δ-MnO_2, or birnessite, phase consists of sheets of MnO_6 octahera units separated by an approximate distance of 7 Å. λ-MnO_2, or spinel, is a three-dimensional MnO_2 phase consisting of uniform and complex tunnelling networks. γ-MnO_2, which is the phase of EMD, is an intergrowth of the β- and R-MnO_2 phases resulting in a highly disordered structure, which has been an ideal phase for alkaline batteries.

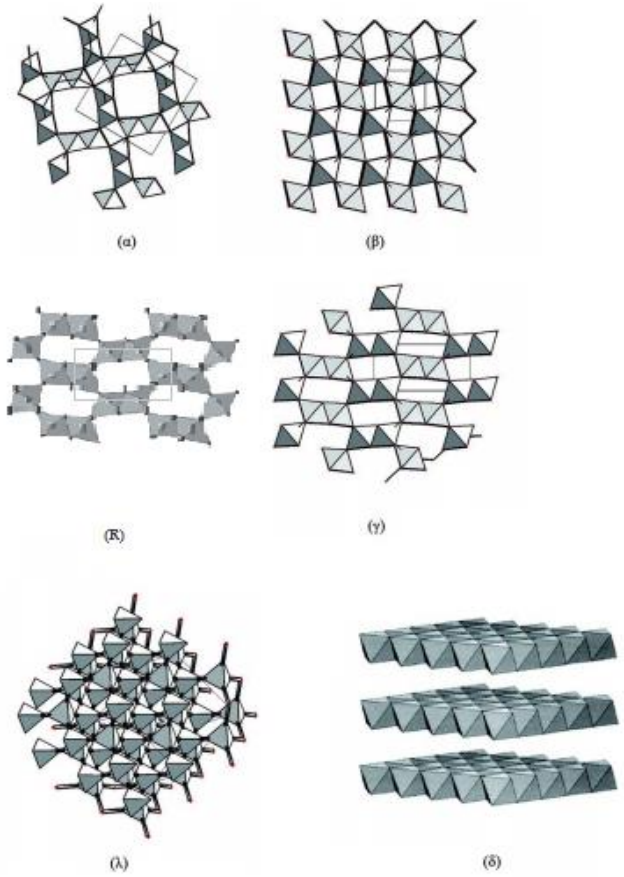

Figure 1.7 Various phases of MnO_2: (α) hollandite, (ß) pyrolusite, (R) ramsdellite, (γ) EMD, (λ) spinel, and (δ) birnessite. [67]

The various phases can be shaped into different morphologies (micro- to nano- scale) suitable for different applications. For example, as shown in Figure 1.8, hollandite can form nanowires and nanofibers (or nanorods). EMD usually forms agglomerated microflakes and birnessite can form flower shaped nano- or micro-spheres. All morphologies can be altered through varying the synthesis methods [68]–[70].

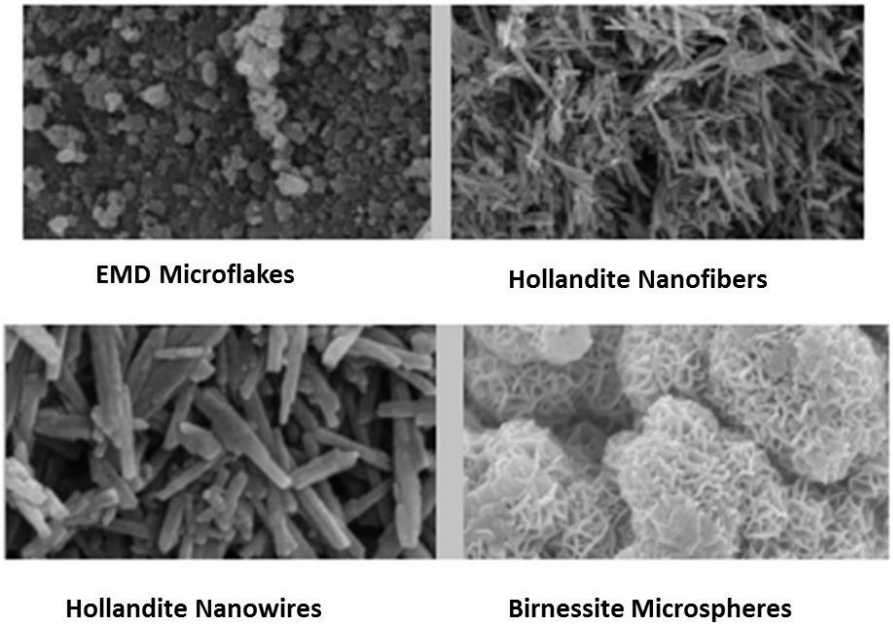

Figure 1.8 Morphologies of various MnO_2 products. [68]–[70]

Hollandite, birnessite, and spinel MnO_2 have channels large enough for the intercalation and deintercalation of potassium, sodium, and lithium ions, and can therefore be used for supercapacitor or lithium-ion battery application [67], [71]. Manganese oxide composites with other metal ions structured into nanorod spinel or nanosphere birnessite compounds are used as cathode materials for Li-ion batteries as these materials can be easily lithiated and delithiated with a relatively high degree of rechargeability while maintaining structural integrity [64], [71].

As mentioned, alkaline MnO_2/Zn batteries use electrochemically produced γ-MnO_2. The 1 x 1 and 1 x 2 tunnels of this phase allow for the intercalation/deintercalation of protons during the discharge/charge processes. Ruetschi *et al.* [72] have reported that EMD is highly disordered and it consists of Mn^{4+} vacant sites (that are occupied by protons known as Ruetschi protons) and partially reduced manganese (Mn^{3+}) ions (that posses a proton, known as Coleman protons, for charge balance). These protons inside the structure form hydroxyl groups with the neighbouring oxygen atoms (also known as "structural water") (see Figure 1.9). Proton intercalation/deintercalation is believed to facilitated in the EMD phase because of the presence of these structural waters [72]–[75].

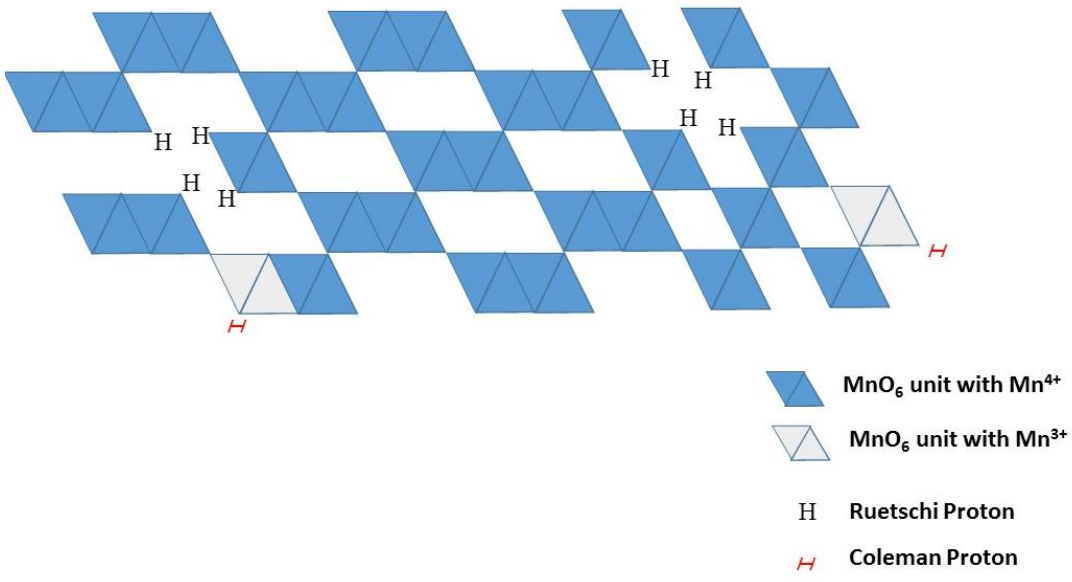

Figure 1.9 Ruetschi's interpretation of EMD.

The figure above can also be represented as the following structural formula:

$$Mn^{4+}_{1-x-y} \cdot Mn^{3+}_{y} \cdot O^{2-}_{2-4x-y} \cdot OH^{-}_{4x+y}$$

where x and y correspond to the fraction of missing Mn^{4+} and Mn^{3+} present ions. The aforementioned protons (x = Ruetschi proton and y = Coleman proton), which form OH^- complexes provide a proton bridge and thus increase the rate of proton diffusion into the lattice [72]–[75].

It is also important to mention that the defect and ramsdellite portions of EMD are the primary sources of discharge/charge capacity. The defect and ramsdellite sites have shown to reduce at potentials above -30 mV vs. Hg/HgO. The pyrolusite phase starts to reduce at lower potentials (≤ -30 mV vs. Hg/HgO or ≤ 1.2 V vs. Zn/ZnO), where the second (undesirable) electron discharge is approached [76], [77].

1.3.2 Synthesis and Properties of EMD

EMD is prepared by the oxidation of Mn^{2+} to Mn^{4+} in an electrolyte consisting of $MnSO_4$ salt and H_2SO_4 acid. The anodic and cathodic reactions are:

$$Mn^{2+} + H_2O \rightarrow MnO_2 + 4H^+ + 2e^- \qquad E = 1.224\ V_{SHE} \qquad \textbf{Equation 1.14}$$

$$2H^+ + 2e^- \rightarrow H_2 \qquad E = 0.000\ V_{SHE} \qquad \textbf{Equation 1.15}$$

Deposition parameters such as the current density, bath temperature, concentration of the salts, and the acid type all impact the EMD's physical properties such as surface area, porosity, and water content which in turn affect the electrochemical properties [40], [45]–[51].

Adelkhani and Ghaemi have reported the effect of pH on the characteristics of EMD in several papers [40], [45], [47] In one study, pH values of 2 and 5 were tested, and it was found that EMD

synthesized at the lower pH of 2 exhibits a lower proportion of the pyrolusite phase (lower Pr) [40]. Although a more morphologically uniform EMD material is obtained from the higher pH level of 5, the sample synthesized at a pH of 2 was shown to have better rechargeability. Adelkhani's subsequent and more comprehensive reports on the effect of pH do confirm the decreasing level of pyrolusite phase growth at lower pH levels [45], [47]. However, the results show that an improved EMD product, in terms of surface area and total pore volume, is synthesized at higher pH levels.

The same researchers have also investigated the effect of temperature [46], [50]. EMD with higher crystallinity was obtained at high temperatures (above 100 ^{o}C) inside a pressurized reactor [50]. The same EMD products were found to have superior performance in RAM cells. Attempts to decrease the reaction temperature without the compromise of structural integrity has been done by implementing pulsed current deposition methods. It was still found that increased temperatures in those systems (60 ^{o}C vs 80 ^{o}C) produce a more rechargeable EMD [46]. However, further increases in temperature reduced the rechargeability and structural water content (4% water at 98 ^{o}C vs 12% water at 80 ^{o}C). A combinational study of acid concentration and temperature conducted by Dutra *et al.* has revealed that low temperature (65 ^{o}C) and acid concertation (0.34 M) results in the synthesis of a superior EMD product in terms of surface area [51]. However, no cycling testing were conducted by that study.

Although no direct study has been conducted on the effect of current density, combinational studies performed by Devenney *et al.* reveal that lower current density (62.5 vs. 100 A m^{-2}) and medium acidic conditions (0.17 M vs. 0.05 or 0.28 M) produce the best EMD product in terms of

capacity utilization, but, no cycling results were presented [49]. Davis, whose experiments consisted of deposition of EMD in a pressurized cell reports that higher acid and salt concentrations (1.02 M H_2SO_4 and 0.75 M $MnSO_4$) lead to a higher percentage of structural water than when lower concentrations of about 0.9 M H_2SO_4 and 0.5 M $MnSO_4$ were used for the preparation of EMD. A quick highlight of some the findings presented can be found in the following table (Table 1.6).

Table 1.6 Comparison of EMD products synthesized under different conditions.

Factor Tested	Parameter Value	EMD Characterization	EMD Cycling	Source
Acid (Low)	pH = 2 *T = 80 °C* *CD = 80 to 100 A m^{-2}*	SA = 54.58 m^2 g^{-1}_{EMD} Pr ~ Low	Cumulative capacity of 4,500 mAh g^{-1}_{EMD} over 60 cycles	[40], [45]
Acid (High)	pH = 5 *T = 80 °C* *CD = 80 to 100 A m^{-2}*	SA = 51.5 m^2 g^{-1}_{EMD} Pr ~ High	Failed after 20 cycles (Cumulative capacity of 1,400 mAh g^{-1}_{EMD} over lifetime)	[40], [45]
Temperature (High)	T = 120 °C *pH = 0.3* *CD = 80 to 100 A m^{-2}*	High crystallinity	1st Capacity: 240 mAh g^{-1}_{EMD} 15th Capacity: 45 mAh g^{-1}_{EMD}	[50]
Temperature (Low)	T = 60 °C *pH = 0.3* *CD = 80 to 100 A m^{-2}*	Low crystallinity	No cycling (single discharge) 1st Capacity: ~ 30 - 100 mAh g^{-1}_{EMD}	[50]
Current Density (High)	CD = 100 A m^{-2} *pH = 0.7* *T = 90 to 99 °C*	Not directly available	Low capacity utilization	[49]
Current Density (Low)	CD = 62.5 A m^{-2} *pH = 0.7* *T = 90 to 99 °C*	Not directly available	High capacity utilization	[49]

An alternative attempt to enhance EMD's performance has been to incorporate metal ions in the EMD's structure during synthesis by introducing additives to the electrolysis electrolyte solution

[28], [78]–[82]. Incorporation of titanium into EMD has been done by Nartey *et al.* who found that under the right conditions (high acid concentration), highly crystalline, high surface area, and highly rechargeable titanium incorporated EMD can be produced [28]. Jantscher *et al.* have also taken this method approach by producing barium and barium + titanium incorporated EMD [82]. Their results reveal that while barium has no direct effect on EMD's physical and electrochemical characteristics, barium mixed with titanium increases the surface area of EMD by 4-fold. Although their high surface area EMD had a high internal resistance, the capacity retention of this altered EMD was higher. Bodoardo *et al.* have investigated the incorporation of aluminium ions [78]. Their results show that aluminium incorporation increases the amorphicity of EMD, and the rechargeability. However, only 2 cycles were demonstrated. It is also important to mention that the control experiment in this paper, pure EMD, is made in a highly acidic environment (4 M HNO_3) and its performance has been argued by the authors to be similar to that of metal-ion incorporated sample. Castledine *et al.* have investigated the influence of bismuth ions, and they claim an almost 100% charge retention of the product can be achieved as tested through 640 cycles of cyclic voltammetry [81]. Although they can't present a reason for the high rechargeability of this EMD, they hypothesize that bismuth incorporation might inhibit formation of irreversible manganese oxide phases. A quick highlight of some the work presented can be found in the following table (Table 1.7).

Table 1.7 Comparison of metal-ion incorporated EMD products.

Dopant	EMD Characterization	EMD Cycling	Source
Titanium (~4%)	SA = 56.8 m^2 g^{-1}_{EMD} Higher crystallinity	60% capacity loss over 40 cycles (Non-specific capacity values provided: 1050 mAh to 400 mAh)	[28]
Barium (~2-3%) + Titanium (~0.6%)	SA = 81.3 m^2 g^{-1}_{EMD}	30% capacity loss over 20 cycles (Relative loss capacity provided)	[82]
Aluminum (~5%)	Lower crystallinity	30% charge loss over cycles 2 cycles	[78]

Modification of EMD through ionic or non-ionic surfactants additives during the synthesis of the material have also been attempted [27], [83]–[87]. Biswal, Ghavami, and Ghaemi have several reports on the role of surfactants during the EMD synthesis [27], [83]–[85], [87]. A common finding throughout their various reports is that surfactants (excluding quartenary amines) greatly affect the morphology (i.e., nanorod or microsphere-like products can be achieved), greatly increase the surface area (more than 100 m^2 g^{-1}_{EMD}), and as a result improve rechargeability. Non-ionic surfactants, i.e., t-octyl phenoxy polyethoxyethanol (Triton X-100) have shown to also increase the structural water content and also reduce the charge transfer resistance (R_{ct}) of the material when tested inside an alkaline cell (0.48 vs. 0.75 Ω) [27]. Potassium intercalation into EMD that might occur during the discharge reaction of EMD inside a potassium hydroxide electrolyte was also found to be reduced [87]. Table 1.8 presents some of the highlights of the researches mentioned.

Table 1.8 Comparison of EMD products synthesized with surfactants.

Electrolysis Additive	EMD Characterization	EMD Cycling	Source
Sodium tetradecyl sulfate (25 mg L^{-1})	SA = 125 m^2 g^{-1}_{EMD} Changed morphology (nanorods) Lower proton content	1st Capacity: 262 mAh g^{-1}_{EMD} 25th Capacity: 95 mAh g^{-1}_{EMD}	[85]
Tetraethylammonium bromide (50 mg L^{-1})	SA = 87.2 m^2 g^{-1}_{EMD} No effect on proton content Smaller grain size	1st Capacity: 298 mAh g^{-1}_{EMD} 14th Capacity: 60 mAh g^{-1}_{EMD}	[83]
Tween-20 (7 g L^{-1})	SA = 153 m^2 g^{-1}_{EMD} Changed morphology (nanospheres)	1st Capacity: 245 mAh g^{-1}_{EMD} 15th Capacity: 80 mAh g^{-1}_{EMD}	[87]
Triton X-100 (9 g L^{-1})	SA = 174 m^2 g^{-1}_{EMD} Changed morphology (nanofibers)	1st Capacity: 270 mAh g^{-1}_{EMD} 15th Capacity: 75 mAh g^{-1}_{EMD} Higher proton conductivity	[27], [87]

1.3.3 Chemically Synthesized MnO_2 and its Use in Alkaline Batteries

As previously mentioned, the variety of MnO_2 crystal structures [67] allows it to be used in several applications in the field of electrochemistry. While EMD (γ-MnO_2) remains the most researched MnO_2 product for alkaline batteries, very little information is available, to the best of author's knowledge, regarding the rechargability of phases that make up the EMD phase (β- and R- MnO_2) or any other chemically synthesized phases. Some results have been reported on the electrochemical behaviour of α-MnO_2 and β-MnO_2 [88], [89], however only the initial discharge capacity is often reported at low depths of discharge. Therefore, the stability of single phase MnO_2 cathode in RAM is generally unknown.

However, a newly discovered topic in aqueous batteries does utilize chemically synthesized MnO_2 (α-MnO_2 or γ-MnO_2 phases) for highly rechargeable batteries [90]–[98]. These new aqueous

MnO_2/Zn batteries use a $ZnSO_4$ electrolyte solution as opposed to a hydroxide salt electrolyte solution, i.e. KOH, which is mainly used in conventional MnO_2/Zn batteries. Initially, $ZnSO_4$-based cells were thought to be Zn-ion batteries (with discharge and charge depending on the insertion and deinsertion of zinc ions present in the electrolyte) [90], [91], [94]–[98]. However, recent work by Pan *et al.* claims that a proton exchange inside the MnO_2 is still operative when a $ZnSO_4$ electrolyte is used [42]. Furthermore, any capacity fade from these "alkaline" cells is believed to fixed by addition of a minute amount of a manganese salt. Added $MnSO_4$ reportedly reduces the extent of manganese dissolution, which is claimed to be the main reason for capacity fade. By incorporating 0.1 M $MnSO_4$ to the $ZnSO_4$ electrolyte solution, 5,000 cycles with 92% capacity retention has been achieved by Pan *et al*. Table 1.9 presents some of the highlights of the researches done in this field.

Table 1.9 Comparison of the cycling performance of various $ZnSO_4$-based MnO_2/Zn cells.

Electrolyte/MnO_2 Phase	**No. of Cycles**	**Initial Capacity (mAh g^{-1}_{MnO2})**	**Final Capacity (mAh g^{-1}_{MnO2})**	**Source**
$ZnSO_4$ (1M) [using γ-MnO_2)]	45	250 (highest at cycle 5)	158	[98]
$ZnSO_4$ (2M)/$MnSO_4$ (0.1M) [using $\alpha-MnO_2$]	5000	160	160	[42]

1.4 Objectives of the Thesis

The main objective of this thesis is to improve the cycling performance of rechargeable MnO_2/Zn cells. A goal of achieving a minimum specific capacity of 100 mAh g^{-1}_{MnO2} was set. To achieve that, it was attempted produce high quality EMD products (high structural water content, high

ramsdellite content, and high surface area) and study its effect on its rechargeability in RAM cells. The steps below were followed for this study:

1. Synthesize MnO_2 materials electrochemically under various conditions.
    a. Vary the pH (proton transport) of the electrolysis cell to improve the structural water content of EMD.
    b. Study effect of current density (rate of formation) on EMD's electrochemical behavior when synthesized at the optimum acid concentration.
2. Perform characterizations on the synthesized EMD samples to identify the differences in their physical properties (phase, Pr, structural water content, and surface area) and electrochemical behaviour in KOH electrolyte (cycling, efficiency, and impedance).
3. Identify the mode of failure by performing characterizations on the cycled cathode.

To further improve rechargeable MnO_2/Zn cells, other phases of MnO_2 (ramsdellite, hollandite, and birnessite) were synthesized and their electrochemical behaviour in the KOH electrolyte was studied and compared to that of EMD.

An alternative electrolyte ($ZnSO_4$) was also investigated. The behaviour of various electrolytically synthesized MnO_2 samples in $ZnSO_4$ electrolyte was studied and further investigations were carried out on the $MnSO_4$ additive used with this electrolyte.

Chapter 2. Experimental Methods

2.1 Manganese Dioxide Synthesis

MnO_2 was synthesized electrochemically in both mild and highly acidic environments. MnO_2 was also synthesized chemically at both atmospheric and high pressure conditions. These methods are discussed in this section.

2.1.1 Electrochemical Method for Production of MnO_2 in Highly Acidic Environments

Electrodeposition of EMD samples, in highly acidic environments, was performed in a two-electrode electrolysis cell shown schematically in Figure 2.1.

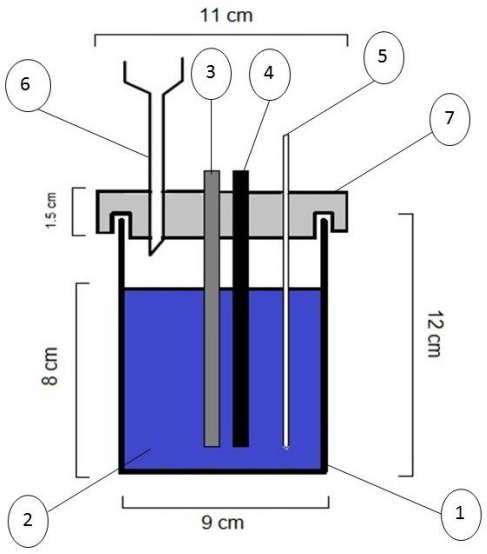

1	Electrolysis Reactor (**Volume:** 600 mL glass beaker)
2	Electrolyte Solution (**Volume:** 450 mL) (**Content:** 1 M $MnSO_4$ + 0.5-5 M H_2SO_4)
3	Titanium Anode (**Dimensions:** 4 cm x 14 cm x 0.2 cm)
4	Graphite Cathode (**Dimensions:** 4 cm x 14 cm x 0.6 cm)
5	Thermocouple (**Temperature:** 95 °C)
6	Reflux Condenser (**Joint Fitting:** ST/NS29/32)
7	Reactor Lid (**Material:** Poly(methyl methacrylate))

Figure 2.1 Schematic apparatus used for production of EMD.

The anode electrode, where the deposition of EMD occurs (see Equation 2.1), consisted of a polished 4 cm × 14 cm × 2 mm titanium plate (McMaster-Carr; 9039K21). The cathode electrode, where hydrogen gas evolves (see Equation 2.2), consisted of a 4 cm × 14 cm × 6 mm graphite plate (McMaster-Carr; 9015K83). These two materials (titanium and graphite) were chosen due to their high conductivity and stability, and lower cost compared to other viable metals such as lead, copper, stainless steel, etc. [99].

$$Mn^{2+} + H_2O \rightarrow MnO_2 + 4H^+ + 2e^- \qquad E_{anode} = 1.224\ V_{SHE} \qquad \textbf{Equation 2.1}$$

$$2H^+ + 2e^- \rightarrow H_2 \qquad E_{cathode} = 0.000\ V_{SHE} \qquad \textbf{Equation 2.2}$$

The electrolyte solution consisted of a fixed amount (1 M) of $MnSO_4$ (98%; Anachemia) and varying concentrations (0.5 – 5 M) of H_2SO_4 (95.0%; Fisherbrand). The experiments were performed at ambient pressure (1 atm) and at an electrolyte temperature of 95 $\pm$ 1 ^oC that was monitored using a type K PTFE coated thermocouple (Corning). Each electrodeposition experiment was performed at a constant current density (galvanostatic). Different current density values in the range of 0.0075 to 0.0175 A cm^{-2} were tested in this thesis. A Solartron Analytical 1470E potentiostat was used to perform these galvanostatic experiments. Each experiment was performed over a period of 15 hours to obtain approximately 5 g of product. The cell potential was generally maintained at 2.5 $\pm$ 0.3 V during the electrolysis. After each experiment, the EMD deposits were chipped and ground, using an agate mortar and pestle, and washed using a vacuum filter until the EMD/water suspension reached a pH of at least 6.5. Current efficiency, $CE_{electrolysis}$, of each deposition was determined by calculating the ratio of the

theoretical yield, using Faraday's law (see Equation 2.3), to the mass of the actual EMD obtained. Table 2.1 lists all the experiments conducted in this section.

$$M[g] = \frac{M\left[\frac{86.9g}{mol}\right] \times I\left[\frac{C}{s}\right] \times t[s]}{N[2e^-] \times F[96500C]} \qquad \textbf{Equation 2.3}$$

Table 2.1 List of EMD samples prepared in highly acidic environments.

$[H_2SO_4]$ (M)	Current Density (A cm^{-2})	$[MnSO_4]$ (M)	Temperature (^oC)
0.5	0.0125	1	95
1			
2			
2	0.0075		
2	0.0175		
2.25	0.0125		
2.5			
2.75			
3			
5			

2.1.2 Electrochemical Method for Production of MnO_2 in a Mild Environment

EMD prepared in a milder environment was also attempted in this thesis. The electrolyte bath used for this process consisted of a 2 M $ZnSO_4$ (98%; Anachemia) with 0.6 M $MnSO_4$ (99%; Anachemia) solution. The name NEMD has been assigned in this thesis for this new type of EMD. The same apparatus shown in Figure 2.1 was used for the synthesis of NEMD. However, the reflux unit and thermocouple were not used as the electrolysis of NEMD was carried out at room temperature. Furthermore, graphite and titanium were also not used for NEMD synthesis since they displayed no reactivity inside the electrolyte at the conditions tested. Instead, the anode

consisted of a 4 cm × 14 cm × 0.04 mm piece of nickel foil (MTI; MF-NiFoil-25u) and the cathode consisted of a 4 cm × 14 cm × 0.5 mm piece of zinc foil (Dexmet). The electrolysis was carried out at a constant current potential of 2.5 V for 24 hours to obtain 0.5 g of product.

2.1.3 Chemical Methods for Production of MnO_2

Chemically produced manganese dioxides (CMD) are generally easier to synthesize, and to control the crystallographic phases and other physiochemical properties. Chemical production methods are also better understood in the literature. Figure 2.2 displays the basic principles required to synthesize a variety of different MnO_2 phases chemically. By using precursors that includes the proper metal ion, a template can be created for synthesize of the desired phase [100].

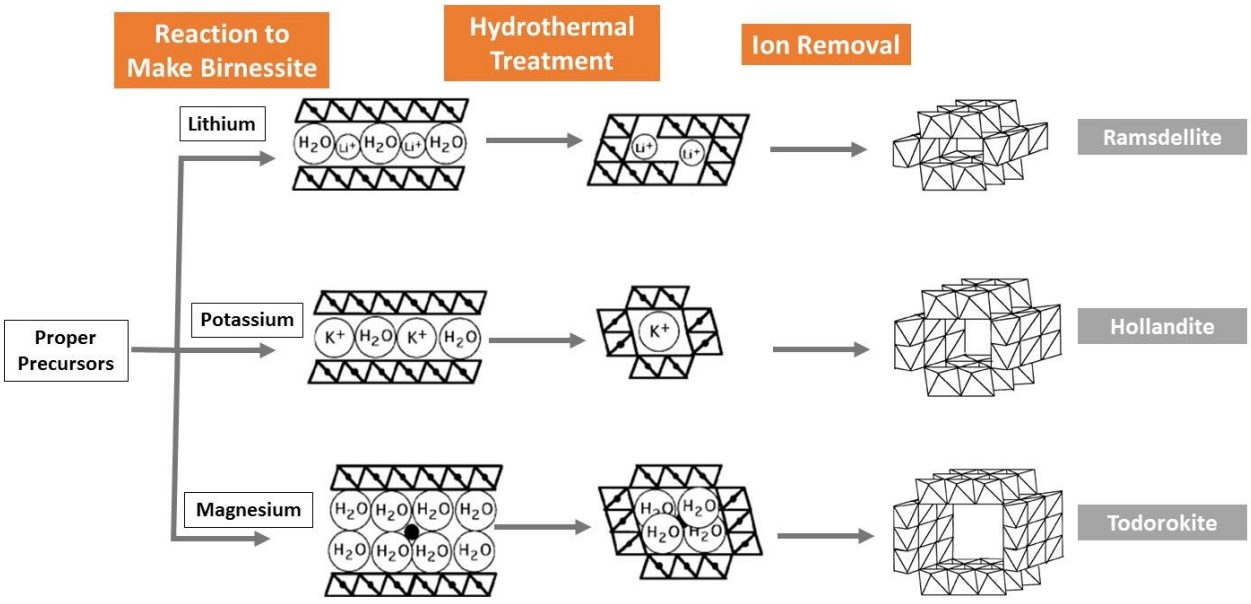

Figure 2.2 Basic principles for chemical synthesis of various MnO_2 phases. [100]

Three different CMDs were tested in this thesis: ramsdellite, hollandite, and birnessite. The birnessite phase, which is the first MnO_2 phase that forms before any other phases develop (see Figure 2.2), was synthesized with a simple oxidation-reduction (redox) reaction between 0.4 M $KMnO_4$ (99%; Anachemia) and 2 M HCl (37.0%; Fisherbrand) at ambient pressure and boiling temperature [101].

The ramsdellite and hollandite phases were synthesized hydrothermally at 120 ^oC. The ramsdellite phase was synthesized through the delithiation of a spinel lithium manganese product [102] that can be obtained commercially. 5 g of $LiMn_2O_4$ (99%; MTI) was mixed with 100 mL of 2.5 M H_2SO_4 (95.0%; Fisherbrand) and then transferred into a 200 mL polytetrafluoroethylene container that was placed inside a hydrothermal vessel (autoclave). The hollandite phase was synthesized through a one-step redox reaction between manganese sulfate and potassium permanganate with added sulfuric acid for the removal of potassium ions from the hollandite template [42]. 20 mL of 0.3 M $KMnO_4$ (99%; Anachemia), 90 mL of 0.01 M $MnSO_4$ (98%; Anachemia), and 1.5 mL of 2 M H_2SO_4 (95.0%; Fisherbrand) were mixed and then transferred to the aforementioned hydrothermal container and vessel.

All the CMD samples were centrifuged and washed three time after synthesis. The washed samples were then dried at 60 ^oC for 24 hours. Table 2.2 lists CMD products synthesized and tested in thesis.

Table 2.2 List of MnO_2 samples prepared chemically.

Sample Name	Method	Precursors	Condition
Birnessite	Ambient Pressure	$KMnO_4$ + HCl	100°C for 30 minutes
Ramsdellite	Hydrothermal	$LiMn_2O_4$ + H_2SO_4	120°C for 24 hours
Hollandite	Hydrothermal	$MnSO_4$ + $KMnO_4$ + H_2SO_4	120°C for 24 hours

2.2 Electrochemical Characterization Method

The electrochemical properties of the synthesized MnO_2 products were examined versus a zinc electrode with either the common alkaline (KOH) or zinc sulfate ($ZnSO_4$) electrolyte. The MnO_2 products were either tested as thick electrodes (~500 µm), which mimic scaled up commercialized batteries, or as thin-film electrodes (~30 µm), which is more suited for battery materials research.

2.2.1 Thick- and Thin- Film Electrode Preparation

Figure 2.3 and Table 2.3 summarize the procedures used for thick-film electrode preparation. For the cathode, a dry powder mixture was first prepared using an MnO_2 product and graphite (TIMREX; Timcal KS44). The graphite was added to enhance the electronic conductivity of the cathode electrode [26]. The cathode powder was mixed with a 1.7 wt% carboxymethyl cellulose (MTI; EQ-Lib-CMC) gelling solution and a 50 wt% styrene butadiene copolymer binding solution (MTI; EQ-Lib-SBR). The purpose of the gelling solution was to make a playdough-like paste that could easily be spread onto an expanded nickel mesh current collector (Dexmet; 3 Ni 5-077). The prepared cathodes (paste + current collector) were also rolled/pressed, and finally cut into approximately 3.5 cm × 2 cm pieces to achieve a thickness of 0.5 ± 0.1 mm.

For the anode, a dry powder mix composed of metallic zinc (Horsehead; 1239-024) and zinc oxide (ZOCHEM; ZOCO 101) was first prepared. Zinc oxide was added to the anode so that excess oxidized zinc is available to be reduced to metallic zinc during the charge reaction. This results in the prevention or inhibition of hydrogen evolution reaction that could occur if all the oxidized zinc is used up before the cathode is fully charged. The anode powder was also mixed with 1 M indium (III) sulfate (99.9%; Indium Corp.) that further inhibits the evolution of any potential hydrogen gas [26]. Furthermore, zinc powder has the ability to form long chains of dendrites during cell cycling. Dendrites can short the cell by piercing through the separator [26]. Therefore, polyethylene glycol (Sigma-Aldrich; Triton X-100) was also added to anode mix to coat the zinc with a layer of surfactant thus inhibiting zinc agglomeration [26]. The anode mixture was then mixed with a 2.1 wt% acrylic acid polymer (Lubrizol; Carbopol® 940) gelling solution and a 60 wt% polytetrafluoroethylene (Sigma-Aldrich; 9002-84-0) binding solution. The resulting paste was spread onto a tin-plated expanded brass mesh current collector (Dexmet; 3 Brass 10-125) and finally cut into approximately 3.5 cm × 2 cm pieces. The anode electrodes (pastes and current collector) had an average thickness of 1.0 ± 0.3 mm.

Table 2.3 Ingredient list for one batch of thick-film cathode and anode to produce six electrodes.

Cathode Electrode		**Anode Electrode:**	
Material:	**Amount (g):**	**Material:**	**Amount (g):**
MnO_2	4.8	*Metallic Zn*	11
Graphite	1.2	*ZnO*	2.75
1.7 wt% CMC	2	*2.1 wt% Carbopol® 940*	2
50 wt% SBR	0.3	*60 wt% PTFE*	0.1
		1 M $In_2(SO_4)_3$	0.22
		Triton X-100	0.2

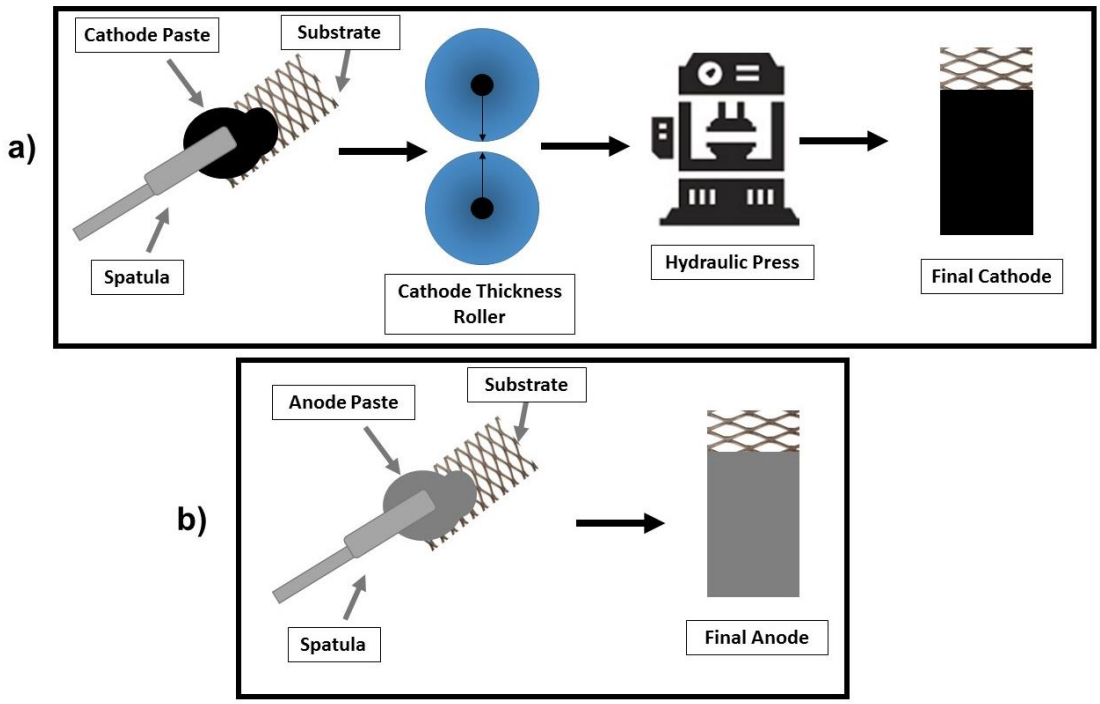

Figure 2.3 (a) The MnO_2 paste is first spread onto an expanded mesh and then processed through an adjustable thickness roller (0.5 mm) and hydraulic press (8 MPa) to produce the cathode electrode. (b)The zinc paste is s spread onto an expanded mesh to produce the anode electrode.

Figure 2.4 and Table 2.4 summarize the general procedure used for thin-film electrode preparation. For the cathode, an MnO_2 product was mixed with carbon black (VULCAN® XC72R) and added to a 7 wt% polyvinylidene fluoride (MTI; EQ-Lib-PVDF) binding solution. The mixture was then added to an n-methyl-2-pyrrolidone (MTI; EQ-Lib-NMP) solvent to obtain an adequate ink consistency which allowed it to be spread onto the current collector (0.037 mm thick carbon paper – TGP-H-12). The ink was either deposited on pre-cut pieces of current collectors using a transfer pipette or spread onto a larger piece using a doctor blade adjusted to a thickness of 0.032 mm. An approximate rate of 1 cm s^{-1} (low shear rate) was used for the spreading of the cathode ink to produce high quality electrodes. The ink and substrate were then dried on a hot plate at 150 ^{o}C for 2 hours and cut into 15 mm disks. 15 mm disks of 0.5 mm thick of zinc foil (Dexmet) was used at the thin-film anode electrode.

Table 2.4 Ingredient list for one batch of thin-film cathode (9 electrodes) and anode (9 electrodes).

Cathode Electrode:	
Material:	**Amount (g):**
MnO_2	0.35
Carbon Black	0.1
7 wt% PVDF	0.7
NMP	0.3
Anode Electrode:	
Zn Foil	2

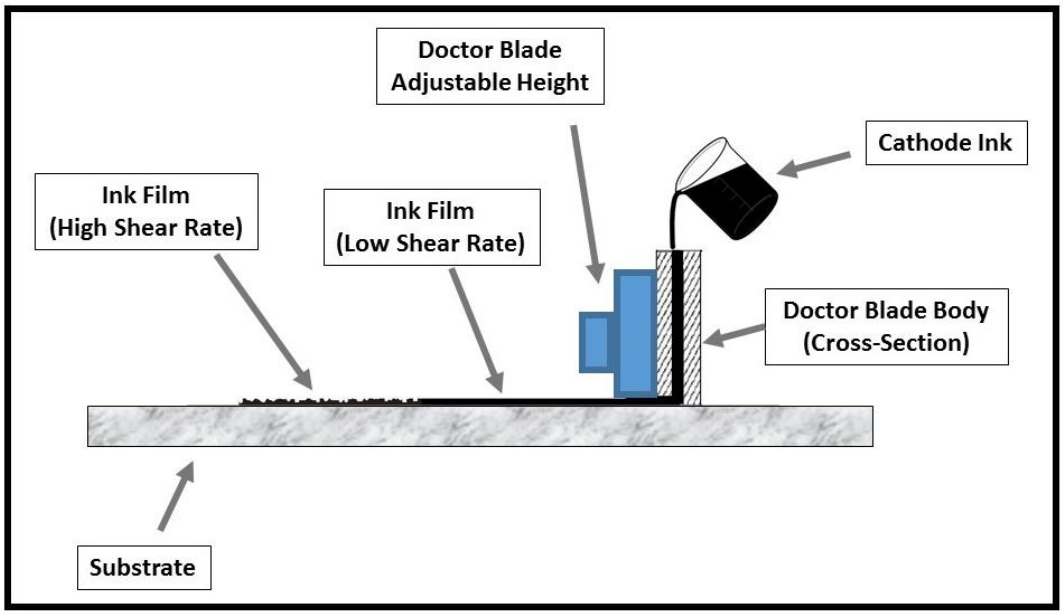

Figure 2.4 The cathode ink is first produced and spread onto a piece of carbon paper using a doctor blade. The final film can only be consistent if it is spread at a low shear rate (1 cm s^{-1}).

2.2.2 Full-Cell Setup and Measurement Techniques

The thick-film electrodes were tested inside a Delrin-based hardware developed in-house (see Figure 2.5 and Figure 2.6) [35]. The separators used consisted of bilayer cellophane film/nonwoven polyimide paper from Neptco (NWP150). For the electrolyte solutions, a 9 M potassium hydroxide (Fisherbrand; 85% Purity) solution was prepared. Approximately 0.6 mL of this solution was dispersed on top of each layer of the electrode stack. To ensure adequate contact during cycling, the electrodes were maintained under a 47 psi pressure (through a tin-plated brass plate under two 30 kg cm^{-1} springs) in the hardware.

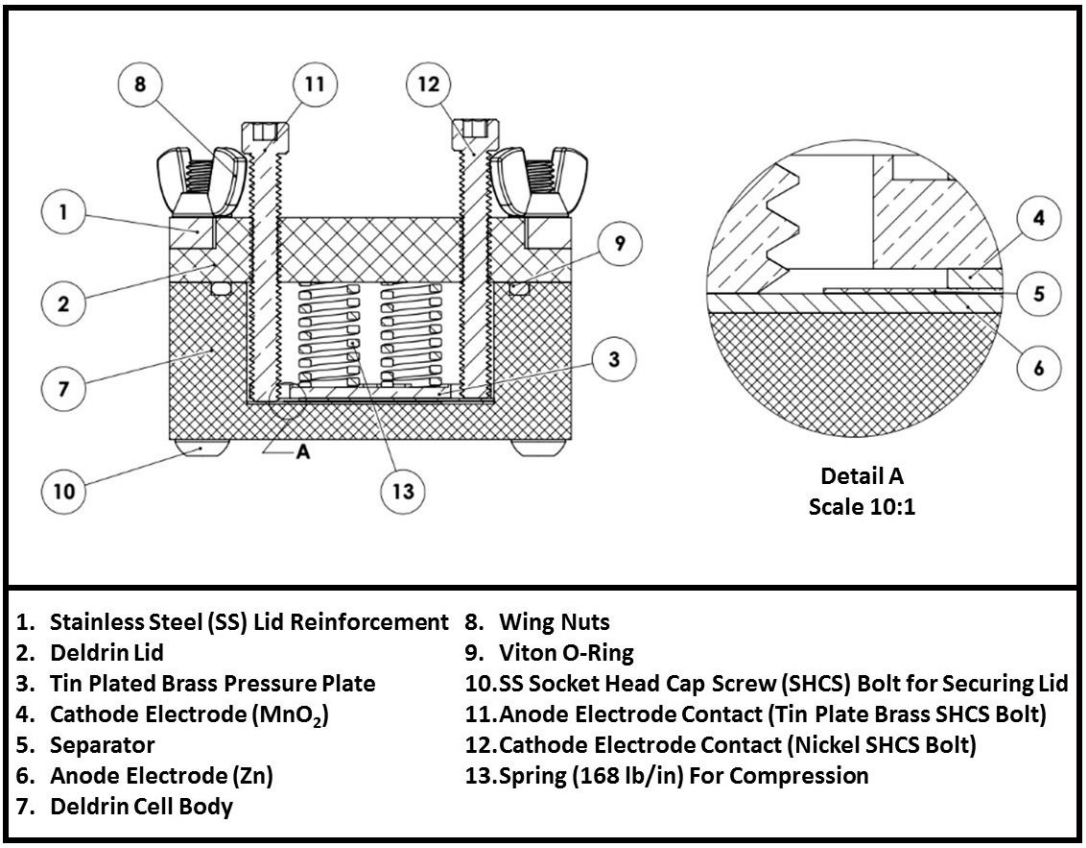

Figure 2.5 Detailed schematic of cell hardware (developed in-house) used for thick-film electrodes.

Thin-film electrodes were tested inside coin cells. A 20 mm wide stainless steel coin cell (CR2032, MTI) with a polypropylene O-ring (Figure 2.7) was used as the hardware. For the electrolyte, a 2 M $ZnSO_4$ (99%; Anachemia) solution was prepared. The 2 M $ZnSO_4$ electrolyte was used with and without a 0.1 M $MnSO_4$ (98%; Anachemia) additive. Approximately 0.2 mL of electrolyte was dispersed throughout the cell. The electrode/separator stack was placed on the bottom of the coin cell hardware, and a 15.5 mm stainless steel disk (spacer) and stainless steel Belleville washer (used as the spring/compressor) was placed on top before the coin cell was closed. A coin cell crimping tool was used to seal the cell.

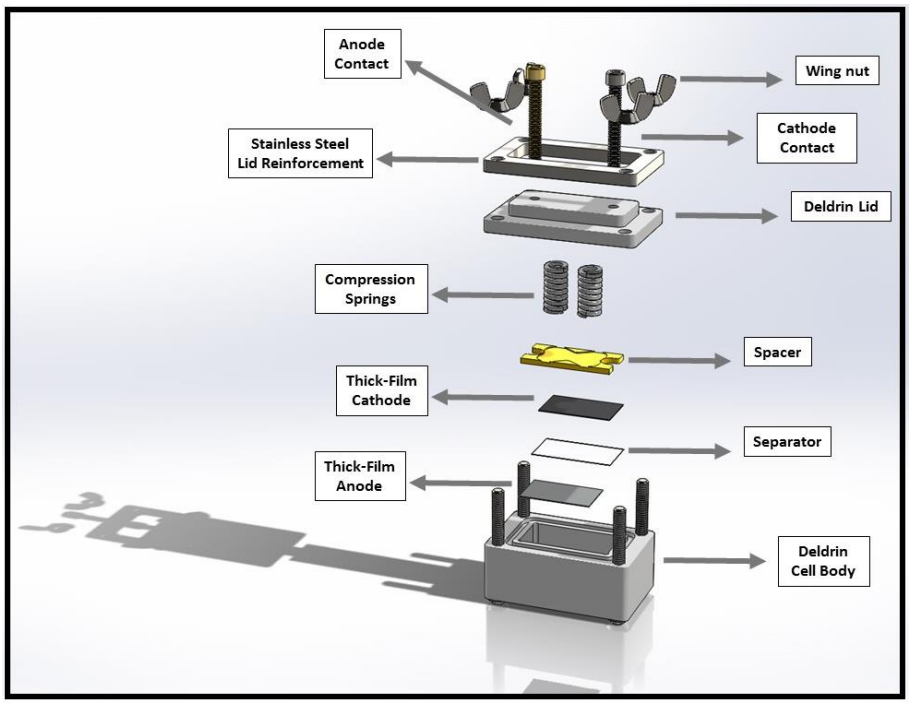

Figure 2.6 3D rendition of cell hardware (developed in-house) used for thick-film electrodes.

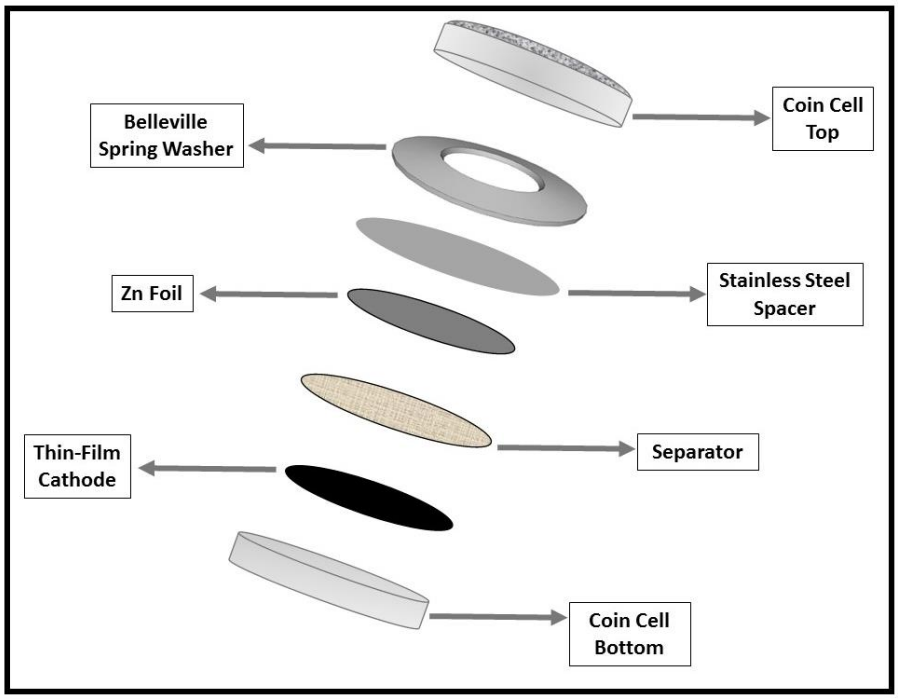

Figure 2.7 3D rendition of hardware used for thin-film cells.

For discharge/charge cycles, battery cyclers MTI BST8-3 (0.1 mA resolution) and Maccor 4300 (1 μA resolution) were used. The cells were cycled at a rate of either C/10 (low current) or C/2 (high current). Charge/discharge was done by applying a direct, constant current of positive and negative values, respectively. At the end of every galvanostatic charge step, cells were held at the charged potential to allow the flow of current inside the cell to dissipate so that the cell would be at equilibrium before the next cycle (see Figure 2.8). During this step (known as the potentiostatic step), the cells were charged further due to residual charge flow. The exact cycling was 1) galvanostatic discharge to 1.1 V (or 0.9 V) vs. Zn/ZnO, 2) galvanostatic charge to 1.75 V (or 1.85 V) vs. Zn/ZnO, and 3) a potentiostatic charge at 1.75 V (or 1.85 V) vs. Zn/ZnO for 3-6 hours. For most MnO_2 samples, about 3-4 cells were made and the results were averaged to obtain statistical significance.

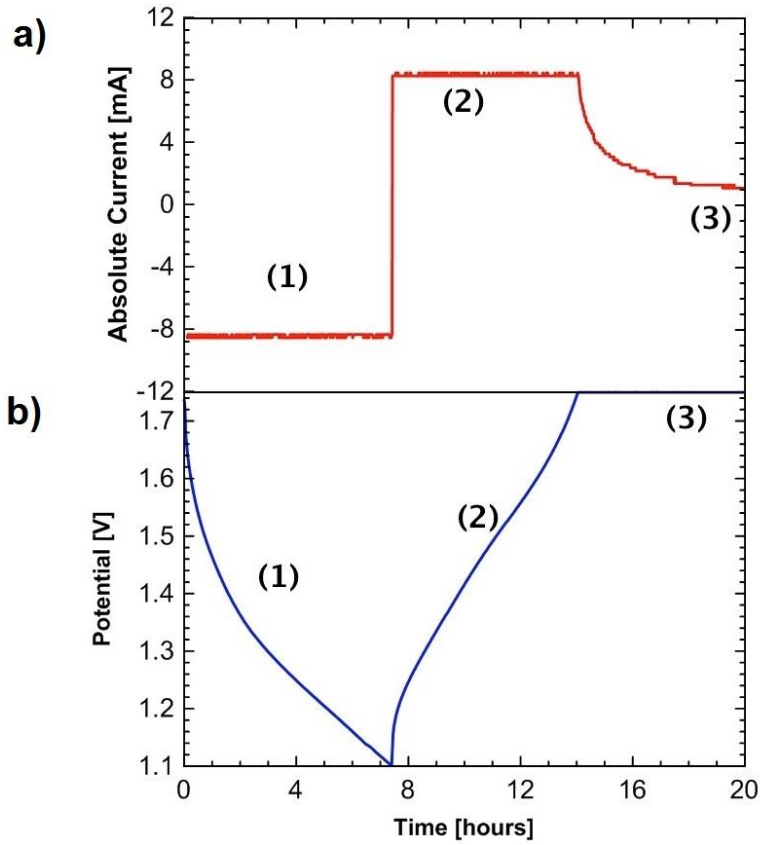

Figure 2.8 (a) Current/time, and (b) voltage/time figures displaying one cycle of the cycling regime used: (1) galvanostatic discharge, (2) galvanostatic charge, and (3) potentiostatic charge.

2.2.3 Half-Cell Setup and Electrochemical Impedance Spectroscopy (EIS) Measurements

Electrochemical Impedance Spectroscopy (EIS) measurements were carried out in a three-electrode cell (see Figure 2.9). Three-electrode systems are often designed to study the reaction of a single active electrode without the influence of any other unknown reactions [103]. In a 3-electrode system, current flows between the electrode of interest (working electrode or WE) and a non-corrosive, conductive material (counter electrode or CE) so that the working electrode is either oxidized or reduced by controlling the potential of the WE with respect to a reference electrode (REF). No reaction occurs on the reference electrode. The reference electrode is a

highly reversible electrode that is able to maintain its potential constant during cycling of the WE. The reference electrode is placed in close proximity to the working electrode so that the potential difference between two can be measured with high accuracy without significant resistance drop. For this research, an expanded nickel mesh (Dexmet, 3 Ni 5-077, thickness = 0.076 mm) was used as the counter electrode and a Hg/HgO electrode with 4.2 M KOH filling solution (Koslow, 5088) was used as the reference electrode. Nickel and Hg/HgO electrodes were used due to their high stability in basic environments [104], [105]. The cycling protocol for the 3-electrode system consisted of: 1) galvanostatic discharge to -0.30 V vs. Hg/HgO, 2) galvanostatic charge to 0.35 V vs. Hg/HgO, and 3) potentiostatic charge at 0.35 V vs. Hg/HgO for 3-6 hours.

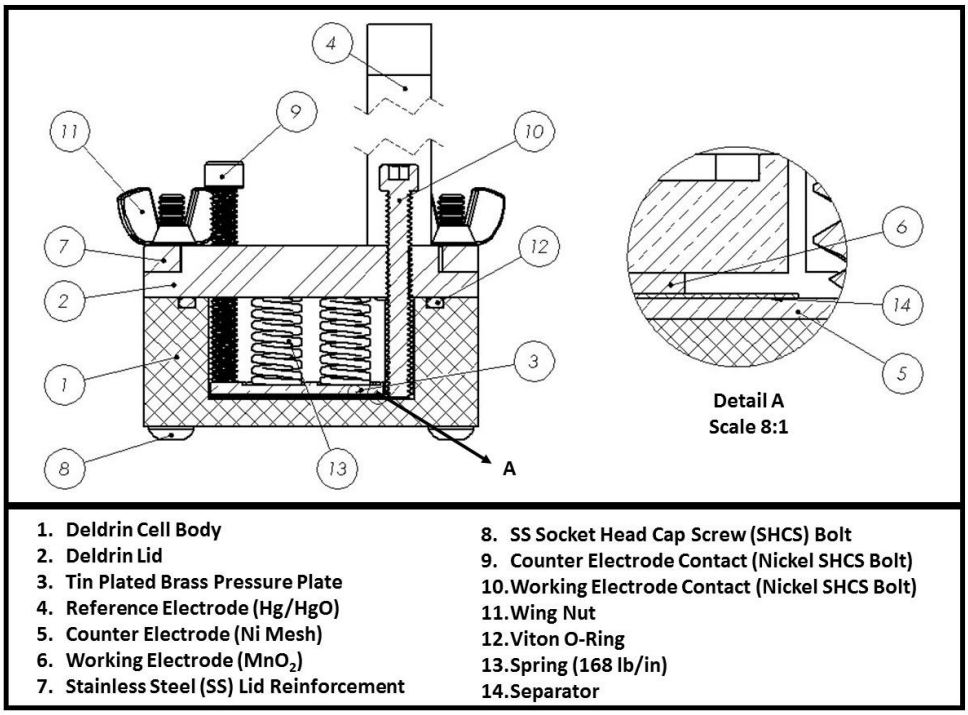

Figure 2.9 Detailed schematic of cell hardware (developed in-house) used for three-electrode cell experiments.

The three-electrode setup was used to observe the reversibility of the MnO_2 cathode without the influence of the zinc anode, and vice versa. Furthermore, the it was used to measure the impedance of the working electrode. The two main resistive components closely observed in this research were the resistance of the electrolyte known as series resistance (R_s) and the resistance occurring at the interface of the electrolyte and the electrode material, known as charge-transfer resistance (R_{ct}) [106]. Various impedance responses have been studied and equivalent circuits to represent each behavior have been modeled. Figure 2.9 displays the impedance response of a model important for this research, a simplified Randles cell, with each of the aforementioned resistance components identified [107].

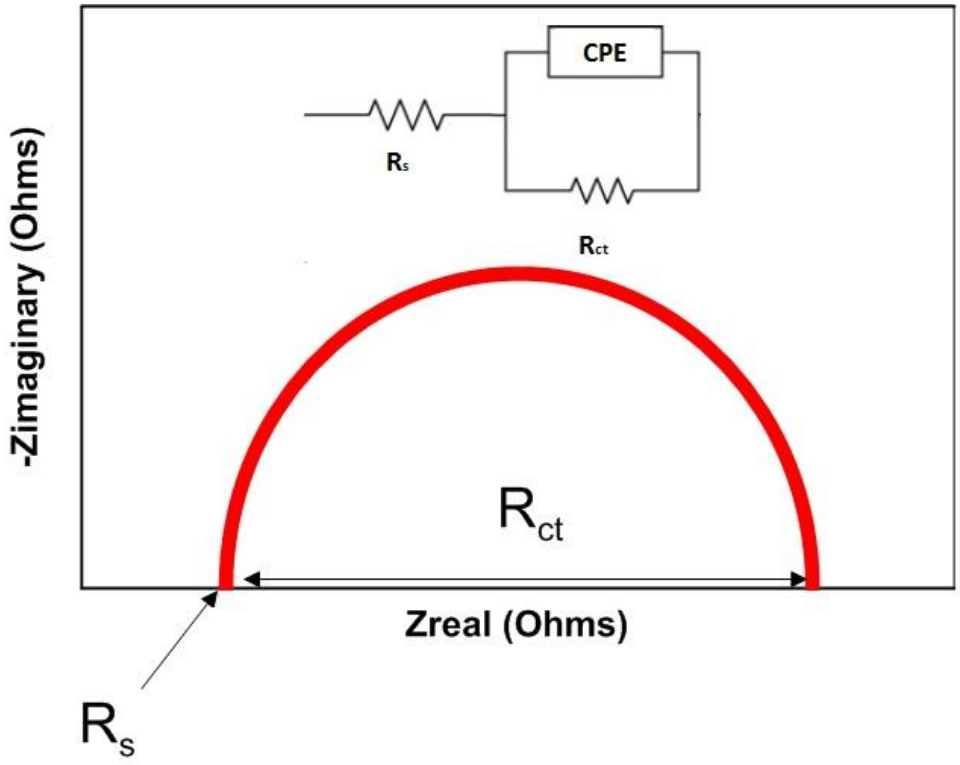

Figure 2.10 Impedance of a simplified Randles cell.

The impedance measurements for this thesis were performed using a Biologic (VMP3) potentiostat by applying a varying potential in the frequency (f) range of 0.1 Hz $\leq$ f $\leq$ 200 kHz, with a perturbation amplitude of 10 mV. The EIS spectra were obtained after the discharge, and after each of the charge steps.

2.3 Physical Characterization

2.3.1 X-Ray Diffraction (XRD) Studies

In order to identify the phase of crystallinity of the fresh and cycled cathode electrodes, x-ray diffraction (XRD) analysis was performed. Analysis was performed on well mixed powdered samples to ensure the random orientation of the various crystal structures in the sample. XRD techniques use monochromatic source x-rays (e.g., Kα = 1.54 Å) and scan the beams diffracted from the sample specimen. Crystal structures with repeating planes diffract (see Figure 2.11) the x-rays in a constructive manner according to Bragg's law (see Equation 2.4) where *d* is the distance between the planes, *n* is the order of diffraction (plane number), and θ is the angle of the incoming x-rays [108].

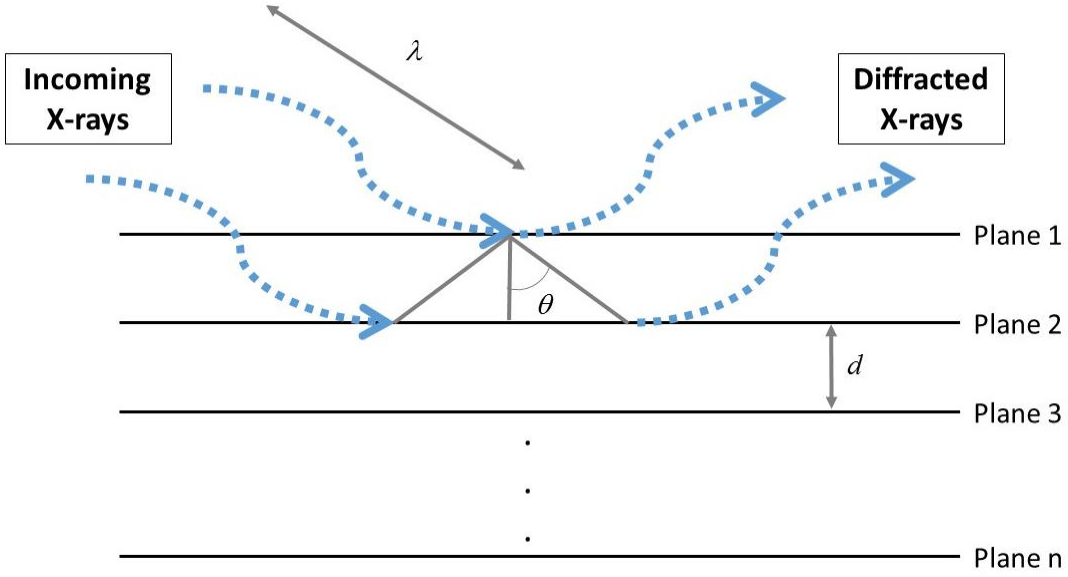

Figure 2.11 Conditions of Bragg's law.

$$n * \lambda = 2 * d * sin(\theta)$$ **Equation 2.4**

The XRD device has an x-ray detector to measure the intensity of these scattered constructive waves that are plotted as a function of scattering angle (2θ) (see Figure 2.11). The spectrums collected are then compared to a database system to find the crystal structures inside the sample. To prepare the samples for XRD analysis, synthesized MnO_2 material was ground to a fine powder. The cycled cathode materials were removed from the current collectors, washed, and also ground. XRD scans were collected from a Bruker D2 Phaser with a Cu Kα radiation source and Lynxeye detector. The scans were performed for a scattering angle range of $5° \leq 2\theta \leq 80°$. Analysis and pattern identification was performed using a 2013 ICDD PDF-2 database.

2.3.2 Surface Area and Pore Size Analysis

The specific surface area and pore volume distribution sizes were determined by N_2 physisorption experiments by the Brunauer–Emmett–Teller (BET) and Barrett-Joyner-Halenda (BJH) analysis methods. Figure 2.12 displays the working principles of N_2 physisorption analysis. Nitrogen gas is applied to the sample and is adsorbed onto the surface during which time the equilibrium gas pressure is measured [109]. The BET surface area is measured at moderately low pressures where the conditions only allow a monolayer of gas on the surface of the sample [109]. Thereafter, the gas pressure is increased further so that the gas can condense into the pores to measure size of the various pores inside the sample [109].

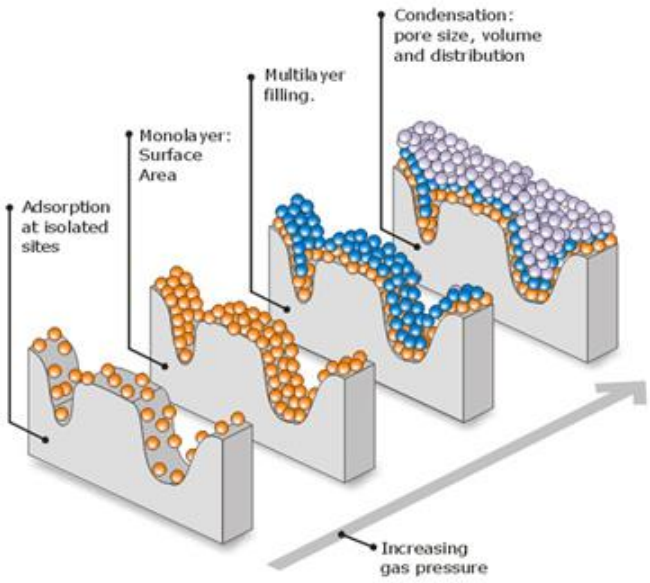

Figure 2.12 Working principles of N_2 physisorption for surface area and pore size analysis. [109]

The measurements for this section were carried out using Micromeritics ASAP 2020 Plus equipment. The samples (~200 mg) were initially degassed at 120 °C for 4 hours, under vacuum, using an onboard degassing port, prior to the adsorption experiments. Analysis was then carried out inside a bath of liquid nitrogen (77 K) to create the optimal temperature environment for nitrogen adsorption.

2.3.3 Thermogravimetric Analysis (TGA)

Thermogravimetric (TGA) measurements were performed to determine the exact weight loss of minute amounts of the samples (up to 200 mg) with very high accuracy ($\pm$ 0.01%) over different temperatures ranges. The mass loss measurements were carried out to calculate the structural water concentration of the EMD samples.

The measurements for this section were carried out using a TA Instruments Q500 equipment. The measurements were carried out in a flowing nitrogen environment. All samples were initially preheated at a temperature of 50 ^{o}C for one hour to remove any adsorbed moisture. The Q500 unit was programmed to heat the sample to 800 ^{o}C at a rate of 2 ^{o}C min^{-1}. Weight loss measurements were recorded with a precision of $\pm$ 0.01%. TGA experiments were performed 2 times and results were averaged.

2.3.4 X-Ray Fluorescence (XRF) Spectroscopy

X-ray Fluorescence (XRF) was used in this research for elemental analysis. The working principles of XRF are as follows: high energy x-rays are emitted from an excited source, i.e., tungsten, towards the product [110]. If the energy of the incoming x-rays is higher than the energy level of the electron residing in the lower energy shell level (K and L) of the material of interest, the

incident x-ray (primary radiation) is able to ionize those electrons allowing the excited atom to relax and emit x-rays which are referred to as fluorescence radiation (see Figure 2.13) [110]. The x-rays can be used to identify the elements in a given sample.

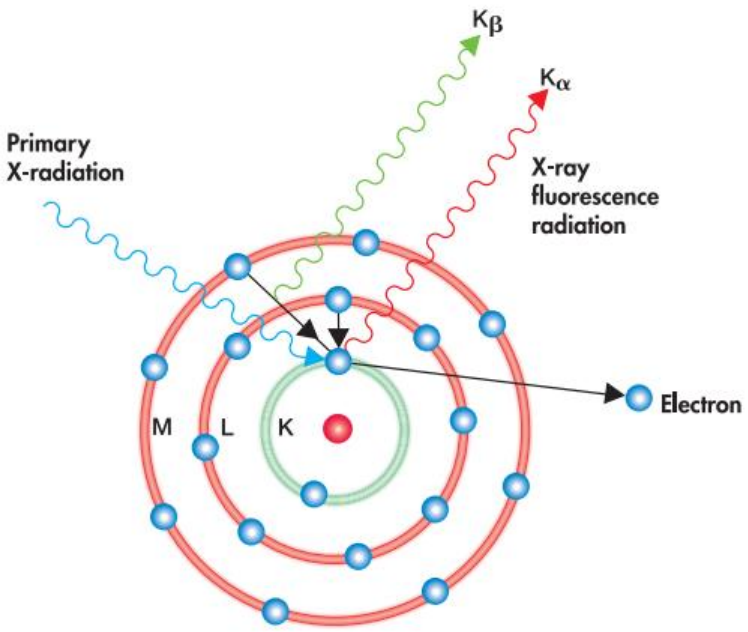

Figure 2.13 Working principles of XRF. [110]

The measurements for this section were carried out using a Fischerscope X-RAY XDV®-SDD XRF with a tungsten x-ray source (50 kV), a silicon detector, and a 3 mm area detection diameter of the material.

Chapter 3. Acidic Synthesis of EMD: Results and Discussion

3.1 The Difference in the Rechargeability of MnO_2 Cathode and Zinc Anode

In order to diagnose the failure modes of rechargeable alkaline batteries, it is important to investigate how the cathode and anode operate during cycling. To do this, an MnO_2/Zn cell was constructed using thick-film EMD (Erachem EAB-111) cathode, thick-film zinc anode, and 9 M KOH electrolyte. A Hg/HgO reference electrode was used to monitor the voltage of both electrodes during cycling. Figure 3.1 displays the cycling of the cell at a rate of C/10 for 10 cycles. While reducing the EMD from an initial potential of 0.35 $V_{Hg/HgO}$ to -0.30 $V_{Hg/HgO}$ (a potential change of 0.65 V), the zinc anode's potential fluctuates from an initial voltage of approximately -1.36 $V_{Hg/HgO}$ to -1.25 $V_{Hg/HgO}$ (a potential change of 0.11 V).

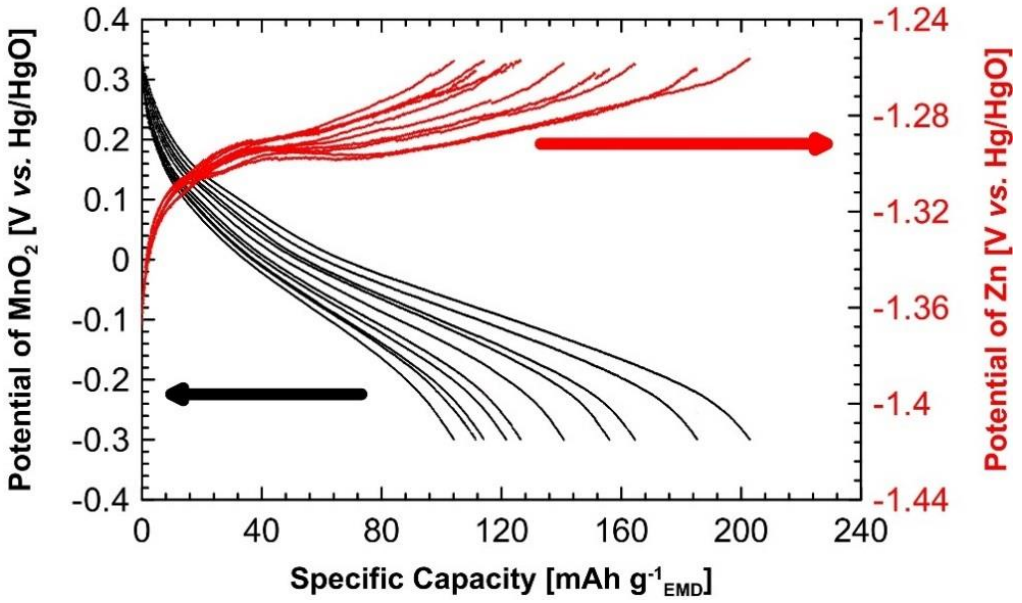

Figure 3.1 First 10 cycles of a three-electrode cell with EMD as the working electrode and zinc as the counter electrode.

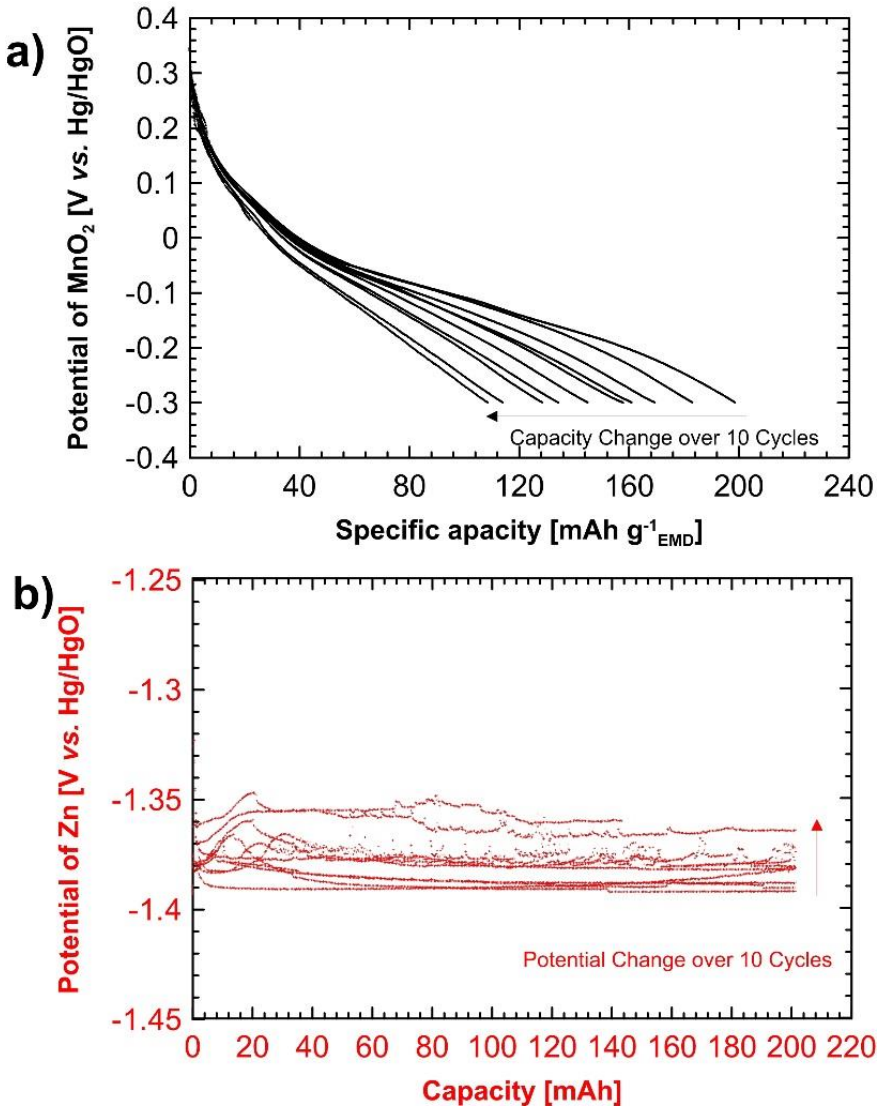

Figure 3.2 First 10 cycles of half-cells with (a) EMD as the working electrode and nickel as the counter electrode, and (b) zinc as the working electrode and nickel as the counter electrode.

Figure 3.1 reveals that the zinc anode's potential change during the discharge is only about 17% of EMD's potential change. However, it is also important to note that the zinc is being oxidized at a lower potential after each subsequent cycle, thus indicating that perhaps the anode is also losing capacity. In order to better differentiate the cycling behaviour between the two electrodes, half-cell experiments (three-electrode) were carried out for the cathode and the anode separately (in 9 M KOH electrolyte) in order to eliminate the influence of one electrode from the

other. A nickel mesh was used as the counter electrode in both cells. Figure 3.2 (a) and (b) display the cycling behaviour of EMD and zinc, respectively. It is important to note that the zinc electrode is able to maintain a more constant potential during its oxidation inside the half-cell, however, the capacity fade in EMD is still present inside the half-cell. While EMD's capacity decreases by approximately 50% during these 10 cycles, zinc shows almost zero capacity fade. Furthermore, the cells operate at an almost fixed potential of approximately -1.38 $V_{Hg/HgO}$ and the potential change during these 10 cycles is negligible (> 0.050 V).

3.2 Effect of Synthesis Parameters of EMD on its Rechargeability in Alkaline MnO_2/Zn Cells

The literature review in Chapter 1 revealed that the acid concentration used for the electrolysis of EMD has shown to vary the structural water content (which could affect the diffusion of protons in the lattice and therefore the overall performance) and proportion of the ramsdellite phase (the more active portion of EMD). More specifically, these two parameters were improved at higher acid concentrations. However, no comprehensive study of the impact of acidic concentration on the physicochemical and electrochemical properties of EMD has been reported to this date, particularly with respect to rechargeability of the EMD. Furthermore, long term cycling data (≥ 50 cycles) of rechargeable MnO_2/Zn with adequate demonstration of repeatability (i.e., statistical confidence) has not been reported either. Therefore, a systematic study of EMD samples prepared over a wide range of acid concentrations (0.5 - 5 M H_2SO_4; -0.7 < pH < 0.3) was performed, and the impact on the physical and electrochemical behavior of the EMD, including long-term cycling, was examined.

3.2.1 Acid Concentration

For this portion of the thesis, samples listed in Table 2.1 were synthesized and analyzed. All the electrochemical characterizations for these samples were performed using the Delrin-based cell hardware and thick-film electrodes. 9 M KOH as the electrolyte was used for the analysis of the MnO_2 products in MnO_2/Zn cells.

3.2.1.1 Physical Characterization of Freshly Synthesized EMD

Figure 3.3 (a) and (b) show the XRD diffractograms of the EMD samples synthesized at varying H_2SO_4 concentrations as well as the Erachem EAB-111 EMD sample used for comparison. Samples which were produced at an acid concentration (C_{H2SO4}) lower than or equal to 2 M have XRD patterns which closely resemble the γ-MnO_2 XRD pattern reported in the literature (type *III* EMD). These samples contain defects with extensive twinning in their structure [74].

Samples prepared in $C_{H2SO4} \geq 2.25$ M display a major shift in the scattering angle for many of the prominent EMD diffraction peaks and an almost complete disappearance of the (110) Bragg peak (characteristic of the EMD phase [74] – indicated by the red line). Furthermore, these samples show the gradual growth of additional MnO_2 phases with increasing acid concentration. Due to high amount of defects in the phases, proper identification of these phases is challenging. However, the prominent Bragg peaks at the lower scattering angles ($10^o \leq 2\theta \leq 20^o$) and the Bragg peaks at $2\theta \approx 28.5^o$ and 50^o do match the (110), (200), (310), and (411) peaks of α-MnO_2 or hollandite (PDF# 00-44-0141). The α-MnO_2 peaks are indicated by the blue lines in Figure 3.3.

Although the main use of the XRD analysis for EMD is to observe any structural change with varying synthesis parameter, it could further be used to find the percentage of the pyrolusite phase, i.e. Pr, in the EMD structure. A model proposed by Chabre *et al.* can be used to calculate Pr (see Equations 3.1-3.2). This model uses the 2θ Bragg peak position correlated to the EMD plane with (110) planar vector direction [74].

$$P_r = 0.602\,x - 0.198\,x^2 + 0.026\,x^3 \qquad \textbf{Equation 3.1}$$

$$x = 2\theta(110) - 21.248 \qquad \textbf{Equation 3.2}$$

Figure 3.3 (b) shows that the angle of the (110) Bragg peak clearly shifts when C_{H2SO4} varies between 0.5 M and 5 M. The peak position of the (110) reflection were determined by a Gaussian-profile shape to the peak, and Pr values were calculated for all the samples (see Figure 3.4). The commercial EMD was found to have a Pr of 0.41. Pr values for the synthesized samples appear to initially decrease with increasing C_{H2SO4}. Samples synthesized in 0.5 M ≤ C_{H2SO4} ≤ 2 M have corresponding Pr values of: 0.32, 0.17, 0.17, respectively, where the minimum value of Pr, Pr_{min}, is reached for the range of sulfuric acid concentrations studied. These results were of high interest because the ramsdellite portion of the EMD structure has been reported to be the more electrochemically active portion and provide the primary source of discharge/charge capacity [76], [77].

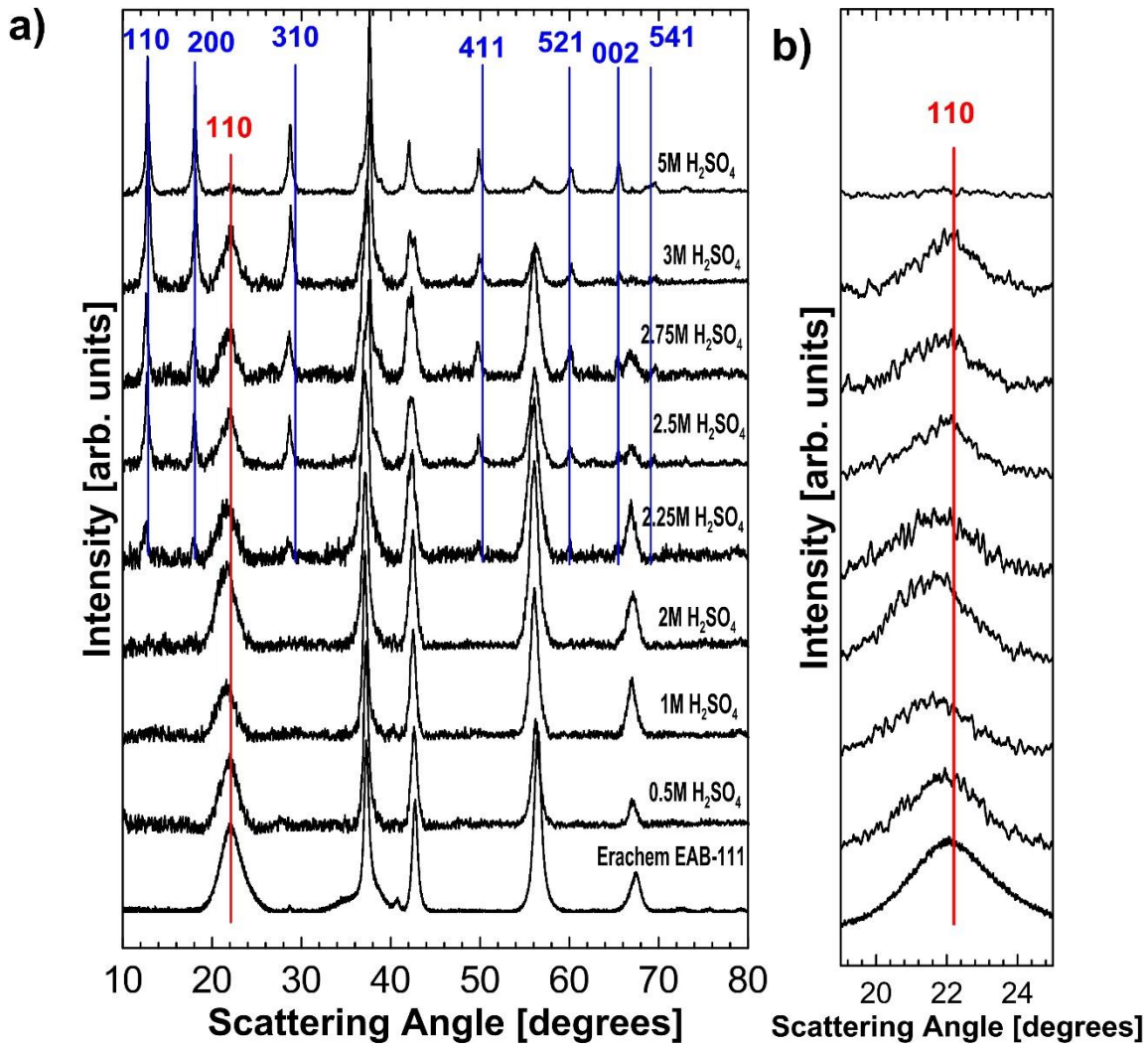

Figure 3.3 (a) XRD profiles of the EMD samples prepared at different acid concentrations and Erachem EAB-111; (b) the (110) Bragg diffraction peak for $20^o \leq 2\vartheta \leq 24^o$.

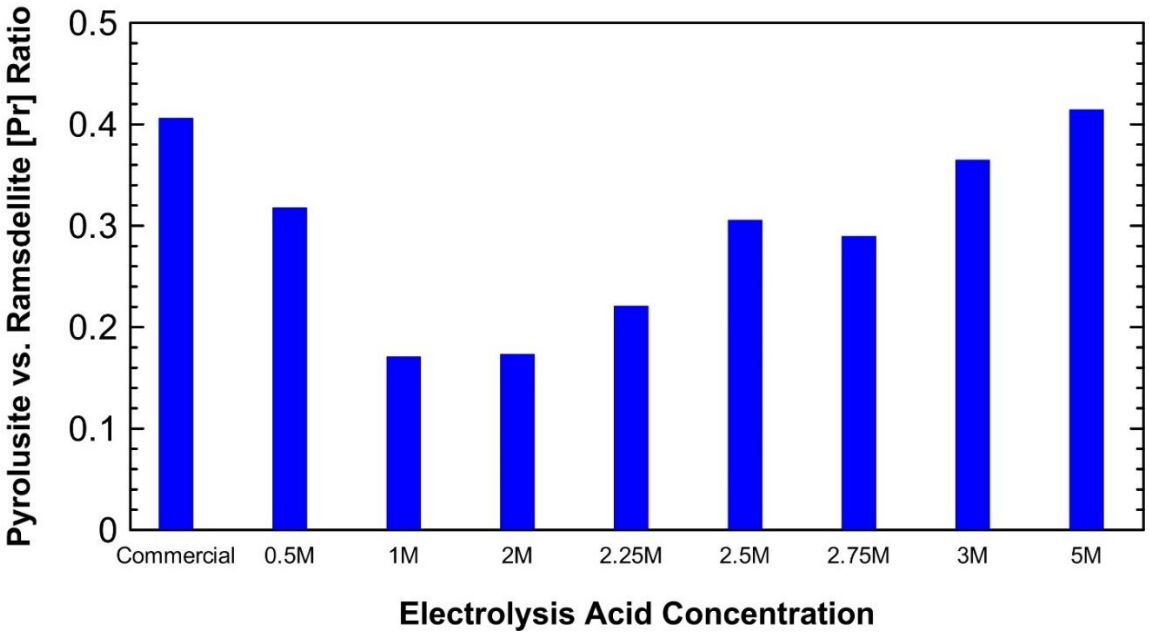

Figure 3.4 Pr ratio of EMD samples prepared vs. the electrolysis acid concentration in comparison to a commercial EMD.

In order to investigate the change in water content ($W_{structural}$) with changing C_{H2SO4}, TGA analysis of the samples was performed (see Figure 3.5). Weight losses from ≈ 120 °C - 300 °C represent the proton loss from the defect sites (the structural water content) [72]–[75]. Figure 3.6 shows water content as a function of C_{H2SO4}. The structural water content increases from $W_{structural} \approx$ 2.6% to $W_{structural} \approx 4.4\%\ wt_{H2O}$, when the C_{H2SO4} increases from 0.5 to 2 M. For 2 M $\leq C_{H2SO4} \leq$ 3 M, however, the structural water only fluctuates around $W_{structural} \approx 4.5 \pm 0.3\ \%wt_{H2O}$. Samples prepared with 2 M acid show a 1.7× increase in the water content compared to the commercial EMD ($W_{structural} \approx 2.6\ \%wt_{H2O}$). TGA results show that even the samples synthesized in the least acidic environment ($C_{H2SO4} \approx 0.5$ M) contains a higher percentage of water ($W_{structural} \approx 3.5\ \%wt_{H2O}$) compared to the commercial EMD. Although Erachem does not disclose the synthesis conditions of their product, commercially produced EMD typically use $C_{H2SO4} \approx$ 0.09 - 0.55 M H_2SO_4 in their electrolysis bath [48].

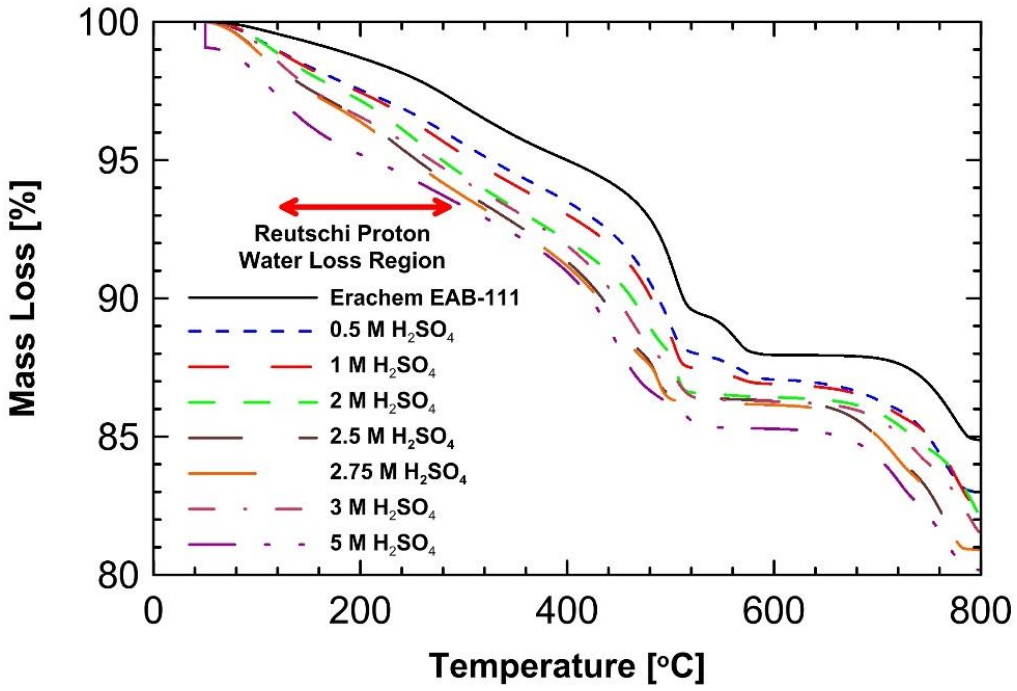

Figure 3.5 TGA of EMD samples prepared at different acid concentrations, and Erachem EAB-111 over the temperature range 50 °C – 800 °C.

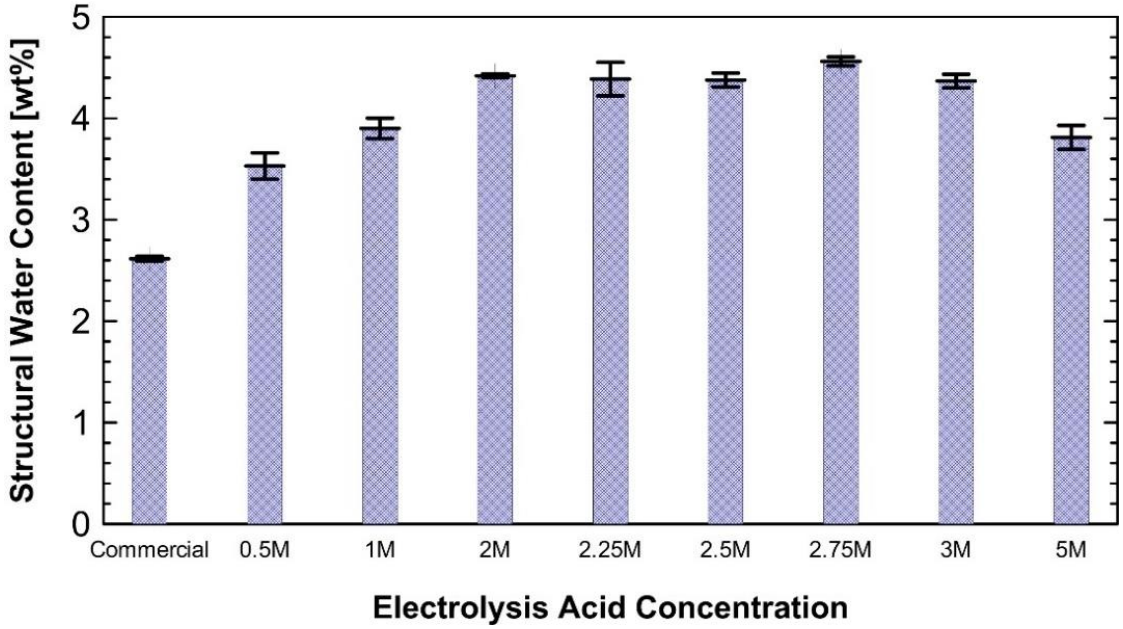

Figure 3.6 Structural water content of EMD as a function of acid bath concentration in comparison to a commercial EMD.

In order to further understand the effect of Pr and $W_{structural}$ on the structure of EMD, the d-spacing of the samples were calculated from the position of the (110) peak using Bragg's law of diffraction (see Equation 2.2) and are shown in Figure 3.7. It appears that decreased Pr and increased $W_{structural}$ initially leads to larger values of d_{110} and a maximum d_{110} of about 0.41 nm is obtained for C_{H2SO4} = 2 M. For C_{H2SO4} > 2 M, a decrease in the d_{110} spacing is observed. These results show that up to C_{H2SO4} = 2 M, which yields pure EMD (γ-MnO_2) phase, the d_{110} planes expand, presumably because of higher water content. This confirms a recent report that has revealed that water molecules are more tightly packed in EMD samples with a higher percentage of ramsdellite [111]. The combination of these two factors could further facilitate the protonic conductivity of the EMD prepared in 2 M acid.

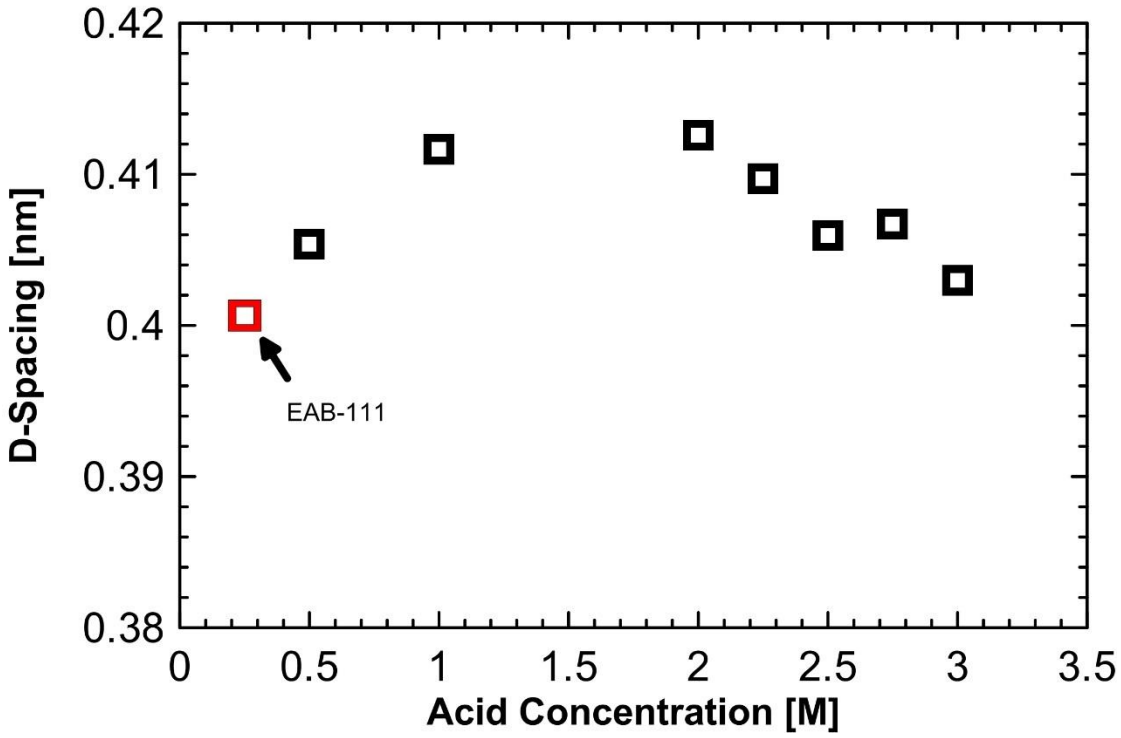

Figure 3.7 D-spacing of EMD samples prepared vs. the electrolysis acid concentration in comparison to a commercial EMD.

For further physical characterization of the EMD samples produced, BET and BJH measurements were performed on the commercial and samples prepared in 0.5 M $\leq C_{H2SO4} \leq$ 2.5 M. The other samples were not investigated by BET and BJH because of their poor electrochemical performance as it will be revealed in the next section. Figure 3.8 (a) and (b) show the N_2 adsorption-desorption isotherms and the desorption BJH pore distribution curves of the selected EMD samples, respectively. The hysteresis loop of samples prepared in 0.5 M $\leq C_{H2SO4} \leq$ 2.5 M are all in the p/p^o range of $0.4 \leq p/p^o \leq 0.9$, while the Erachem sample's hysteresis loop extends further and is far more pronounced at higher p/p^o. This characteristic may hint at the fact that the Erachem EMD is more mesoporous compared to the in-house synthesized EMDs [112]. Furthermore, the hysteresis loop is much wider for the samples with a broader pore size distribution due the capillary condensation and evaporation that occurs within samples with larger pores, requiring lower pressures for desorption. However, it is also important to note that the existence of larger pores as well as the flat end of the hysteresis for the in-house synthesized samples may indicate a much more complex channel system (of large and small pores) in comparison to the Erachem EMD [112].

Figure 3.8 (a) and (b) show the average BET surface area and the average BJH adsorption pore diameter, respectively. Even the samples produced in the lowest acid concentration (i.e. 0.5 M H_2SO_4) display an approximately 86% increase in the surface area ($SA_{EMD} \approx 77.6$ m^2 g^{-1}_{EMD}) in comparison to Erachem EMD ($SA_{EMD} \approx 41.7$ m^2 g^{-1}_{EMD}). The highest surface area samples were synthesized with C_{H2SO4} = 2 and 2.5 M, having SA_{EMD} values of 86.4 and 99.8 m^2 g^{-1}_{EMD}, respectively, which is a 150% improvement over the Erachem EMD. Biswal *et al.*'s work on

improving EMD's surface area (through incorporation of anionic surfactants into the electrolysis process) [85], has shown that a higher surface area can lead to improved cycling capability of the EMD due to increased contact between the EMD surface and reducing molecules intercalating into the material. Further analysis of the results of Biswal *et al.*'s work indicates that a 20% increase in surface area may lead to at least 2x higher capacity after approximately 20 cycles.

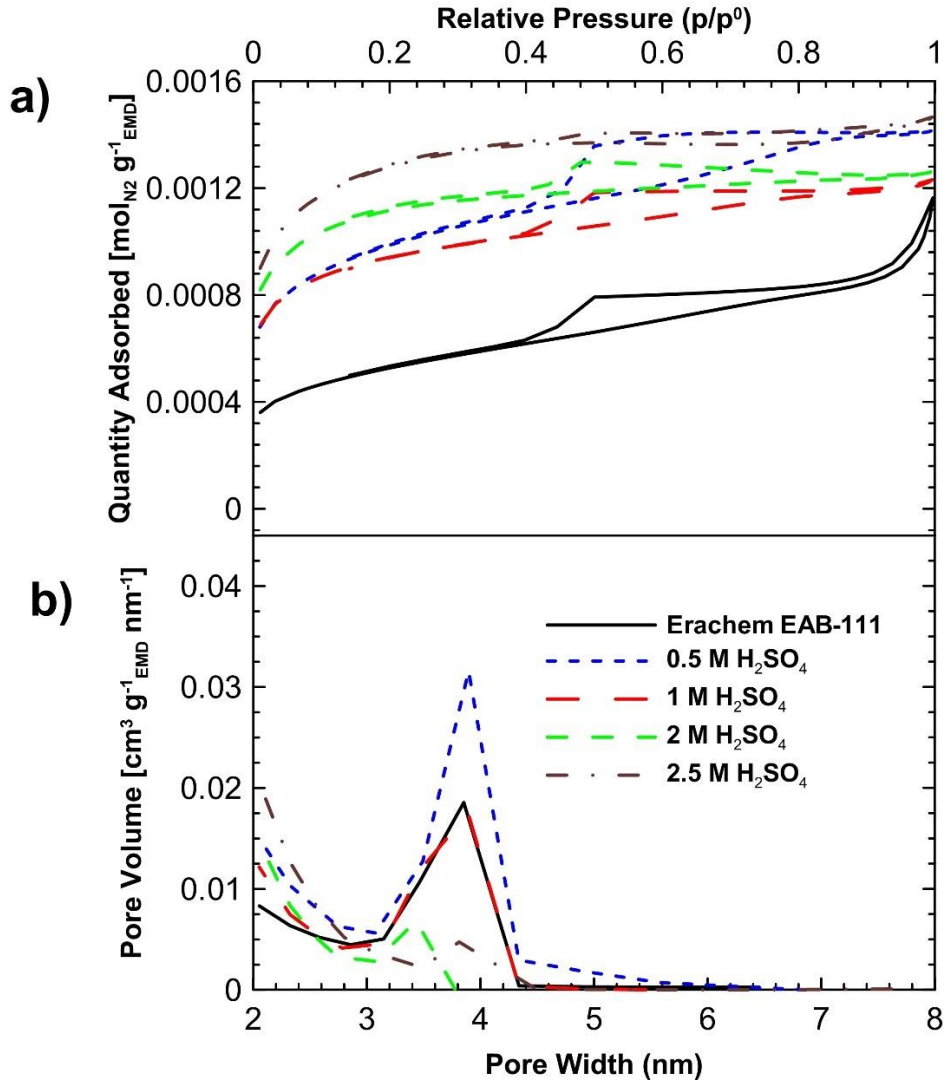

Figure 3.8 (a) BET adsorption/desorption isotherms and (b) BJH desorption pore size distribution of EMD samples prepared at different acid concentrations.

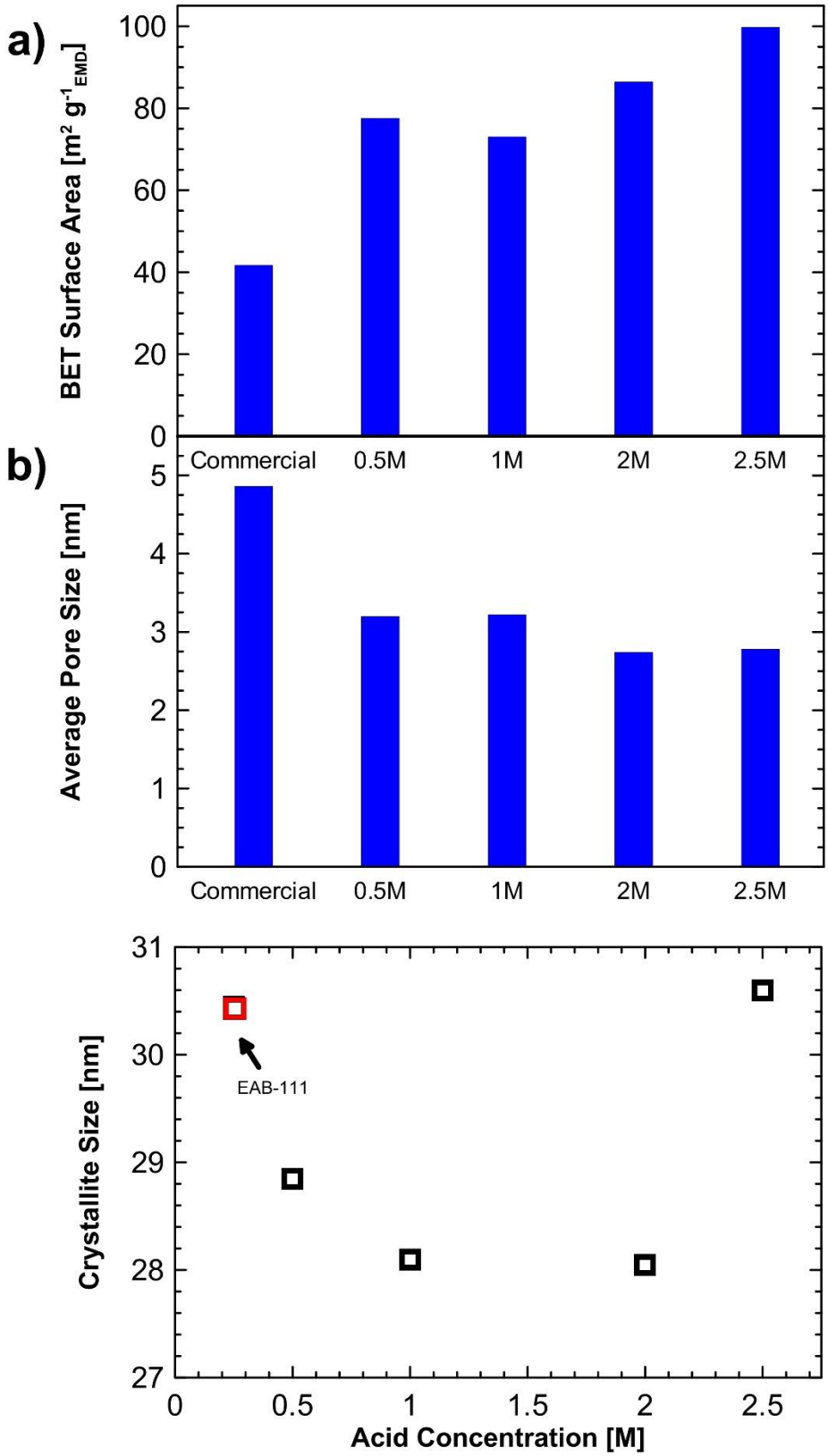

Figure 3.9 (a) BET surface area, (b) BJH desorption pore size, and (c) crystallite size of EMD samples prepared at different acid concentrations.

Figure 3.8 (c) displays the crystallite size (τ) of the various EMD samples calculated from the position of the (110) peak using the Scherrer equation, where λ is the x-ray wavelength (0.154 nm) and β is the broadness of the peak at the halfway point (see Equation 3.3).

$$\tau = \frac{0.9\lambda}{\beta \cos(\theta)}$$ **Equation 3.3**

EMD synthesized in 2 M H_2SO_4 or less has decreasing crystallite size with increasing acid concentration (increasing surface area). The crystallite size of EMD synthesized in C_{H2SO4} = 2.5 M has a crystalline size comparable to that of the commercial EMD. The high surface area of this sample could therefore be due to the additional intergrowth of other EMD phases. It is also important to note that the samples prepared with 2 M and 2.5 M H_2SO_4, which have the highest surface area, also have the smallest pore sizes of 2.74 and 2.78 nm, respectively. EMD samples with small pore sizes have been reported to have a higher resistance (an 80% decrease in pore size increased ohmic resistance by approximately 3×), when measured by electrochemical impedance methods [113]. Therefore, there may be an optimum SA_{EMD} with respect to pore size where the best performance in terms of resistance and cycling can be obtained.

3.2.1.2 Effect of Acid Concentration on the Electrolysis Process

It is important to note some of the challenges faced with EMD synthesis at such high acid concentrations. Figure 3.10 (a) shows the titanium anode after deposition in 1 M H_2SO_4 and 10 M H_2SO_4. Figure 3.10 (b) shows the current efficiencies of the EMD synthesis at the electrolysis acid concentrations studied. The decreasing trend of the current efficiency is related to the degradation of the titanium anode inside the acidic environment. At the potentials and pH at

which the electrolysis cell was operating at, TiO^{2+} and TiO_2^{2+} species could form [114] (see Figure 3.11), however the titanium is often covered with a fine layer of EMD that forms instantly as soon as a current is applied. Therefore, the degradation (or dissolving) of the titanium was not fully visible at the acidic concentrations studied, however, it was clearly observed at very high acid concentrations (10 M H_2SO_4).

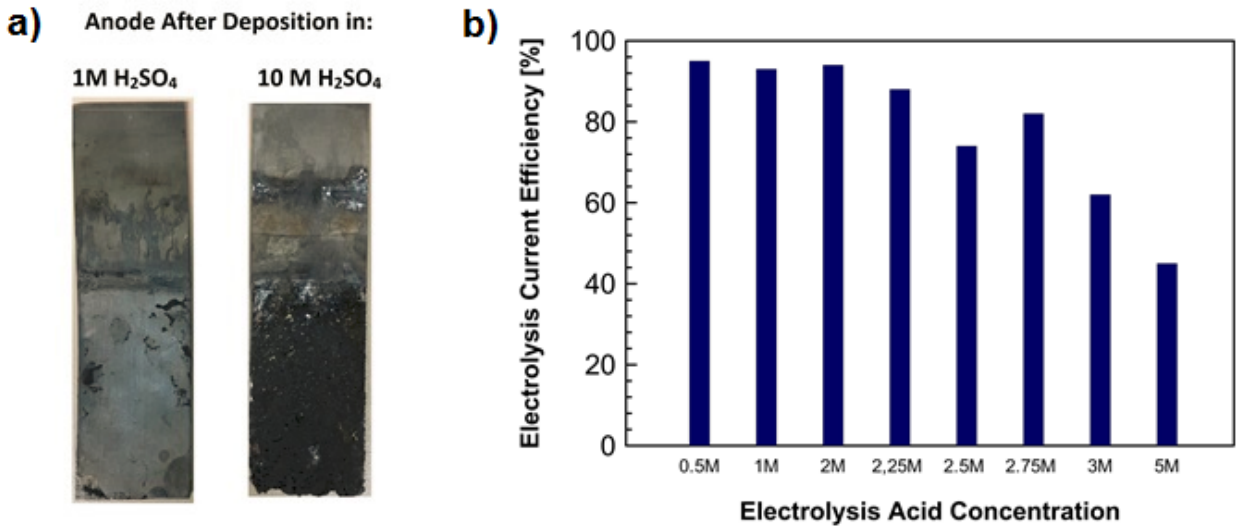

Figure 3.10 (a) Titanium anode after electrolysis in 1 M H_2SO_4 (left) and 10 M H_2SO_4 (right); (b) current efficiency vs. the electrolysis acid concentration.

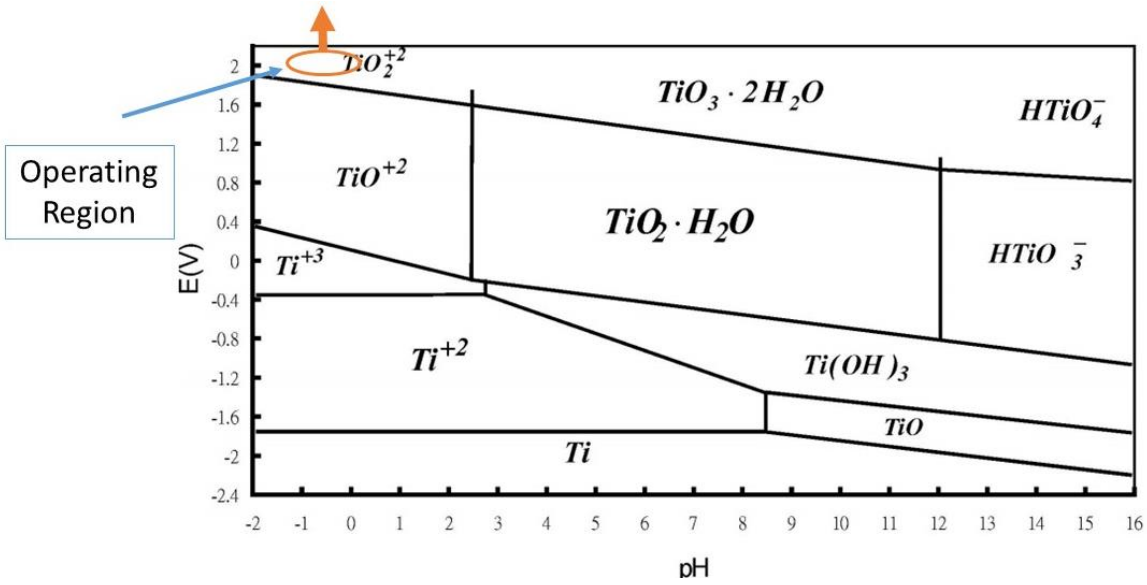

Figure 3.11 Modified Pourbaix diagram of titanium. [114]

3.2.1.3 Electrochemical Characterization of EMD

For each EMD sample, 2-4 cells were constructed and results were averaged with appropriate standard deviations calculated. Figure 3.12 (a) and (b) show the typical 1st and the 60th discharge/charge cycles for the commercial EMD and selected prepared EMD samples. The area between the discharge and charge voltage curves correspond to the energy loss that occurs between the charge and discharge processes (see Equations 3.4 and 3.5).

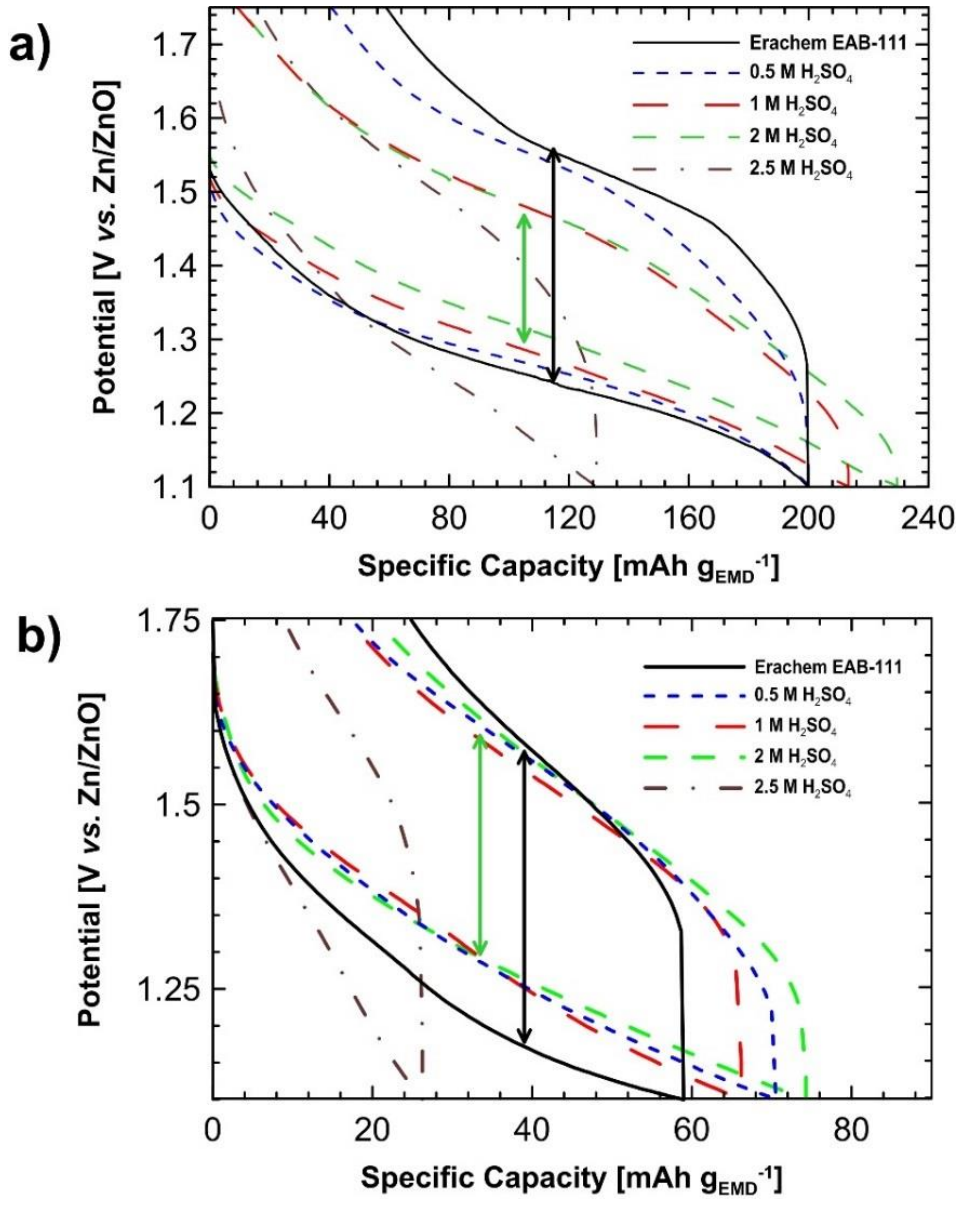

Figure 3.12 Voltage/capacity profiles of the electrochemical cells with the EMD samples prepared at different acid concentrations and Erachem EAB-111 for (a) the 1st cycle, and (b) the 60th cycle.

$$Energy = \int Voltage \times Specific\ Capacity$$

Equation 3.4

$$Energy\ Efficiency = \ EE = \frac{Energy_{discharge}}{Energy_{charge}} \times 100\%$$

Equation 3.5

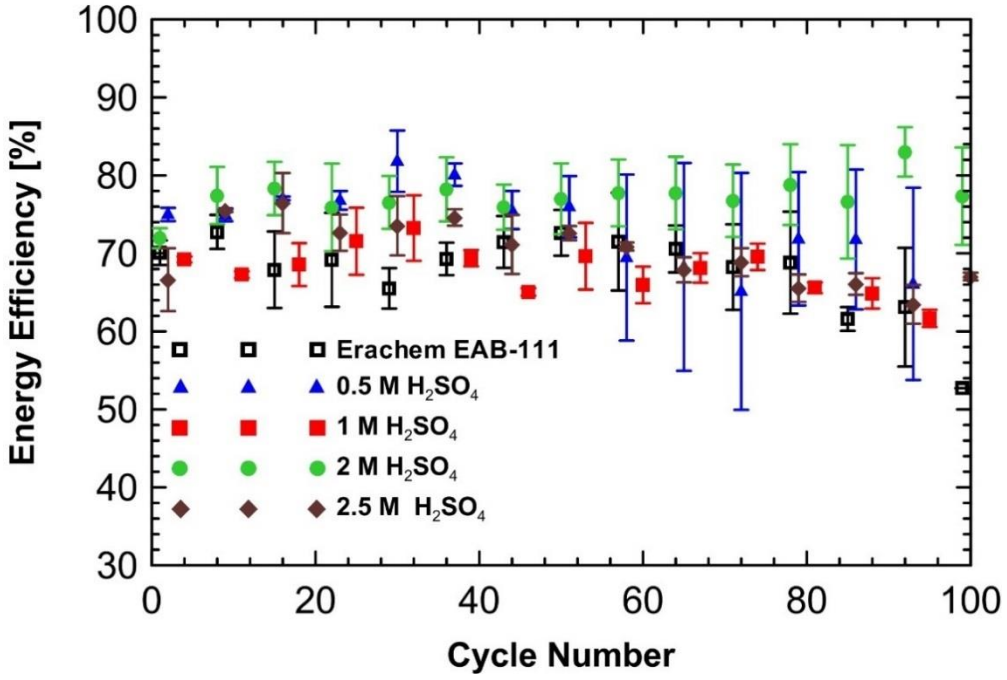

Figure 3.13 *Energy efficiency of the EMD samples prepared at different acid concentrations, and Erachem EAB-111 over 100 cycles.*

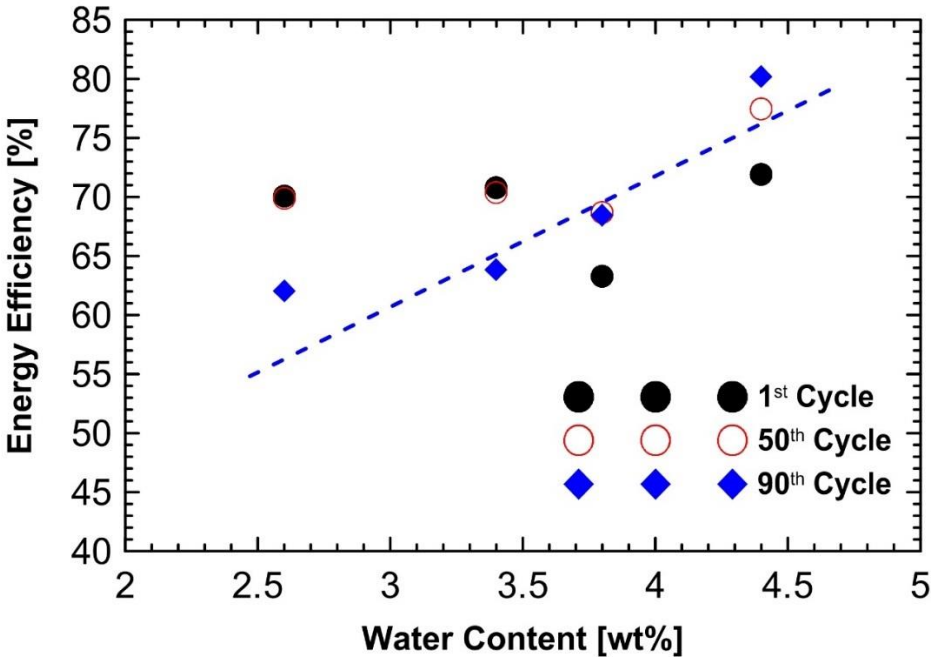

Figure 3.14 *Energy efficiency of electrochemical cells for EMD vs. the structural water content for the 1st, 50th, and 90th cycle.*

The 1st discharge/charge reveals that in-house samples all show smaller voltage polarization differences between the discharge and charge steps compared to the commercial sample. This difference, however, changes during the cycling (see Figure 3.12 (b)). Furthermore, by plotting the energy efficiency of all 100 cycles, it can be observed that the in-house EMD samples show, in general, higher (≥ 20%) energy efficiency compared to the commercial EMD (see Figure 3.13). Additionally, EMD produced in the 2 M acid bath shows a higher efficiency (≥ 30%) within the range of standard deviations especially in the later cycles. It can also be seen that the energy efficiency of the cells fluctuates significantly with cycling. Despite the variabilities, the 2 M EMD sample shows a superior performance within the range of standard deviation. Figure 3.14 shows the energy efficiency of the EMD samples with different water content for a number of different cycles. The sample prepared in C_{H2SO4} = 2 M shows the highest energy efficiency at each of the selected cycles. These results indicate that the water content of the EMD may have an important effect on the energy efficiency of the EMD materials.

Figure 3.15 shows the cycling capability of the cells for one hundred cycles at a rate of C/10 with their standard deviation. The cycling performance of Erachem EMD is shown by a best polynomial fit to the data of six cells for clarity. All the tested EMD samples lose capacity in two apparent stages: i) a rapid capacity loss during the first 30 cycles followed by ii) a more gradual capacity loss. The rate of capacity fade is observed to be slower after 30 cycles for EMD synthesized in C_{H2SO4} = 2M. Cells using this EMD are able to maintain a minimum capacity of approximately 70 mAh g^{-1}_{EMD} up to the 100th cycle. However, commercial EMD does show the highest initial capacity. This property is particularly important for primary batteries which indicates that

commercial Erachem EMD has been optimized for primary battery applications. However, Erachem EMD also displays a more significant capacity decline (average capacity of 40 mAh g^{-1}_{EMD} is reached by the end of this cycling period). The specific capacity of the commercial EMD product drops below that of the 2 M EMD after approximately the 50th cycles and below samples prepared in 0.5 M and 1 M H_2SO_4 after approximately the 70th cycle. The EMD samples synthesized under very high acidic conditions (2.5 M H_2SO_4), which possibly contains the hollandite phase in addition to EMD, has the lowest overall performance. The initial capacity of these cells are at approximately 50% of the regular commercial EMD capacity, and their capacity drops to approximately 15 mAh g^{-1}_{EMD} after 100 cycles. This low capacity was observed for all the samples with additional hollandite phase, hence these samples were not examined in greater detail.

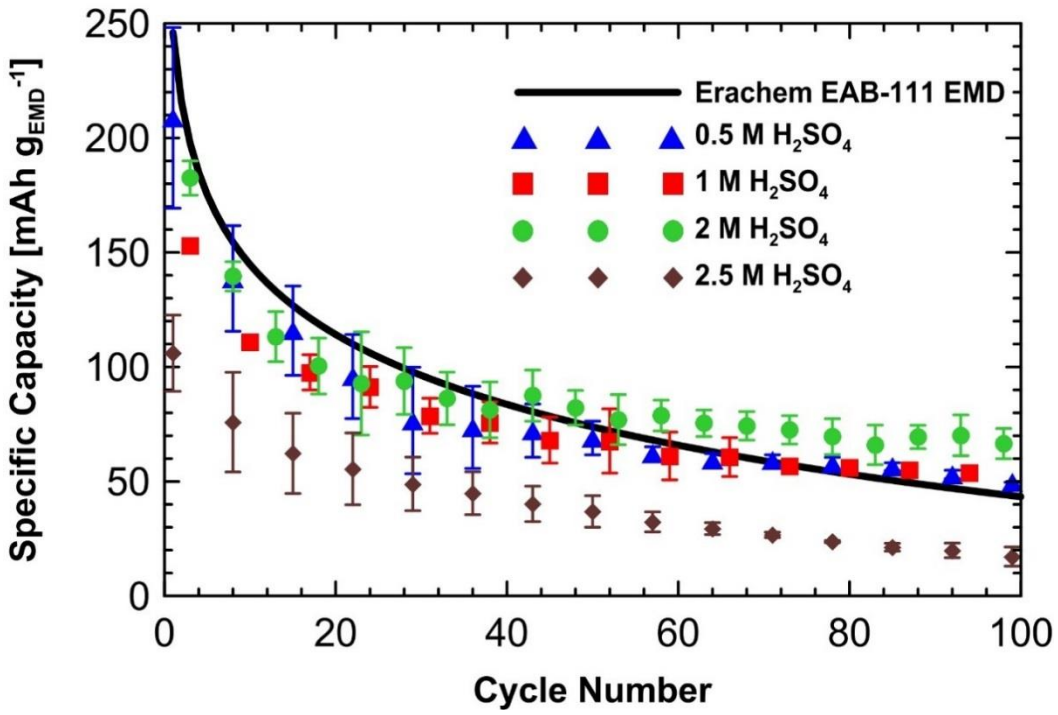

Figure 3.15 Cycling performance of the EMD samples prepared at different acid concentrations, and Erachem EAB-111 over 100 cycles.

The electrochemical impedance of samples synthesized in C_{H2SO4} = 2 M (best cycling performance) and commercial EMD sample were investigated in half-cells equipped with an Hg/HgO reference electrode and Ni mesh as the counter electrode. The impedance scans were obtained at the end of discharge and after the complete charge steps. Figure 3.16 (a)-(c) and (d)-(f) show the Nyquist plots and cycling behavior of Erachem EAB-111 and 2 M EMD, respectively. The Nyquist scans are shown for a number of selected cycles, typically where a sudden decrease in capacity (e.g., 20^{th} and 40^{th} cycles) occurs as well as the 80^{th} and 100^{th} cycle, where the cell's capacity reaches a steady state. The impedance data show in general two semi-circle loops which can be approximated by a series combination of two parallel R-C circuits. Figure 3.16 (g) shows an equivalent circuit of one R_s (electrolyte and contact resistance) component and two R_{ct} (charge transfer resistances) components. The values of these resistances are estimated from the intercepts of the semicircles on the EIS plots. Table 3.1 and Table 3.2 summarize these resistances at the end of discharge and charge for the commercial and 2 M EMD samples, respectively.

While the variation of R_s during the 100 cycles is negligible (< 20% variation) for both cells (indication of the good electrolyte and contacts throughout the cycling process), the two R_{ct} values (R_{ct1} and R_{ct2}) appear to increase with cycling. The R_{ct} is related to the reciprocal of the exchange current density [115], a measure of the equilibrium reaction rate or the surface reactivity. The loss of surface reactivity, i.e., growth of R_{ct}, coincides with the capacity loss during the electrochemical cycling. This indicates that the surface of EMD is losing reactivity and is thus being replaced by less reactive manganese dioxide phases. Furthermore, while the commercial EMD shows one fully developed semi-circle, the second semi-circle is smeared by the diffusion

tail of the EIS. The 2 M EMD sample, however, does show two fully developed semi-circles during the entire 100 cycles. Furthermore, the EIS data of both samples show an increase in the values of R_{ct2} with cycling but it is easier to observe it in the 2 M EMD sample because it has a better defined second semi-circle. The presence of the second semi-circle may be attributed to a difference in the water content of the two samples as R_{ct} has also been related to the "water activity" of EMD [116]. However, the 2 M EMD sample has a higher R_s and R_{ct1} value, which could be due to its smaller pore size that have been reported to have increased resistance [113]. As a result, it appears that the porosity and water content of the EMD may have a larger effect on the charge transfer of the EMD material inside a cell, and moreover the impedance factors R_s and R_{ct1} have little effect on the overall cycling ability.

Table 3.1 Impedance parameters after the potentiostatic charge.

	Commercial EMD			2M EMD		
Cycle #	R_s/f [Ω/kHz]	R_{ct1}/f [Ω/kHz]	R_{ct2}/f [Ω/kHz]	R_s/f [Ω/kHz]	R_{ct1}/f [Ω/kHz]	R_{ct2}/f [Ω/kHz]
1	0.0055	0.921	1.18	0.095	1.87	2.27
20	0.0059	1.37	7.72	0.071	1.44	5.31
40	0.0057	1.19	8.29	0.077	1.51	5.73
60	0.0074	1.48	9.88	0.075	1.66	6.31
80	0.0056	1.45	10.5	0.077	1.56	5.31
100	0.0050	1.45	16.5	0.077	1.66	7.11

Table 3.2 Impedance parameters after the galvanostatic discharge.

	Commercial EMD			2M EMD		
Cycle #	R_s/f [Ω/kHz]	R_{ct1}/f [Ω/kHz]	R_{ct2}/f [Ω/kHz]	R_s/f [Ω/kHz]	R_{ct1}/f [Ω/kHz]	R_{ct2}/f [Ω/kHz]
1	0.0016	0.801	1.96	0.085	0.915	1.46
20	0.0010	1.42	1.49	0.076	1.54	1.61
40	0.0005	1.38	2.86	0.079	1.83	1.59
60	0.0051	1.50	3.36	0.086	2.03	1.92
80	0.0026	1.38	-	0.084	2.02	2.68
100	0.0050	1.36	-	0.085	2.05	2.55

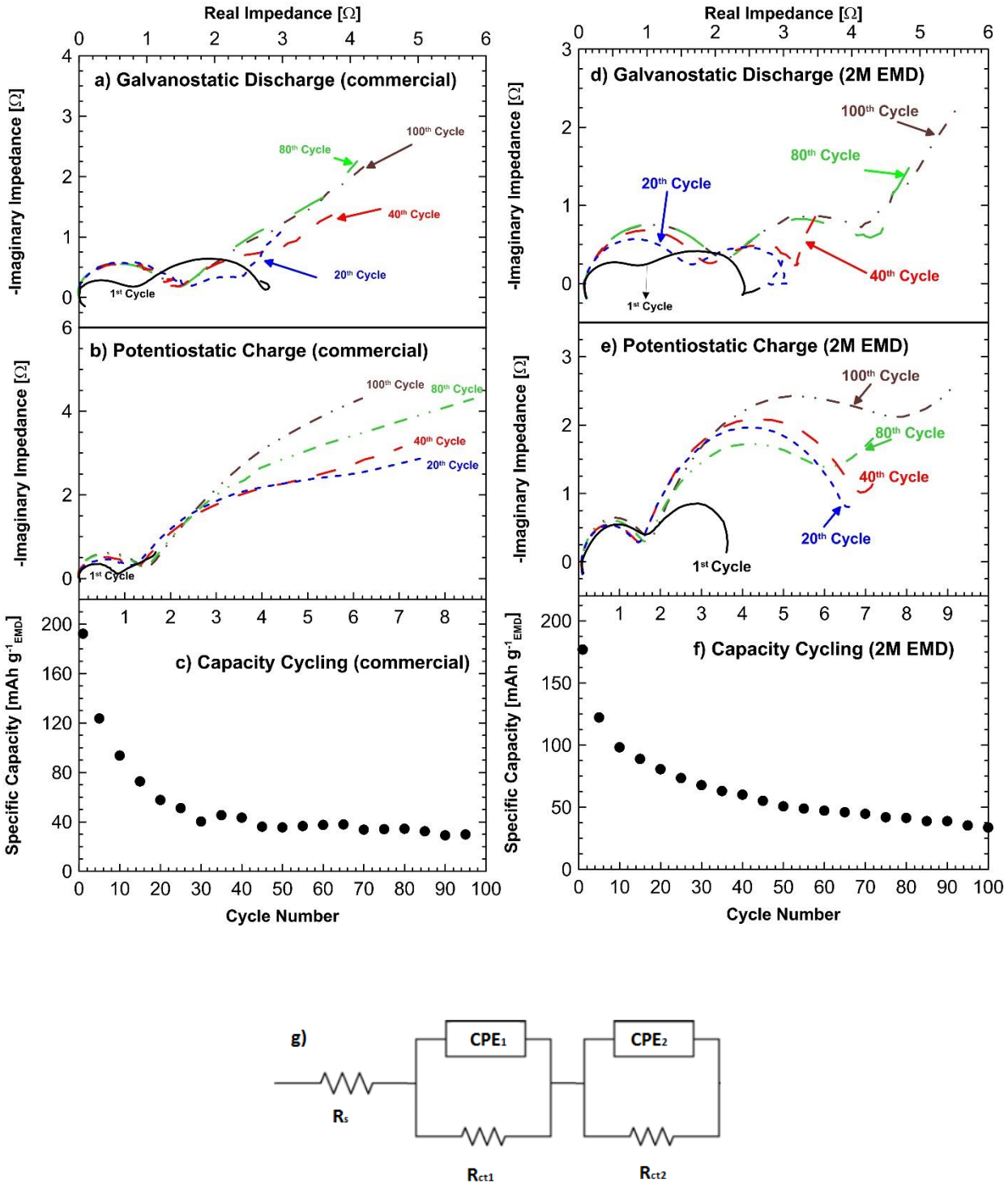

Figure 3.16 *Nyquist plots of Erachem EAB-111 and 2 M EMD cells at selected cycles (a), (d) after galvanostatic discharge, (b), (e) after potentiostatic charge; (c), (f) the specific capacity of the cells over 100 cycles; (g) the equivalent circuit for the half-cell experiments.*

3.2.1.4 Physical Characterization of Cycled EMD

Figure 3.17 shows the XRD diffraction patterns of the cathode electrodes after the 100th cycle in a fully charged state. The diffractograms reveal two major developments: 1) the EMD phase has been partially converted to other MnO_2 phases, hollandite and birnessite; 2) irreversible phases like hausmannite (Mn_3O_4) and hydrohetaerolite ($ZnMn_2O_4$) appear to have been formed as well. The first effect is related to the observation that the characteristic EMD peak (110 at $2\theta \approx 22^o$) has almost disappeared in all of the cells analyzed. For the Erachem EAB-111 sample (which had the lowest capacity after 100 cycles), a peak appears close to EMD's (110) peak, however, it is hard to assign this to either EMD or hausmannite due to the defects and twinning of the sample. Furthermore, hausmannite peaks appear to be more prominent in the cycled commercial sample and EMDs synthesized in C_{H2SO4} of 0.5 M and 1 M compared to the EMD synthesized in 2 M acid. The hydrohetaerolite phase appears to be more prominent in the cycled 2 M EMD. These results indicate that any zinc crossover through the separator, which happens in some cells and can potentially be alleviated by adequate separators, is not the main reason for the capacity fade in the EMD/Zn cells. The XRD pattern of cycled 2.5 M EMD shows MnO_2 peaks which can be matched with those of the hollandite phase. The hausmannite and hydrohetaerolite peaks are moreover almost non-existent in this sample.

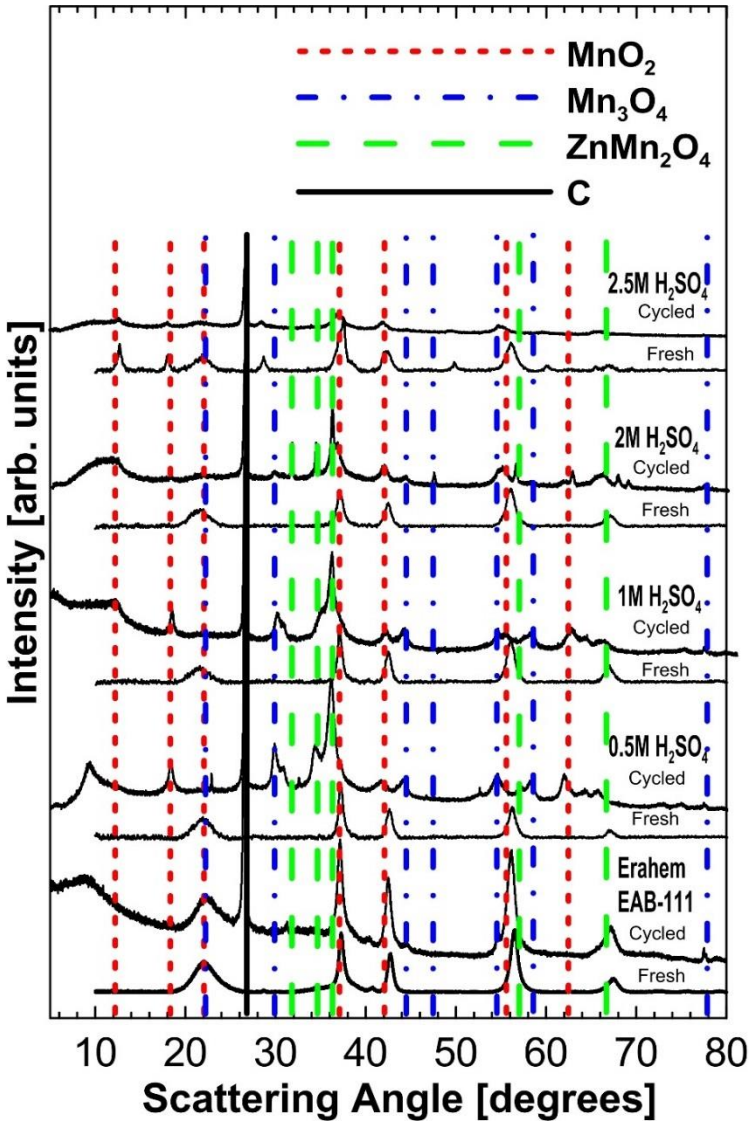

Figure 3.17 XRD profiles of fresh and cycled (100 charge/discharge) EMD samples prepared at different acid concentration, and Erachem EAB-111.

Another reason for capacity fade could be the loss of EMD's structural water. A hypothesis was made that water loss may occur as a result of disruption of the EMD phases which occurs during the dissolution-precipitation of manganese dioxide during the electrochemical cycling. Structural water compensates for cation vacancies or partially reduced Mn^{4+} ions in fresh EMD samples. In analyzing loss in structural water, an assumption was made that the water could be replaced with

cations present in the electrolyte (e.g., K^+) or dissolved manganese ions. To obtain the water loss over the structural water loss region (120°C < T < 300°C), TGA was performed and an estimated weight loss of the CMC additive (W_A) was subtracted in order to find $W_{structural}$. Figure 3.18 shows the $W_{structural}$ of the EMD samples after electrochemical cycling. Data shows that all samples have gone through a water loss of about 18% to 47%. These results corroborate with the significant changes of the EMD XRD pattern, showing that formation of irreversible phases such as huasmannite and the loss of EMD phase are responsible for the capacity loss in the EMD/Zn cells.

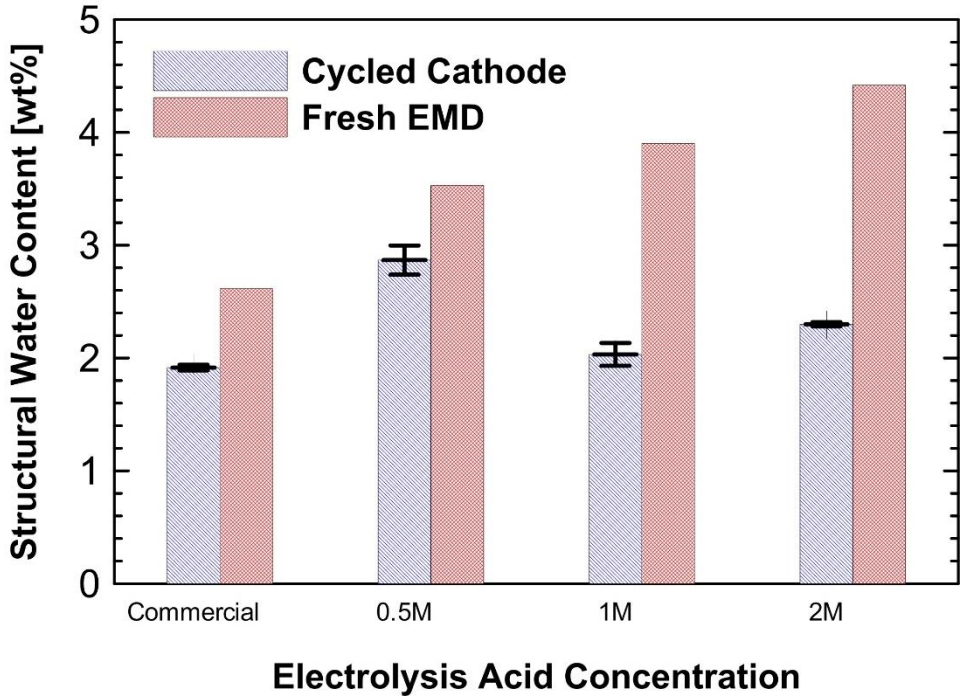

Figure 3.18 Structural water content of the EMD samples prepared at different acid concentration, and Erachem EAB-111 after 100 cycles compared to the fresh powder.

3.2.2 Current Density

In order to further fine-tune the synthesis parameters for high performing EMD, a higher and lower current density (0.0075 and 0.0175 A cm^{-2}) than the one investigated in the previous section (0.0125 A cm^{-2}) were studied at the optimum acid concentration (2 M H_2SO_4). Figure 3.19 displays the obtained XRD diffractograms obtained from each of the samples. Although the intensity of some of the peaks seems to differ between the samples, the positions of the peaks display no shift and no additional peaks appear at lower or higher current densities.

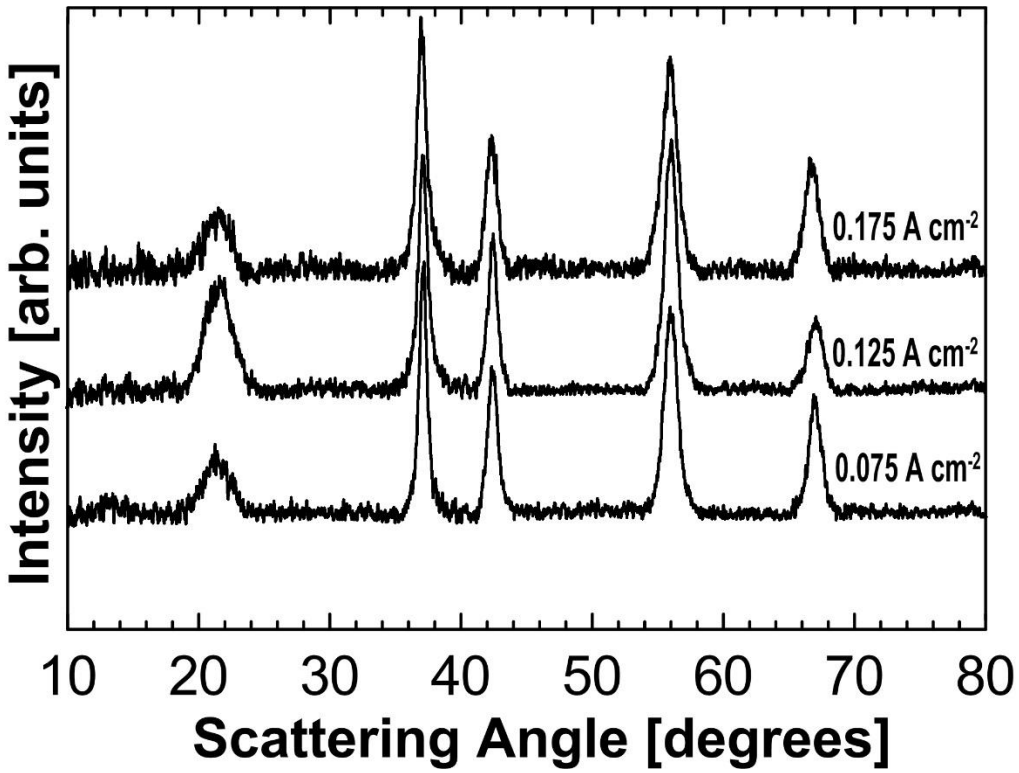

Figure 3.19 *XRD spectrums of EMD samples prepared under different current density conditions.*

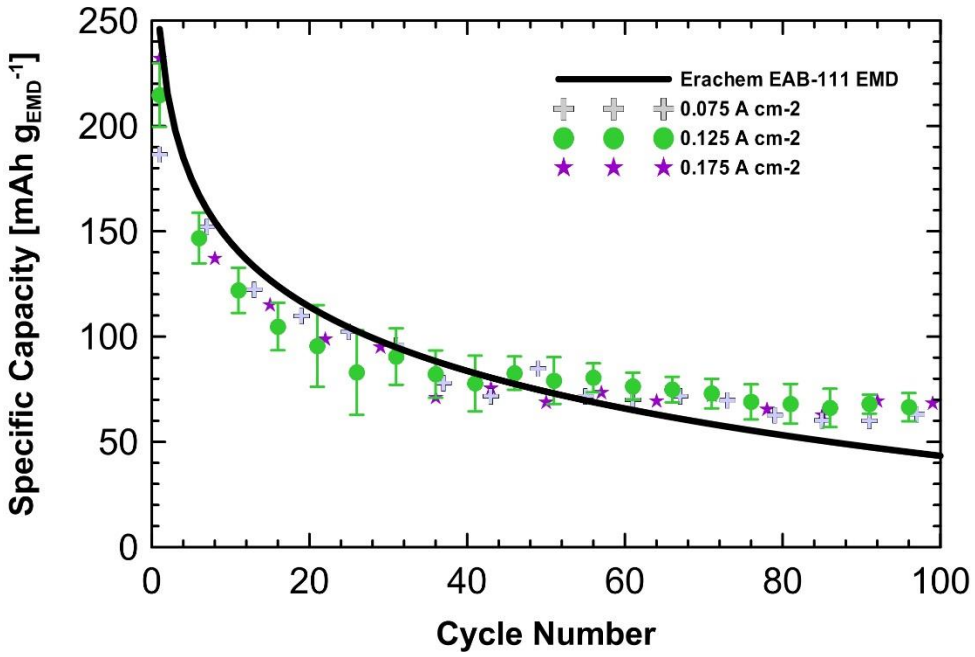

Figure 3.20 Capacity cycling of EMD samples prepared under different current density conditions, and Erachem EAB-111 over 100 cycles.

Furthermore, cycle tests of the samples inside flat-plate cells display no difference in performance (see Figure 3.20). These samples were not investigated any further, and it was concluded that the electrolysis current density has a negligible effect on the synthesized EMD products made for rechargeable batteries.

Lower current densities (0.0075 and 0.0125 A cm^{-2}), however, do display an enhanced EMD synthesis current efficiency for the actual synthesis step itself. Figure 3.21 shows the current efficiencies of the synthesis for the three aforementioned samples. As it can be seen, current efficiency decreased by approximately 10 percent when synthesis was performed at 0.0175 A cm^{-2} (82%) in comparison to the current efficiencies of the electrolysis experiments performed at 0.0075 and 0.0125 A cm^{-2} (91% and 94%, respectively).

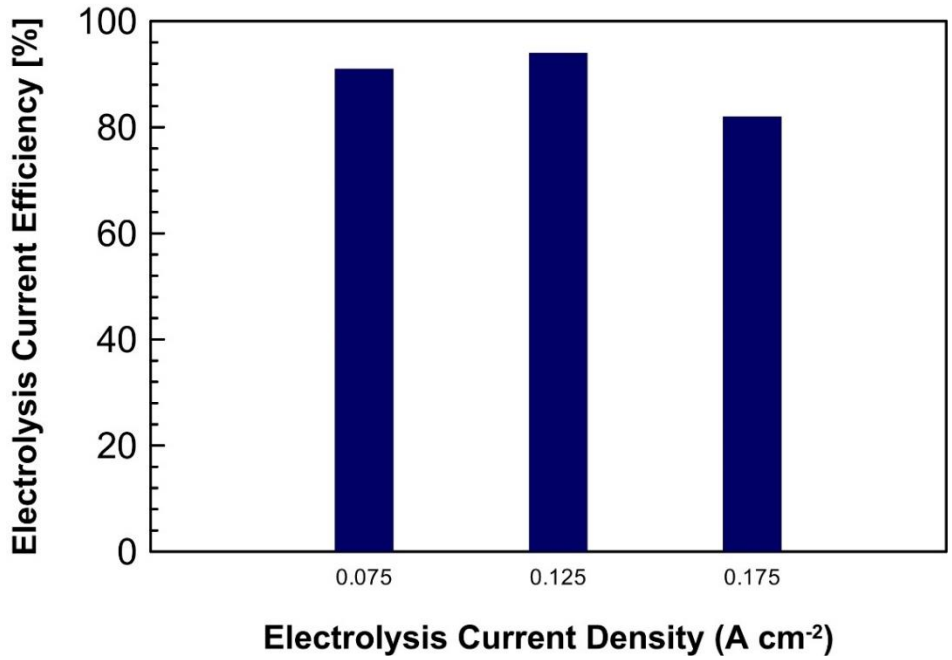

Figure 3.21 Current efficiency vs. the electrolysis current density.

3.3 Other Works

Table 3.3 summarizes some of the other work done for this section of the thesis.

Table 3.3 Summary of miscellaneous work done for improving acidic EMD synthesis.

Parameters Examined	**Observations**
Acid Type (2 M Nitric Acid)	• Very poor cycling performance (see Figure 3.22 (a)) ○ Both cell prepared approached failure after ~ 50th cycle
"Doping" (Ti, Co, Fe) *Inside 1 M H_2SO_4* *At 0.0125 A cm^{-2}*	• Too much of the dopant salt (higher than 3% of the total electrolyte content) inhibited oxidation of Mn^{2+} ○ Any iron salt addition completely inhibited manganese oxidation • Preliminary cycling results of titanium and cobalt "doping" showed no true improvements (see Figure 3.22 (b)) • Proper characterization protocols to provide proof of "doping" could not be made
Temperature *Inside 1 M H_2SO_4* *At 0.0075-0.0175 A cm^{-2}*	• High overpotentials occured when depositing EMD at lower temperatures (~50 ^{o}C) • Examination of temperature higher than 95 ^{o}C required a pressurized cell and was therefore not attempted

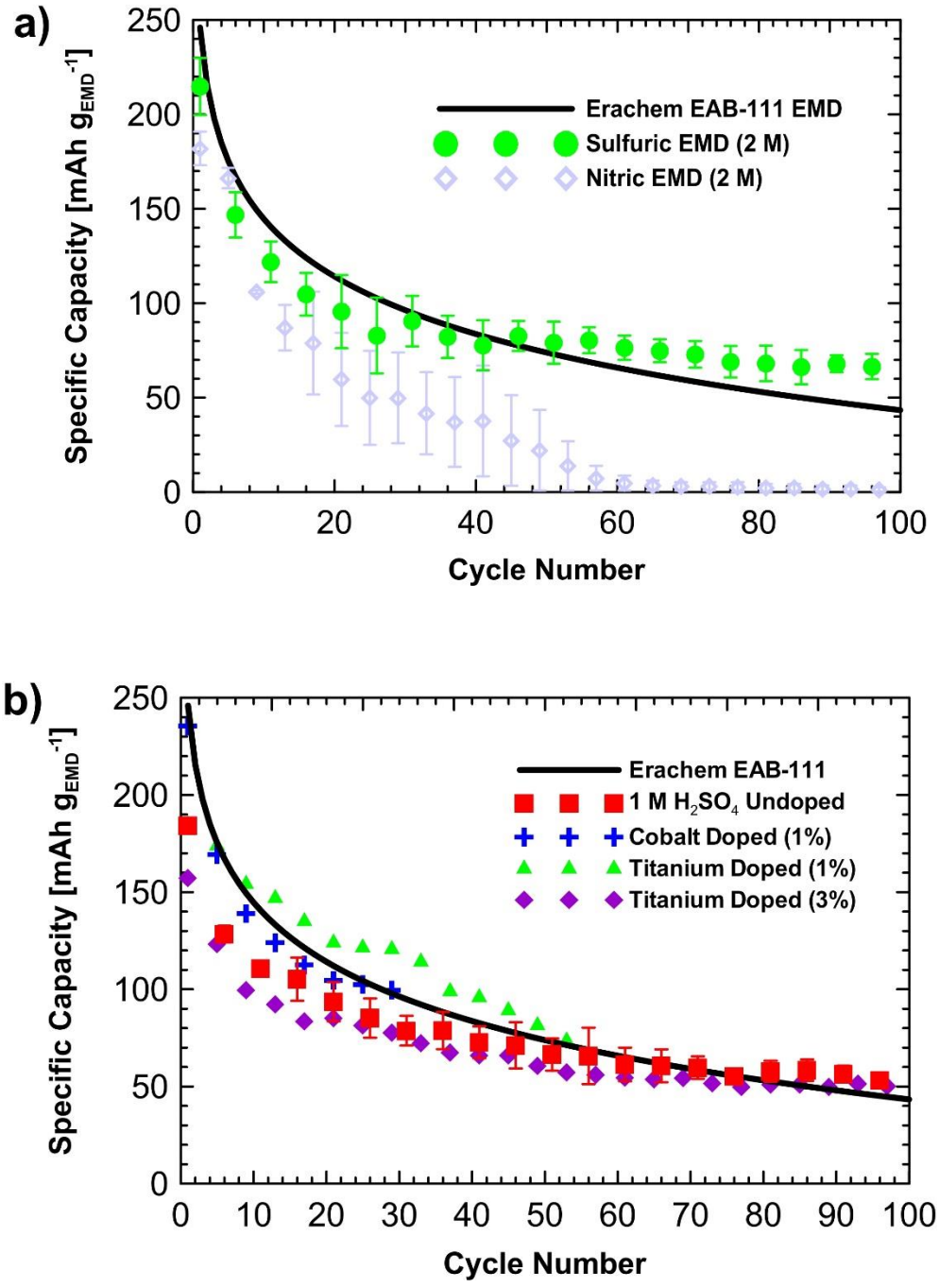

Figure 3.22 Cycling performance of (a) EMD synthesized in nitric acid, and (b) Ti and Co "doped" EMD in comparison to commercial EMD.

Chapter 4. Alternative Pathways for EMD Synthesis: Results and Discussion

4.1 Chemically Synthesized MnO_2 as Cathode Material for Rechargeable Alkaline Batteries

4.1.1 Physical and Electrochemical Characteristics of Ramsdellite, Hollandite, and Birnessite Phases of MnO_2

Chemically synthesized MnO_2 samples often yield pure and highly crystalline phases [100]. As previously mentioned, most of the battery-related research focus has been on using EMD [23], [26], [27], [38], [53], [56], [57], [59], [61]. Therefore, pure phases of α-MnO_2 (hollandite), R-MnO_2 (ramsdellite), and δ-MnO_2 (birnessite) (see Figure 4.1 (a) - (c)) were synthesized and tested for their cell performance. It is important to mention that at the time of writing this chapter, a recent article was published by Yadav *et al.* that discloses a highly rechargeable alkaline battery using δ-MnO_2 doped with bismuth and copper [117]. However, these batteries initiate discharging their 1^{st} electron at much lower depths of discharge (DoD) (< 1 V_{cell}). Copper appears to stabilize the Bi-doped birnessite phase and allow for repeated cycling of this material.

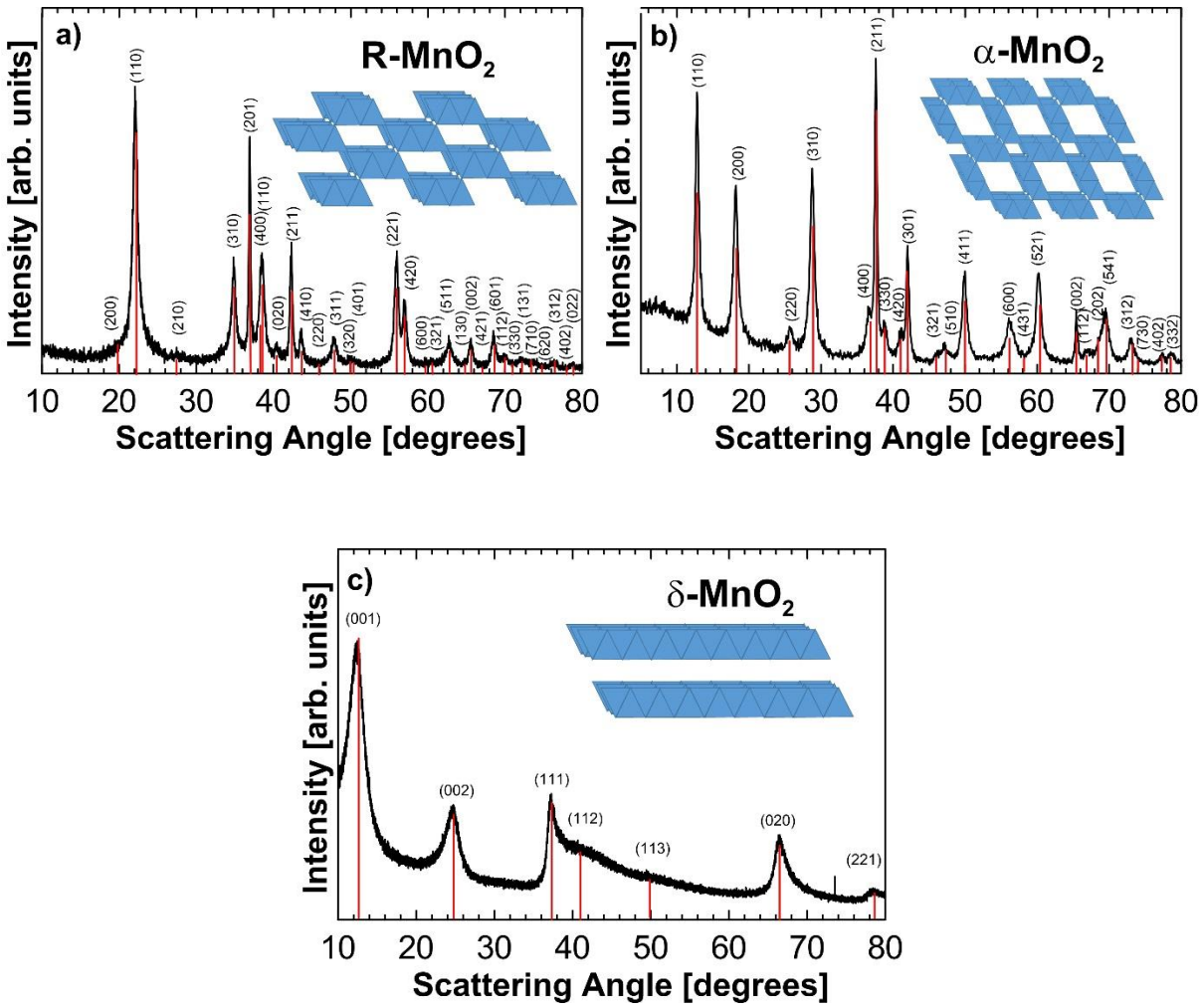

Figure 4.1 XRD patterns of the chemically synthesized MnO_2 phases: a) ramsdellite, b) hollandite, and c) birnessite.

Figure 4.2 displays the average initial specific capacities of the 1st electron discharge (in 9 M KOH electrolyte; DoD = 1.1 V_{cell}) of different MnO_2 products synthesized in-house. It is clear that EMD has the highest capacity. Single phases of hollandite and birnessite MnO_2, in particular, show only 15% of EMD's specific capacity above 1.1 V_{cell}.

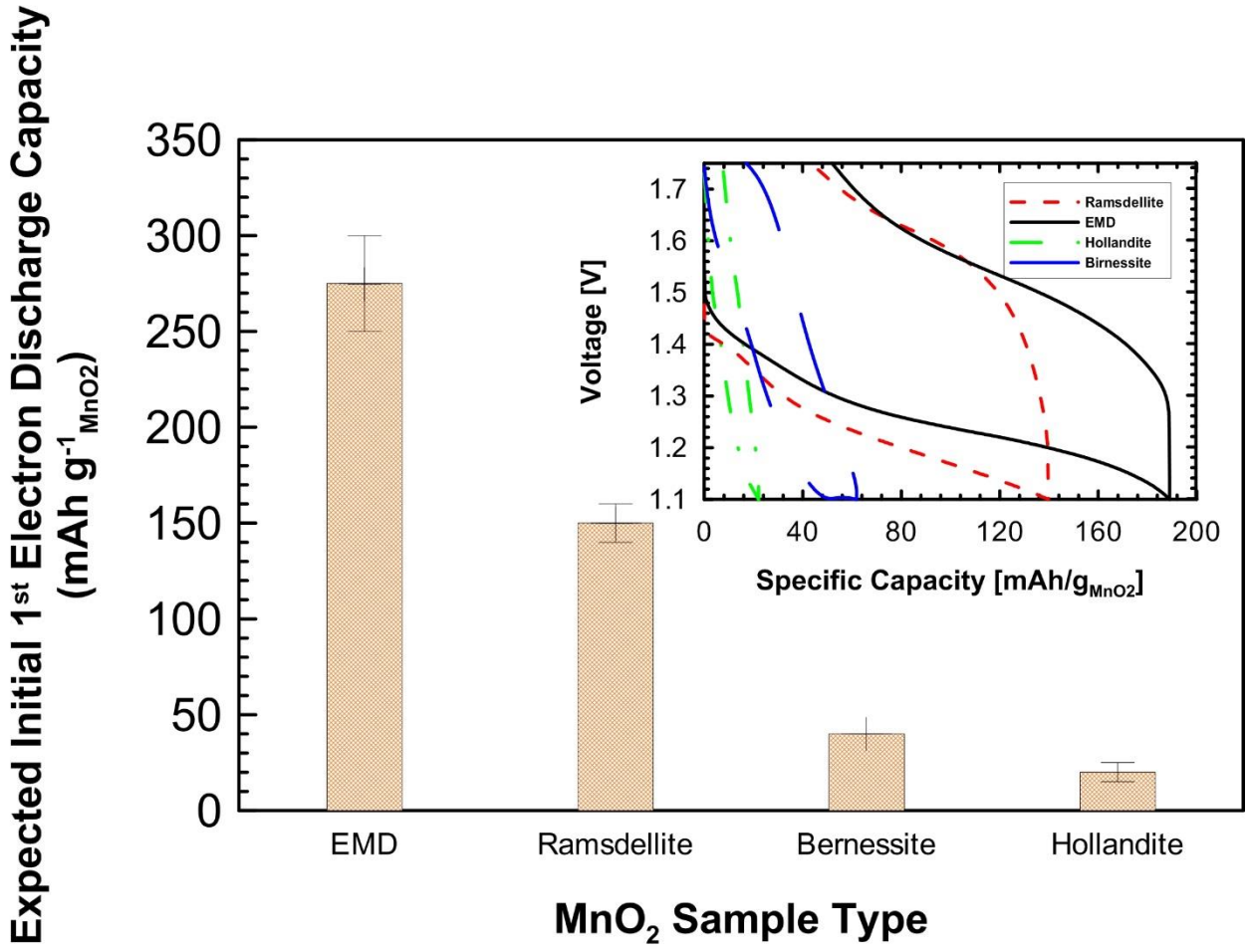

Figure 4.2 Measured initial first electron discharge capacities of MnO_2 samples shown for EMD, ramsdellite, birnessite, and hollandite phases in MnO_2/Zn alkaline cells using 9 M KOH electrolyte (DoD = 1.1 V_{cell}). The specific capacity vs. voltage curves are also displayed.

The lower capacity of highly crystalline MnO_2 phases may be due to the lower defect structure and structural water content of these phases (see Figure 4.3). Structural water is essential for proton intercalation and deintercalation during charge/discharge reactions [118]. Hollandite and ramsdellite have less than 1 $\%wt_{H2O}$ structural water content in comparison to EMD's range of 2.5 - 4.5 $\%wt_{H2O}$. Birnessite shows a rather large weight loss in the Reutschi proton loss region (~6%), this weight loss, however is possibly due birnessite possessing many loose water

molecules in it's interplanar spacing [100]. It appears that these loose water molecules don't achieve a high discharge capacity above 1.1 V_{cell}.

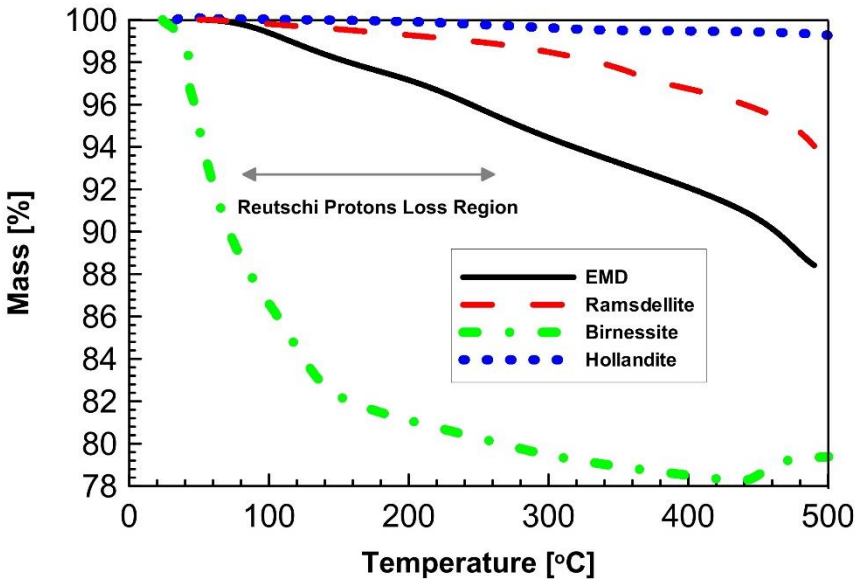

Figure 4.3 TGA thermograms of MnO_2 samples: EMD, ramsdellite, birnessite, and hollandite phases showing the water loss.

Ramsdellite's capacity of 140 mAh g^{-1}_{MnO2}, although half of EMD's capacity value of 300 mAh g^{-1}_{MnO2}, was still of high interest since it was above the target specific capacity of 100 mAh g^{-1}_{MnO2} for 100 cycles. Therefore, the electrochemical behaviour of this phase was examined in some details.

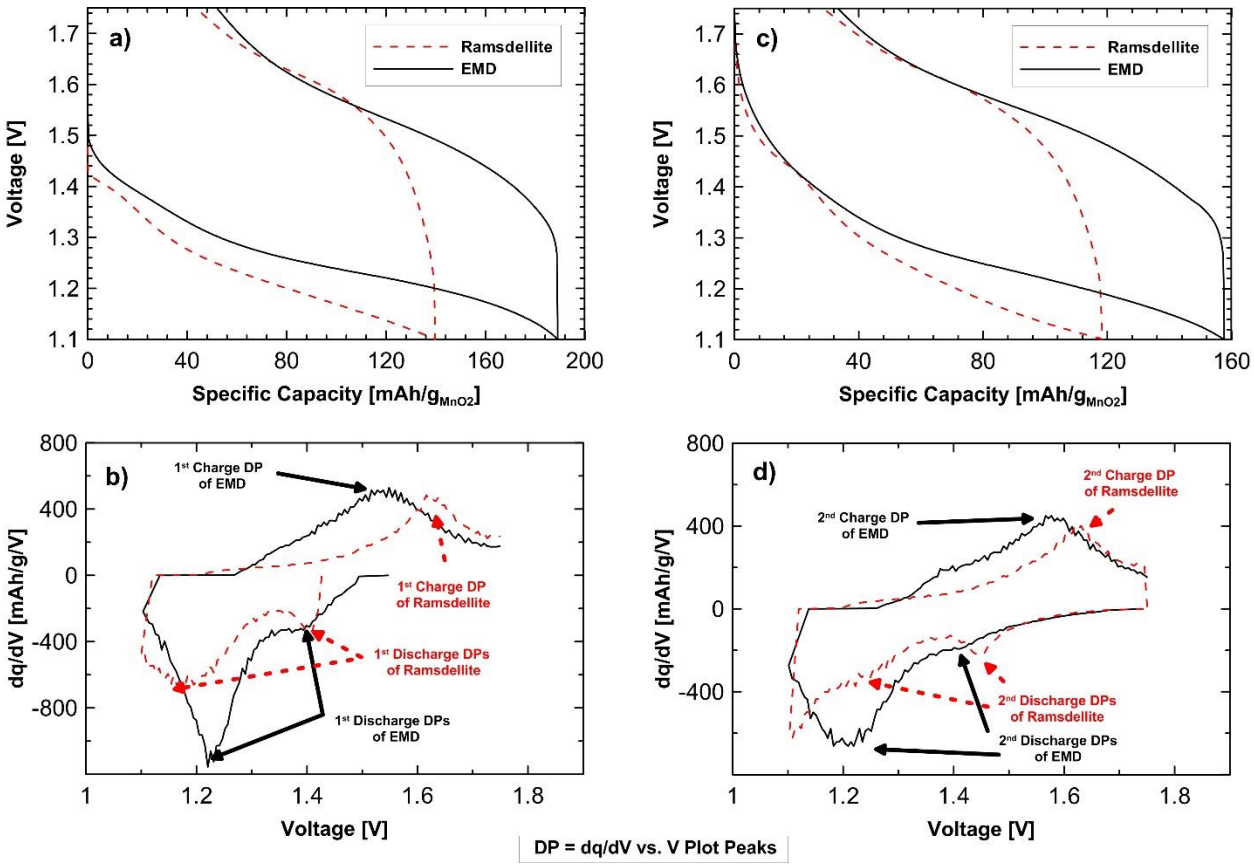

Figure 4.4 a) Specific capacity vs. voltage and b) specific inverse differential capacity vs. voltage of alkaline (in 9 M KOH electrolyte) cells using EMD and pure ramsdellite as the cathode material during the first cycle. c), d) Similar data as shown in a) and b) but for the second cycle.

Figure 4.4 (a) and (c) display the first and second cycle capacity-voltage curves of alkaline cells using EMD and pure ramsdellite as their cathode material. Figure 4.4 (b) and (d) display the inverse derivative of voltage-capacity curves vs. the cell voltage. The sensitive differential peaks (DP) correspond to plateau-like regions in the capacity-voltage profiles. For the reduction of EMD, DPs have been correlated to the reduction of surface layers, ramsdellite tunnels, and pyrolusite tunnels by slow cyclic voltammetry measurements (Figure 4.5) [76], [77], [119].

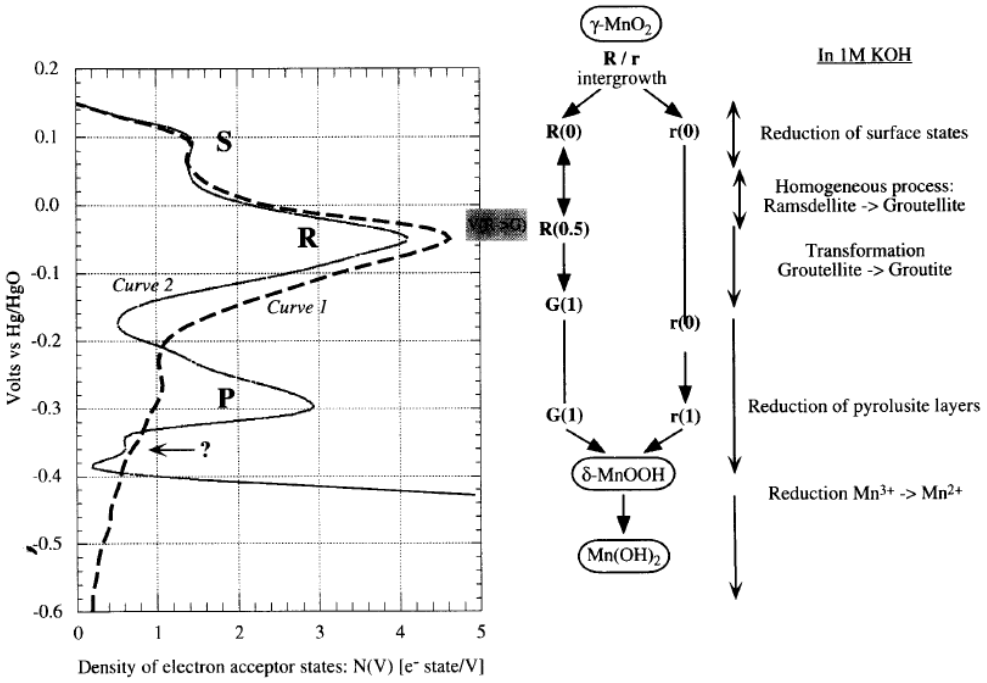

Figure 4.5 Reaction scheme displaying the potentials at which different portions of EMD (e.g., surface manganese (S), ramsdellite domain (R), and pyrolusite domain (P)) are reduced. [74]

The two discharge DPs of EMD on Figure 4.4 (b) can correspond to the reduction of surface MnO_2 and the R-MnO_2 tunnels which occur approximately at 1.4 V_{cell} and 1.22 V_{cell}, respectively. For pure ramsdellite, reduction of MnO_2 on the surface and the tunnels occur approximately at 1.42 V_{cell} and 1.18 V_{cell}, respectively. Moreover, the reduction of the surface and tunnels of pure ramsdellite MnO_2 appear to occur more distinctively in comparison to EMD. This distinction is even visible on the capacity-voltage plots (see Figure 4.4 (a) and (c)) that display a clear inflection point on the discharge curve of the cell using pure ramsdellite at approximately 1.4 V_{cell}. After the first cycle, the reduction of surface MnO_2 of EMD becomes more smeared, however, the reduction of the R-MnO_2 portion of EMD remains quite clear. On the other hand, the reduction of the surface MnO_2 of the pure ramsdellite cell, after repeated cycling remains clear, however, the reduction of the tunnels becomes more smeared after the first discharge. This could be due

to an incomplete reduction of the pure ramsdellite tunnels. Both cells tested are discharged to a DoD of 1.1 V_{cell} where the reduction of the ramsdellite portion of EMD does occur. The lower proton content of pure ramsdellite, and thus the lower protonic conductivity of the material, may introduce a large transport overpotential to the complete reduction of the tunnels. The difference in conductivity can also be observed during the charge cycles. The oxidation of MnOOH to MnO_2 in the R-MnO_2 cells occurs at a potential approximately 25 mV higher in comparison to the EMD-based cells.

Figure 4.6 displays the cycling performance of pure ramsdellite MnO_2 and that of the Erachem EAB-111 EMD sample. The best performing synthesized EMD sample, 2 M H_2SO_4 EMD, is also shown for comparison. The cycling performance of the pure ramsdellite cells is very comparable to the 2 M H_2SO_4 EMD cell in terms of specific capacity after a hundred cycles. However, in terms of capacity fade, the pure ramsdellite-based cells show the best performance. The Erachem EMD and 2 M H_2SO_4 EMD samples lose about 86% and 75% of their initial capacities, respectively, while the ramsdellite-based cells lose only about 50% of its initial capacity after 100 cycles.

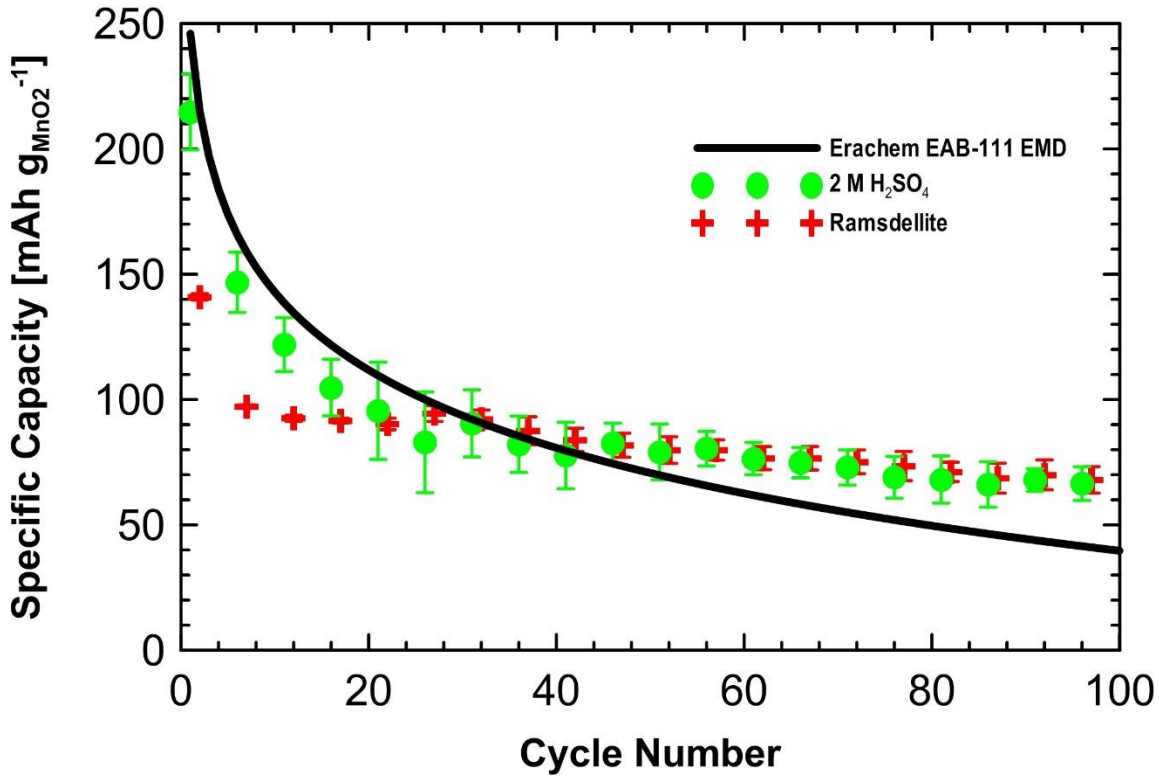

Figure 4.6 Specific capacities for the first 100 cycles of alkaline cells using Erachem EAB-111 EMD, 2 M H_2SO_4 EMD, and pure ramsdellite as the cathode material.

Figure 4.7 shows the energy efficiencies of the ramsdellite and 2 M H_2SO_4 EMD cells. The mid-point voltage (voltage value at the point where 50% of the discharge capacity has been achieved) of each discharge cycle is also shown. Initially, the ramsdellite cells have a lower energy efficiency of about 60%-70% compared to the 2 M H_2SO_4 EMD cells (70%-75%). However, ramsdellite's energy efficiency appears to improve with cycling and reaches a higher value of 80% from the 20^{th} to the 100^{th} cycle. Moreover, the mid-point potential of the ramsdellite cells are initially 75 mV lower than the 2 M H_2SO_4 EMD cells. This metric also improves for the pure ramsdellite cells while it remains constant for the 2 M H_2SO_4 EMD cells. After approximately the 40^{th} cycle, the pure ramsdellite cells' mid-point potential is approximately 50 mV higher than the 2 M H_2SO_4 EMD cells.

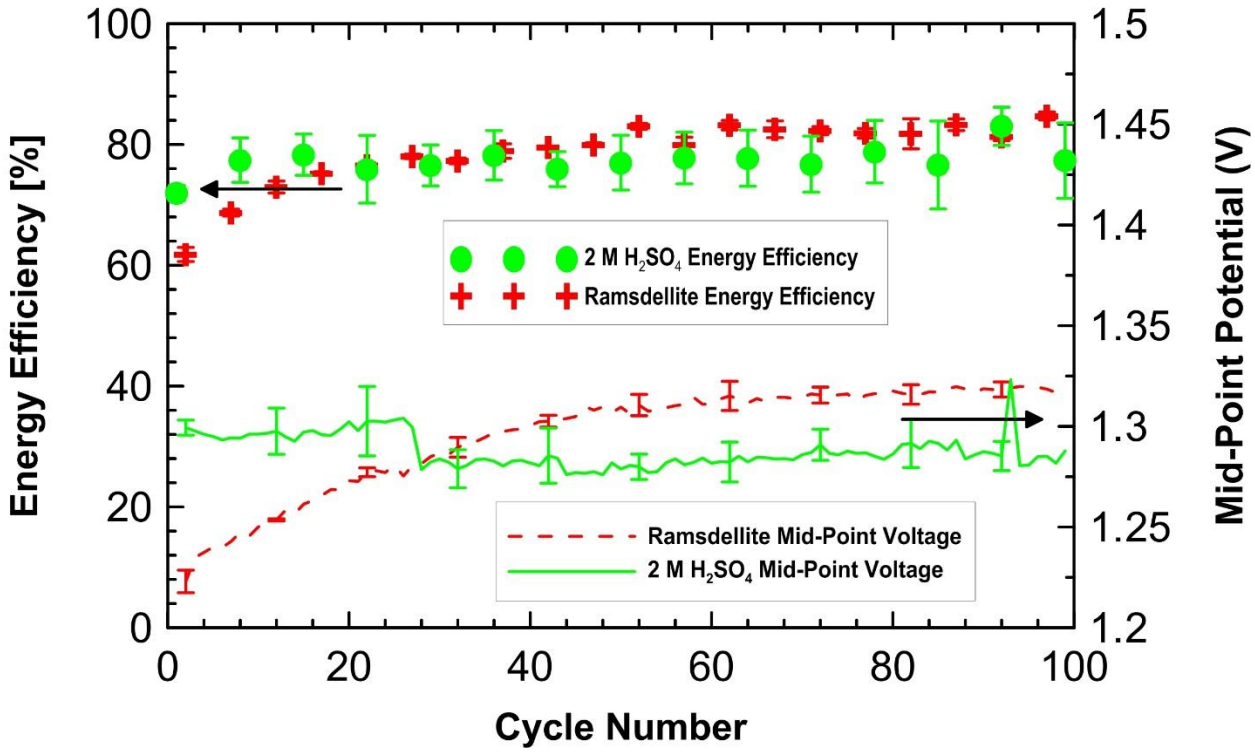

Figure 4.7 Energy efficiency and mid-point potentials for the first 100 cycles of alkaline cells using 2 M H_2SO_4 EMD and ramsdellite as the cathode material.

4.1.2 Post-Mortem Analysis of Ramsdellite MnO_2

Figure 4.8 displays the XRD diffraction patterns of the cathode electrodes of the cells using pure ramsdellite and the best performing EMD sample (2 M H_2SO_4 EMD) after the 100th cycle in a fully charged state. As it can be seen, the ramsdellite goes through a phase transformation towards other phases of MnO_2 (hollandite and/or birnessite MnO_2), hausmannite (Mn_3O_4), and hydrohetaerolite ($ZnMn_2O_4$) like the EMD cathode material. The low capacity of the first electron discharge of hollandite and birnessite phases could further explain the capacity fade of these cells. Additionally, the cycled pure ramsdellite cathode contains fewer unidentified phases (especially at $2\theta \approx 69°$) and the hydrohetaerolite presence appears to be less prominent

(especially at 2θ ≈ 35°) which could explain the improved capacity fade of the pure ramsdellite cells.

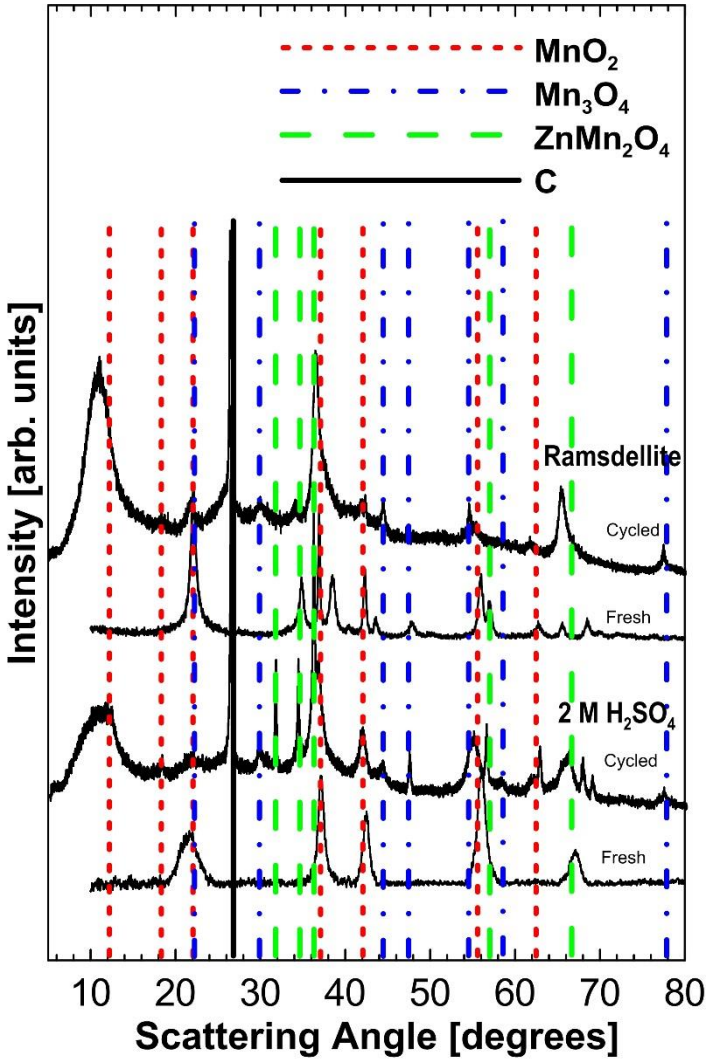

Figure 4.8 XRD profiles of fresh and cycled (100 charge/discharge) MnO_2 samples: ramsdellite and 2 M H_2SO_4 EMD.

4.2 Alternative Electrolyte and Method of Producing Highly Reversible EMD for Rechargeable Alkaline Batteries

At this stage, it is important to note the major differences between cells using KOH-based and $ZnSO_4$-based electrolytes. The MnO_2 cathodes presented so far were cycled using 9 M KOH electrolyte and utilized thick-film electrodes (loading of MnO_2: 60-80 mg cm^{-2}). The MnO_2 cathodes presented in this section were all cycled using 2 M $ZnSO_4$ electrolyte and were produced as thin-film electrodes (loading of MnO_2: 1-5 mg cm^{-2}). Additionally, while the thick-film KOH based cells were cycled from 1.1 V - 1.75 V at a C/10 rate, the thin-film cells were cycled from 0.9 V – 1.85 V at C/2. These changes were done to mimic the parameters used in published researches that have studied $ZnSO_4$ electrolyte [42], [97], [98], [120]–[122]. It is, however, also important to note that previous research in our group by Mehta *et al.* [35] have investigated thin-film electrodes (loading ~ 10 mg cm^{-2}) for KOH-based cells. It was concluded that although thin-film electrodes have a slight improvement in cycling behaviour of EMD in KOH in terms of capacity fade, the specific capacity of EMD drops below 100 mAh g^{-1}_{EMD} after approximately 10 cycles [35]. The same research also concluded that at shallower depths of discharge and higher rates of discharge (using KOH electrolyte) results in a higher capacity fade [35]. Therefore, the comparisons made in this section between cells using the KOH and $ZnSO_4$ are based on the optimized parameters for each electrolyte used.

4.2.1 Electrochemical Behaviour of MnO_2 Cathode in $ZnSO_4$ Electrolyte with $MnSO_4$ Additive

A number of research groups have reported a zinc-ion battery chemistry using MnO_2 (especially the hollandite phase) as the cathode material and $ZnSO_4$ as the electrolyte [42], [97], [98], [120]–

[122]. These groups claim that a $Zn_xMn_2O_4$ type product is produced through zinc intercalation into the MnO_2 tunnels which is reversible to some extent [42], [97], [98], [120]–[122]. However, a recent Nature Energy article by Pan *et al.* debunked zinc intercalation into hollandite by performing transmission electron microscopy analysis on fresh and cycled MnO_2 materials in $ZnSO_4$ electrolyte [42]. Pan *et al.* claim that MnOOH is produced as the discharged product of the MnO_2 cathode like alkaline KOH-based cells [42]. The authors did not observe formation of hausmannite or any other irreversible phases of MnO_2, however, capacity fade was still observed [42]. Pan *et al.* claim that this capacity fade arises from Mn^{3+} ions reducing further to Mn^{2+} during cycling and dissolving into the electrolyte [42]. To address this issue, small amounts of $MnSO_4$ (0.1 M) was dissolved in the $ZnSO_4$ electrolyte in order to prevent this dissolution [42]. Using α-MnO_2 as the cathode material, Pan *et al.* were able to obtain 5,000 cycles at the rate of 5C with 92% capacity retention [42].

To confirm the high rechargeability of α-MnO_2 in 2 M $ZnSO_4$ electrolyte with 0.1 M $MnSO_4$ additive, a cell was made and cycled at a rate of C/2 (see Figure 4.9). A cell using EMD with 2 M $ZnSO_4$ + 0.1 M $MnSO_4$ electrolyte was also made and cycled (Figure 4.9).

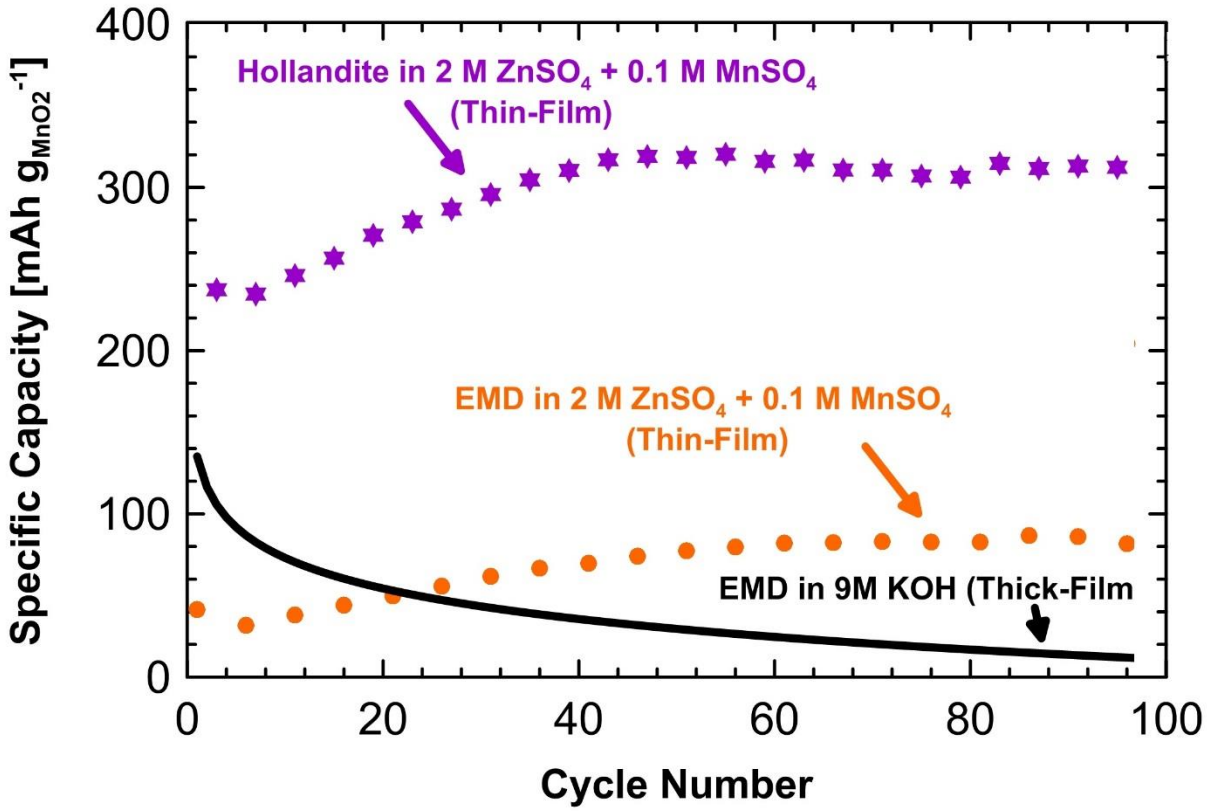

Figure 4.9 Specific capacities for the first 100 cycles of rechargeable thin-film cells in 2 M $ZnSO_4$ + 0.1 M $MnSO_4$ electrolyte using EMD and hollandite as the cathode material.

Figure 4.9 confirms the results stated earlier using α-MnO_2 [42]. It can be seen that EMD has a much lower initial capacity (~ 50 mAh g_{EMD}^{-1}) compared to the α-MnO_2 cell (~ 220 mAh g_{EMD}^{-}) using $ZnSO_4$ electrolyte. However, both cells show an increase in their specific capacity during the first 40 cycles, after which the capacity of both cells reach steady state. Furthermore, the cell using α-MnO_2 as the active material surpasses the theoretical first-electron discharge capacity (308 mAh g_{MnO2}^{-1}) during the initial phase where capacity is increased by approximately 30%. Therefore, it was hypothesized that the added $MnSO_4$ in the electrolyte would lead to a deposition of additional MnO_2 on the cathode electrode during the charging steps.

4.2.2 Synthesis of Electrolytic Manganese Dioxide in Mild Electrolyte

To test this hypothesis, cyclic voltammetry (CV) experiments were carried using carbon paper as the working electrode and zinc as the counter electrode inside saturated $ZnSO_4$ electrolytes with and without the $MnSO_4$ additive (see Figure 4.10).

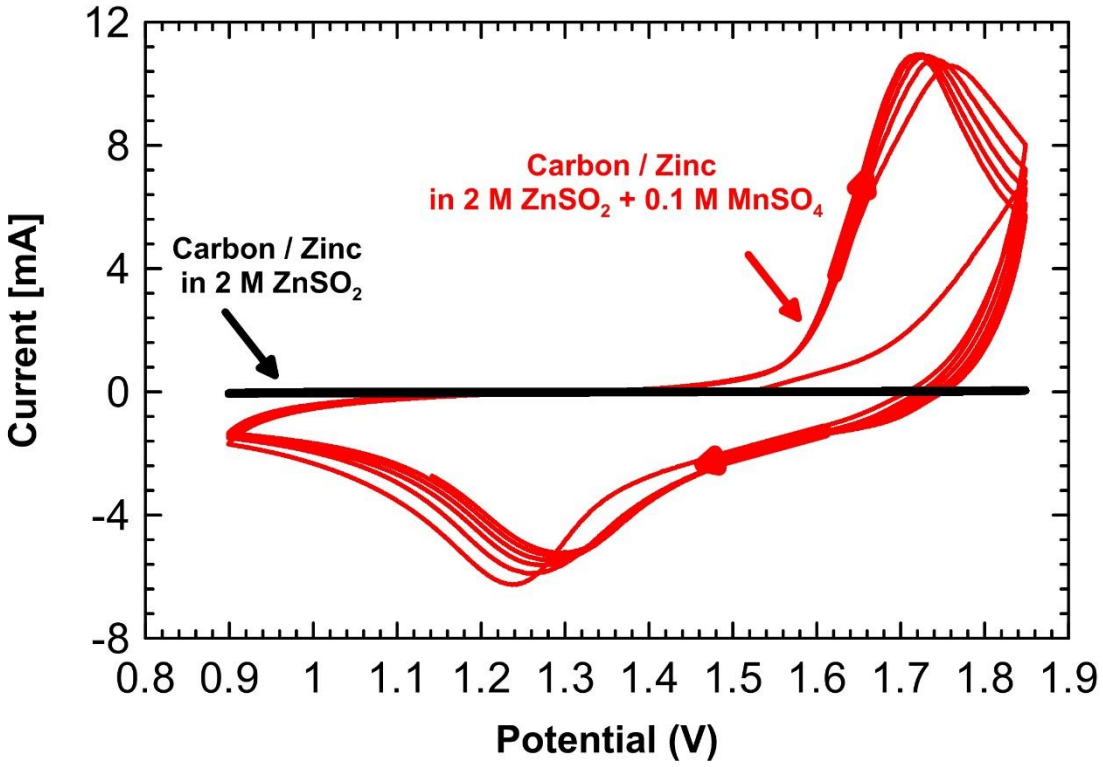

Figure 4.10 CV of carbon paper as working electrode and zinc as counter electrode in a 2 M $ZnSO_4$ electrolyte with and without 0.1 M $MnSO_4$ as additive.

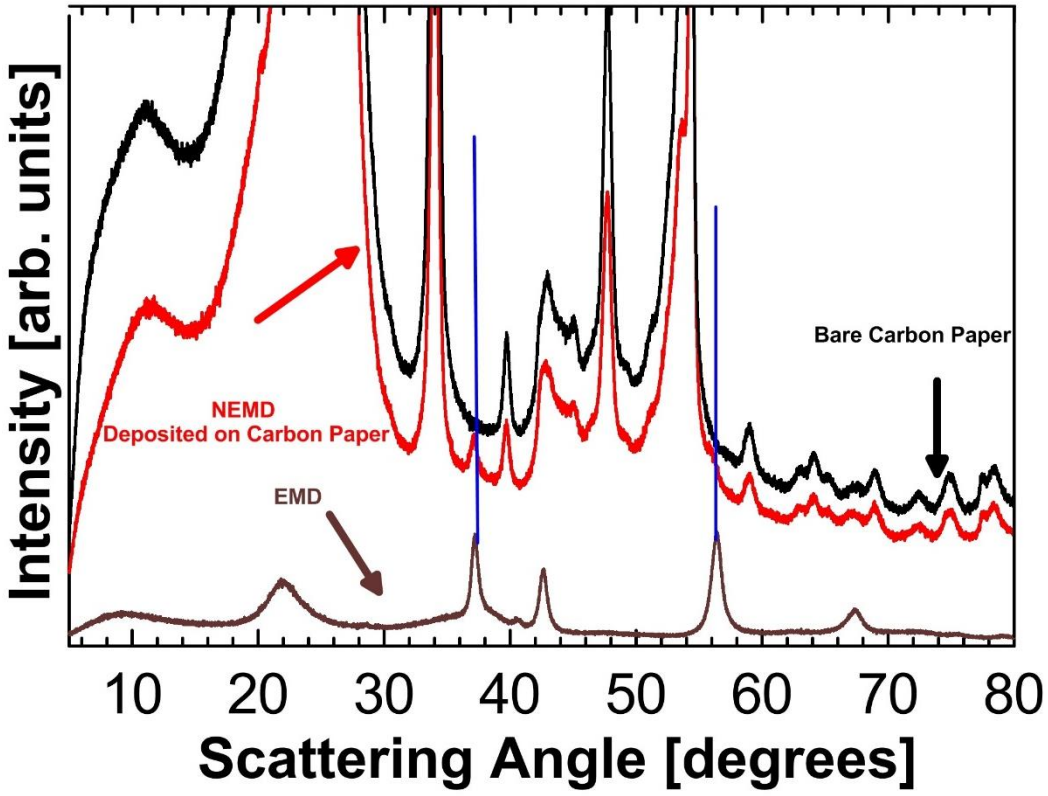

Figure 4.11 XRD pattern of NEMD deposited on carbon paper as compared to the XRD pattern of the bare carbon and Erachem EMD.

Figure 4.10 reveals that no electrochemical activity occurs when a carbon electrode is cycled against zinc electrode in a $ZnSO_4$ solution. However, when $MnSO_4$ is added to the electrolyte, an oxidation occurs (possibly MnO_2 deposition) while the potential is raised. Furthermore, XRD of the carbon paper displays the presence of some prominent EMD peaks (see Figure 4.11). It is important to note that due to the dominance of carbon paper's XRD peaks, the full NEMD spectrum is not fully revealed. Based on these findings and the peaks of the CV figure above, the following reactions are proposed for the electrolytic deposition of MnO_2 in a 2 M $ZnSO_4$ electrolyte with added $MnSO_4$ (see Equations 4.1-4.3).

$$ZnOH^+ + H^+ + 2e^- \rightarrow Zn + H_2O \qquad E_{Red} = -0.497\ V_{SHE} \qquad \textbf{Equation 4.1}$$

$$Mn^{2+} + 2H_2O \rightarrow MnO_2 + 4H^+ + 2e^- \qquad E_{Ox} = -1.224\ V_{SHE} \qquad \textbf{Equation 4.2}$$

$$ZnOH^+ + Mn^{2+} + 2H_2O \rightarrow MnO_2 + Zn + 3H^+ \qquad E_{Cell} = -1.721\ V_{cell} \qquad \textbf{Equation 4.3}$$

Since this deposition occurs inside a milder environment (more neutral (pH ~ 3) than EMD synthesized in H_2SO_4 (pH~0)), this type of MnO_2 has been named Neutral Electrolytic Manganese Dioxide (NEMD). Furthermore, in-situ NEMD is given as the shorthand name for the MnO_2 that develops inside a cell as a result of added $MnSO_4$ to the electrolyte, as was the case in cells shown in Figure 4.9.

Synthesis of NEMD was also attempted inside an electrolysis cell using nickel foil as the anode and zinc foil as the cathode. This method allowed for the NEMD powder to be collected for further analysis. During this reaction, MnO_2 was deposited on the nickel anode as expected. This MnO_2 product is given the shorthand name ex-situ NEMD because it has been synthesized outside of the battery cell hardware. Figure 4.12 (a) displays the XRD patterns of ex-situ NEMD and Erachem EMD. In terms of phase structure, both EMD and NEMD are very similar except for the lack of a EMD peaks which are indicated in the figure. Additionally, the nickel electrode dissolves to some extent during NEMD deposition, therefore, nickel metal peaks are also observed in the ex-situ NEMD.

Furthermore, deposits were also observed on the zinc cathode during NEMD electrolysis. To confirm the reaction on the zinc cathode, as hypothesized in Equations 4.2, XRD was also performed on this electrode (see Figure 4.12 (b)). Zinc metal was observed in the XRD pattern;

however, additional minor peaks were also present. These peaks can be correlated to an electrodeposited nickel/zinc alloy [123], which could have occurred as a side reaction due to the dissolved nickel.

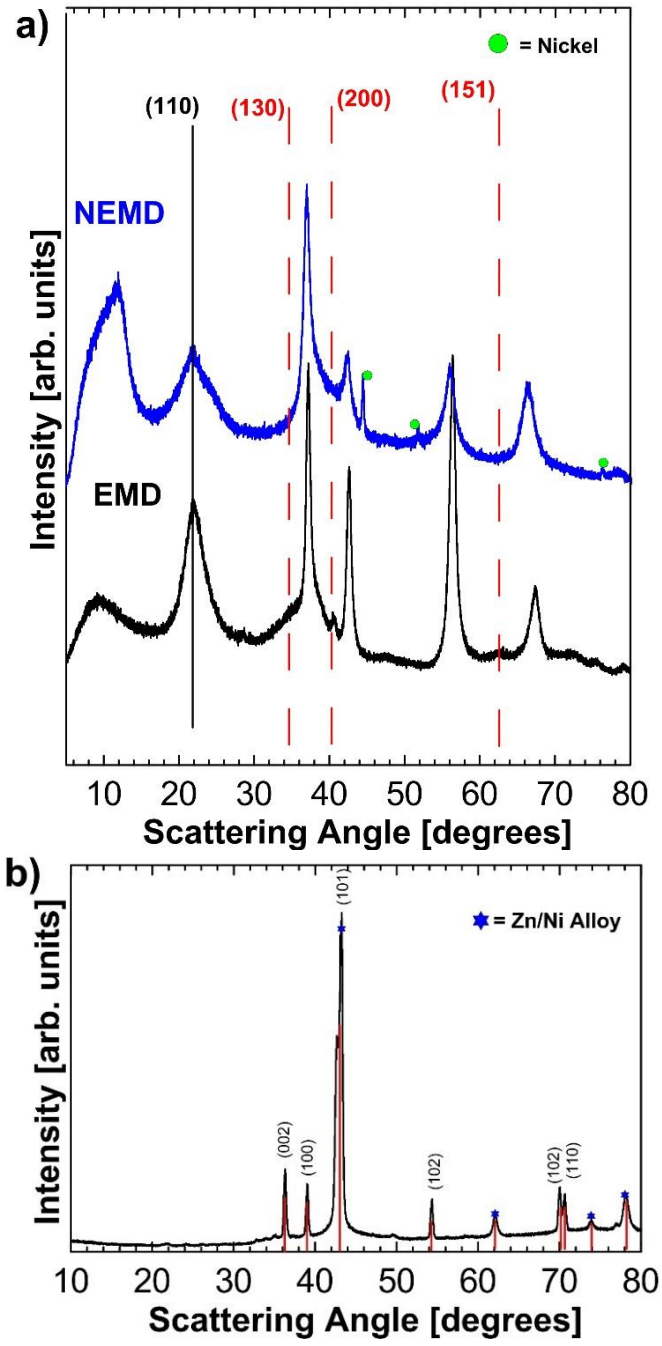

Figure 4.12 a) XRD patterns of Erachem EAB-111 EMD and ex-situ NEMD; b) XRD pattern of zinc cathode after deposition.

Table 4.1 compares some physical and electrochemical characteristics of ex-situ NEMD and EMD. Compared to EMD, ex-situ NEMD performs significantly better in $ZnSO_4$ electrolyte compared to EMD. However, NEMD also has a very low initial capacity KOH electrolyte compared to EMD despite its high surface area and water content. Although, it terms of capacity retention and specific capacity after 100 cycles, NEMD outperforms conventional EMD at high cycling rate (C/2) and is very comparable to the best EMD sample at slower cycling rate (C/10) (see Table 4.1).

Table 4.1 Physical characterization of ex-situ NEMD vs. acidic EMD samples tested in this thesis.

	ex-situ NEMD	EMD
Electrolyte Composition for Electrolysis	1 M $MnSO_4$ 2 M $ZnSO_4$ (pH~3)	1 M $MnSO_4$ 0.5-5 M H_2SO_4 (pH~0)
BET Surface Area ($m^2\ g^{-1}$)	230	40-90
Structural Water Content (%)	4.4	2.5-4.5
XRF Elemental Analysis	95% Mn 2.5% Ni 2.5% Zn	≥ 99.8% Mn
Initial and Final Capacity in $ZnSO_4$ Electrolyte at Rate of C/2 (mAh g^{-1}_{MnO2})	1st Cycle: 150 100th Cycle: 105	1st Cycle: 20-60 100th Cycle:20-60
Initial and Final Capacity in KOH Electrolyte at Rate of C/2 (mAh g^{-1}_{MnO2})	1st Cycle: 100 100th Cycle: 50	1st Cycle: 135 100th Cycle: 10
Initial and Final Capacity in KOH Electrolyte at Rate of C/10 (mAh g^{-1}_{MnO2})	1st Cycle: 100 100th Cycle: 60	1st Cycle: 250 100th Cycle: 40-70

The ex-situ NEMD powder was tested inside a battery cell using 2 M $ZnSO_4$ electrolyte without $MnSO_4$ additive in order to avoid additional deposition of in-situ NEMD. Figure 4.13 (a) shows the cycling performance of the ex-situ NEMD in 2 M $ZnSO_4$ electrolyte. Ex-situ NEMD has an initial capacity of approximately 150 mAh g_{NEMD}^{-1} which is lower than the initial capacity of EMD cycled

in KOH. However, NEMD cycled in $ZnSO_4$ shows a capacity fade rate of 0.5 mAh $cycle^{-1}$ and therefore it has a specific capacity above 100 mAh g^{-1} at the 100th cycle which satisfies the industrial objectives set out in this thesis.

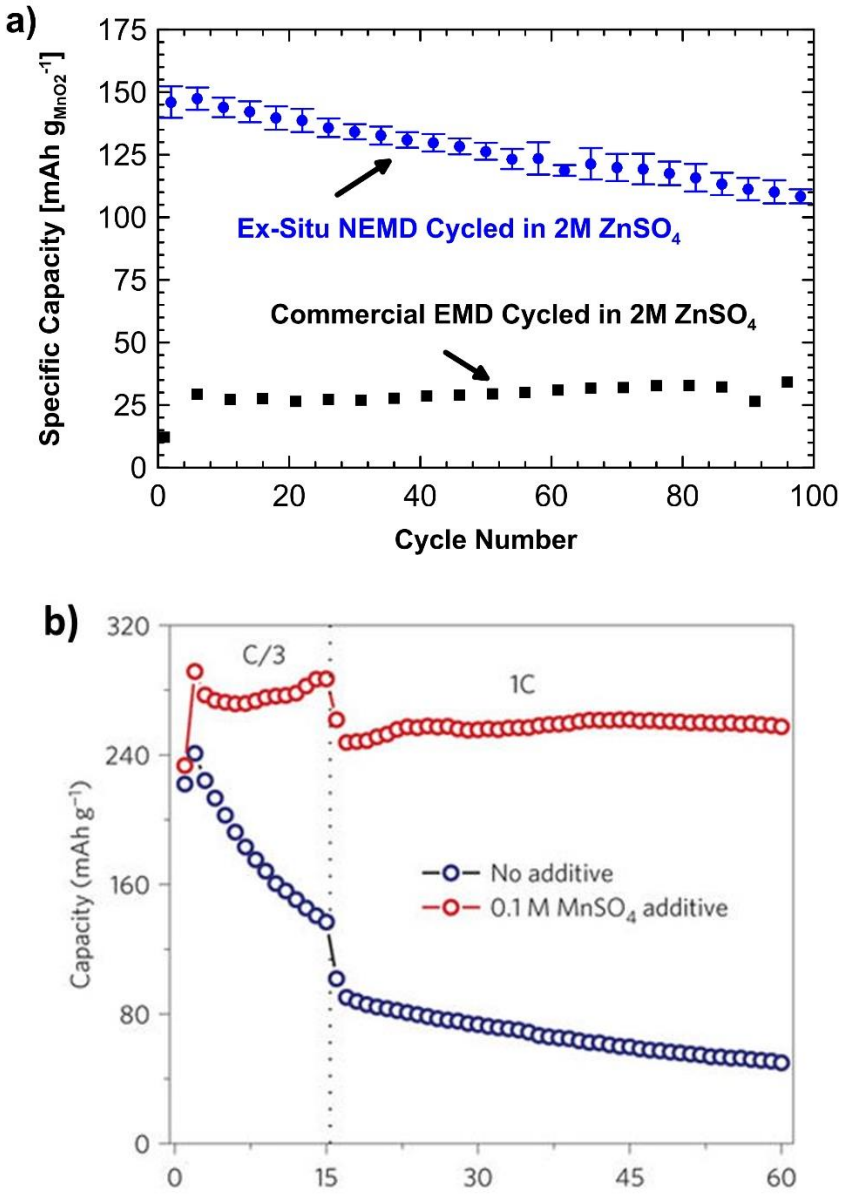

Figure 4.13 a) A comparison of cycling performance of ex-situ NEMD in 2 M $ZnSO_4$ electrolyte and EMD cycled in 9 M KOH at the rate of C/2. b) The cycling performance of α-MnO_2 cycled in 2 M $ZnSO_4$ with and without 0.1 M $MnSO_4$ additive at rates of C/3 and 1C as performed by Pan et al. [42]

The performance of ex-situ NEMD appears to also be similar, if not better, than the performance of α-MnO_2 cycled in 2 M $ZnSO_4$ without 0.1 M $MnSO_4$ additive as reported by Pan *et al.* [42] which show a capacity fade rate of 7 mAh $cycle^{-1}$ at a C/3 rate during the first 15 cycles (see Figure 4.13 (b)). However, α-MnO_2 does have a higher specific capacity than NEMD. Potential benefit of ex-situ NEMD over hollandite is the ease of synthesizing ex-situ NEMD using already established EMD synthesis methods rather than the hydrothermal method that must be used for hollandite. Furthermore, NEMD is synthesized at room temperature and under milder conditions, making it easier than EMD synthesis. However, it should also be noted that the current method used in this thesis for synthesizing NEMD is only approximately 20% efficient and thus more research must be done to improve efficiency and limit electrode dissolution.

Battery cells were also assembled using a piece of bare carbon paper as the cathode and 2M $ZnSO_4$ with $MnSO_4$ added to the electrolyte to observe how well the in-situ NEMD cycles without any readily available active material (MnO_2). Figure 4.14 displays how the capacity of such cells grow as minute amounts of NEMD is deposited during each charge cycle. These cells were charged and discharged at a current density of 0.1 mA cm^{-2} and held at 1.85 V for three hours at the end of each charge step. During each cycle, some MnO_2 was deposited during the charge step, which was discharged during the next cycle. To calculate the specific capacity for these cells, it was assumed that all the charge capacity in the first cycle and any excess charge capacity after that is used to deposit the in-situ NEMD. Figure 4.15 displays the cycling performance as well as the approximated loading of MnO_2 during cycling. As observed, the specific capacity of in-situ NEMD reaches approximately 120 mAh g_{NEMD}^{-1} after 100 cycles which is 10% higher the ex-situ

NEMD's capacity of approximately 105 mAh g_{NEMD}^{-1}. Furthermore, a specific capacity of 90 mAh g_{NEMD}^{-1} is maintained after 180 cycles. However, the loading of these cell can only reach a maximum of approximately 1 mg cm^{-2} (areal capacity ~ 0.1 mAh cm^{-2}) after 180 cycles. In comparison, cells using ex-situ NEMD can have a loading of up to 5 mg cm^{-2} (areal capacity ~ 0.5 mAh cm^{-2}) from the initial cycle.

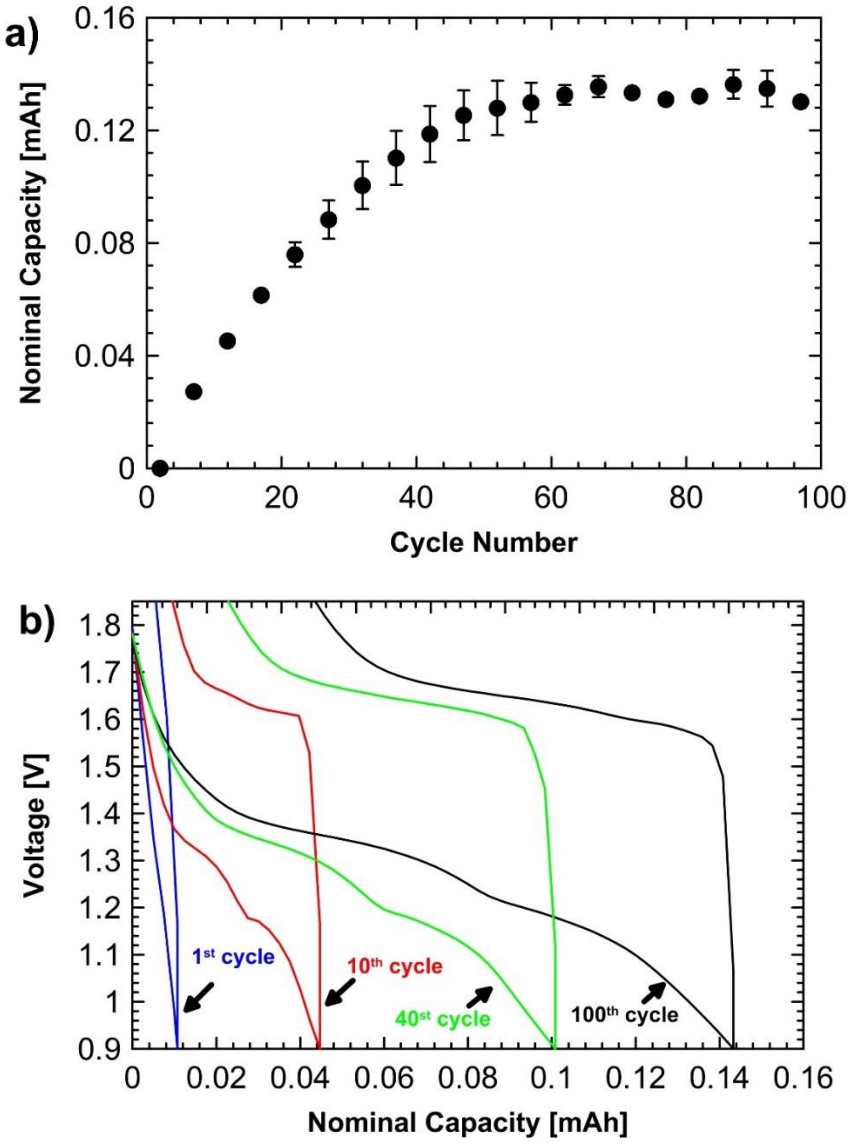

Figure 4.14 (a) Total capacity growth of in-situ NEMD cell and (b) total capacity vs. voltage curves at different stages of capacity growth.

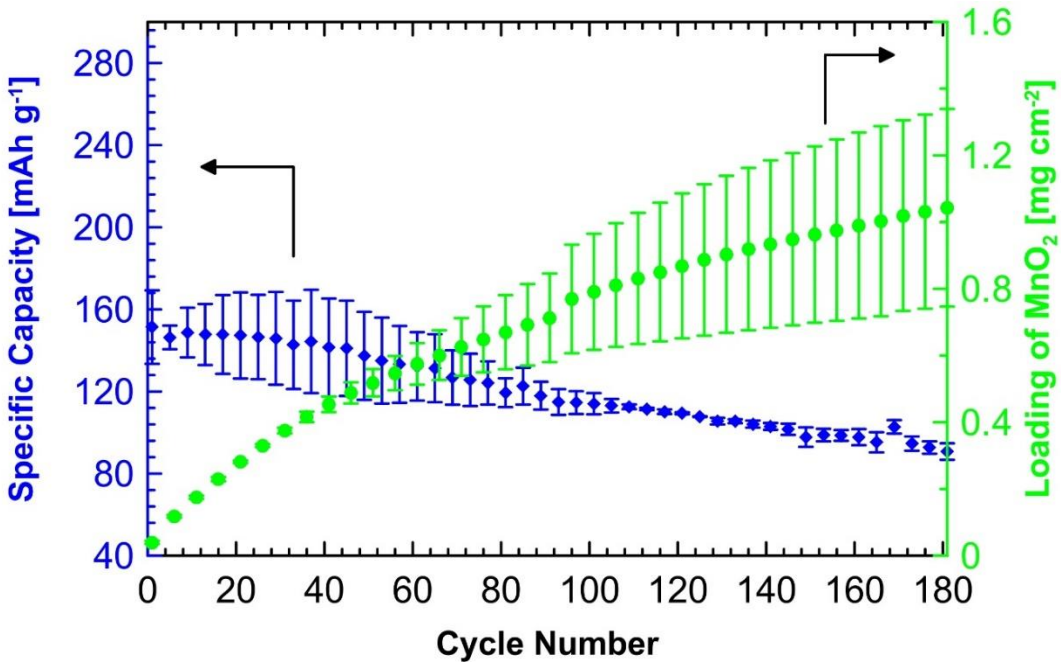

Figure 4.15 Cycling performance and loading of in-situ NEMD in $ZnSO_4$ electrolyte.

The in-situ NEMD cells shown in Figure 4.15 was cycled using the protocol shown in Figure 4.16 (a) where the potential is held at 1.85 V_{cell} to complete the charge process, i.e. similar to the cycling of the ex-situ NEMD. During this step, the current decays rapidly. However, to increase the loading and areal capacity quickly, in-situ NEMD cells were made without a cut-off charge voltage (see Figure 4.16 (b)). These cells were charged galvanostatically for a fixed amount of time without the limitations of upper voltage cut-off for the charge step.

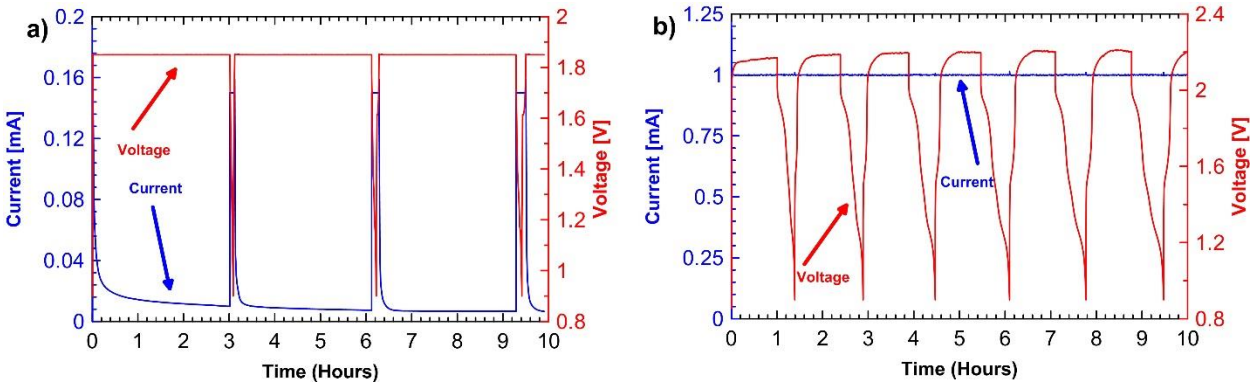

Figure 4.16 a) Cycling regime of in-situ NEMD cells with a charge cut-off voltage and b) cycling regime of in-situ NEMD cells with a charge time limitation.

This time-based cycling regime for in-situ NEMD results in an areal capacity of 0.8 mAh cm^{-2} and NEMD loading of 8 mg cm^{-2} after just 10 cycles (see Figure 4.17). This mode of cycling method can further lead to a mid-point cell voltage to 1.5 V_{cell} which is about 30 mV higher than the previous method of making in-situ NEMD cells (see Figure 4.18). These parameters can also be further enhanced by using a current collector with more active sites or saturating the $MnSO_4$ content in the electrolyte. These improvements will lead to an increase in the volumetric energy density of $ZnSO_4$-based, thus making such cells a great option for commercially viable rechargeable MnO_2/Zn batteries.

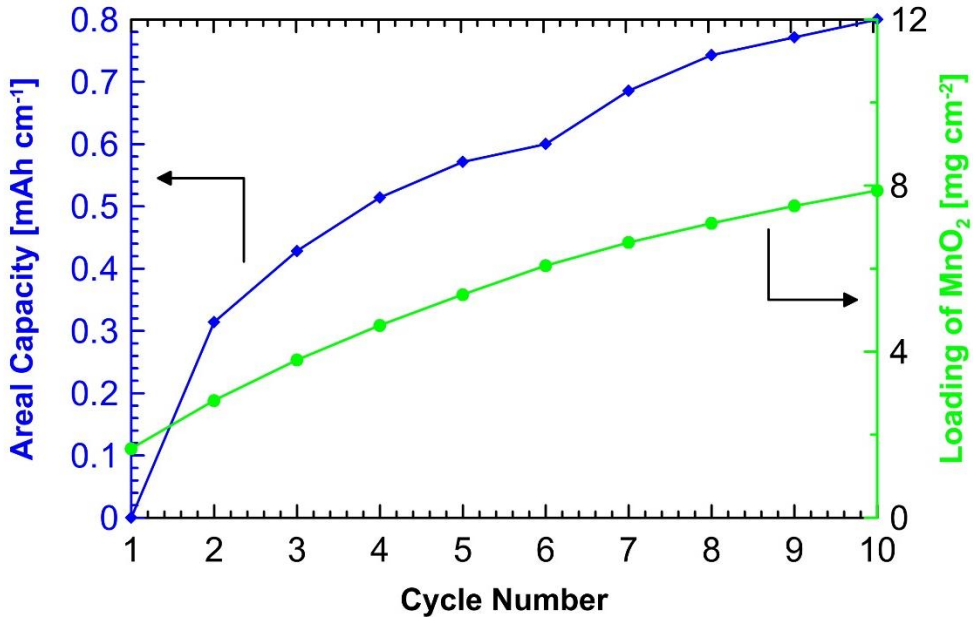

Figure 4.17 Areal capacity and loading of in-situ NEMD cell using a cycling regime with a charge time limitation.

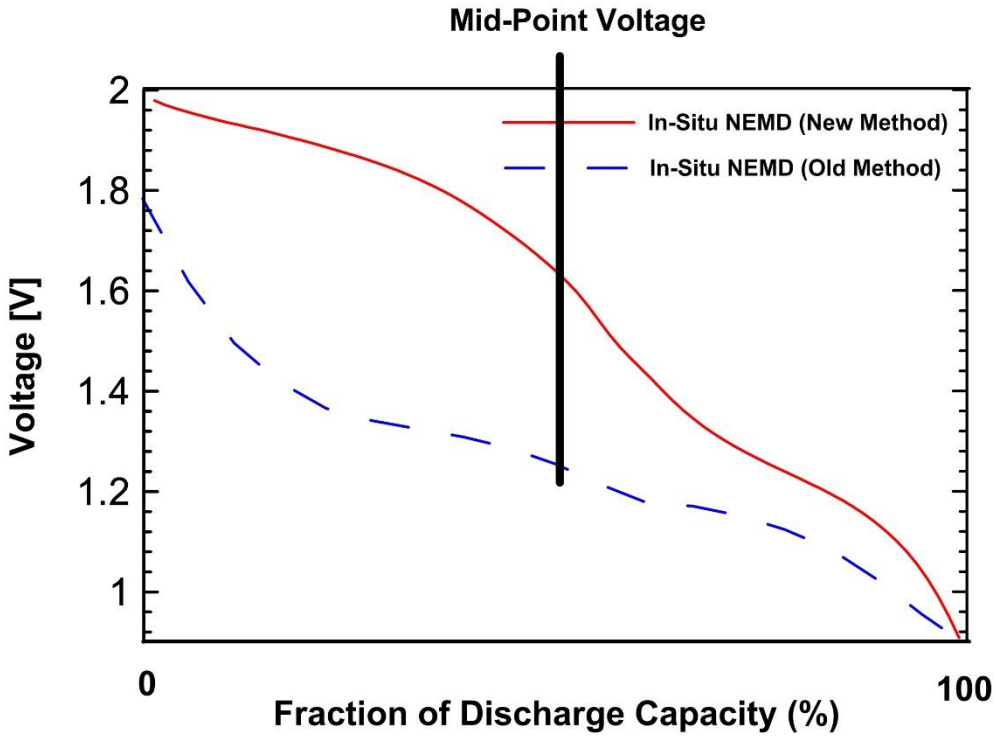

Figure 4.18 Comparison of mid-point discharge voltages of in-situ NEMD cells with a charge cut-off voltage (Old Method) and with a charge time limitation (New Method).

4.2 Summary of the Results and Discussion

This thesis investigated various samples and phases of MnO_2, synthesized both electrochemically and chemically, and different electrolyte solutions used for cycling of the cell to build a rechargeable MnO_2/Zn cell with at least 100 mAh g_{MnO2}^{-1} of specific capacity after 100 cycles.

Initially, MnO_2/Zn cells using a strong basic electrolyte (9 M KOH – pH ~ 14) was used for investigating various electrodeposited MnO_2 samples synthesized in a highly acidic H_2SO_4-based (0.5-5 M KOH – pH ~ 0) solutions. It was concluded that EMD synthesized inside a 2 M H_2SO_4 electrolyte produces a sample with structural water and ramsdellite content that can hold a specific capacity of 70 mAh g_{MnO2}^{-1} in comparison to commercially produced EMD (Erachem EAB-111) that has a capacity of 40 mAh g_{MnO2}^{-1} after 100 cycles. Furthermore, chemically produced ramsdellite MnO_2 was also investigated as the active cathode material. Pure ramsdellite had a low initial specific capacity possibly due to its low structural water content; however, it could retain a capacity of 70 mAh g_{MnO2}^{-1} similar to 2 M H_2SO_4 cell.

Mild electrolyte (2 M $ZnSO_4$ – pH ~ 4) was also used for investigating various MnO_2 samples. All MnO_2 samples displayed high capacity retention in this electrolyte. However, conventional EMD samples displayed a very low capacity (50 mAh g_{MnO2}^{-1}) utilization compared chemically produced hollandite MnO_2 (250 mAh g_{MnO2}^{-1}). Electrodeposited MnO_2 samples with high capacity utilization was also synthesized inside mild environments (2 M $ZnSO_4$ + 1 M $MnSO_4$ – pH ~ 4) after it was discovered that added $MnSO_4$ to the $ZnSO_4$-based MnO_2/Zn cells lead to the electrodeposition of additional high capacity MnO_2 inside the cell during cycling. This finding was contrary to the many

of the researches in literature than claim added $MnSO_4$ to the $ZnSO_4$-based MnO_2/Zn cells improve cycling by preventing dissolution of the MnO_2 cathode. MnO_2 powder synthesized in $ZnSO_4$ electrolyte inside an electrolysis cell was named ex-situ NEMD and MnO_2 deposited directly inside the $ZnSO_4$-based cell, as a result of added $MnSO_4$, was named in-situ NEMD. Ex-situ NEMD displayed an initial specific initial capacity of 150 mAh g_{MnO2}^{-1} when cycled in 2 M $ZnSO_4$ electrolyte and a final capacity of 105 mAh g_{MnO2}^{-1} after 100 cycles. The cycling performance of in-situ NEMD was also investigated by making cells without any MnO_2 on the cathode. In-situ NEMD had a similar initial specific capacity to ex-situ NEMD, however, it maintained a higher final capacity of 120 mAh g_{MnO2}^{-1} after 100 cycles. Furthermore, it was displayed that in-situ NEMD cells with a loading of MnO_2 comparable to what is used in literature (1-5 mg cm^{-2}) can be produced, which shows great potential for making highly rechargeable MnO_2/Zn cells that can be produced in a single step.

Chapter 5. Conclusion and Recommendations for Future Work

5.1 Conclusion

5.1.1 Impact of Electrodeposition Conditions on the Physical Properties of EMD

A thorough study of EMD synthesis by electrolysis of 1 M $MnSO_4$ in various H_2SO_4 concentration (0.5 M to 5 M) at various current densities (0.0075 A cm^{-2} to 0.0175 A cm^{-2}) on titanium anode was performed. These experiments were performed at a constant temperature of 95 ^oC in order to decrease the overpotential of the electrolysis cell. The impact of growth conditions on the EMD structure, ramsdellite content, structural water content, surface area, and porosity of the samples were studied in detail. The results were compared to a typical commercial EMD product (Erachem EAB-111). The key findings can be summarized as below:

- The highest ramsdellite content (86%), structural water content (4.4%), and BET surface area (86 m^2 g_{EMD}^{-1}) of the pure EMD phases synthesized was achieved when electrodeposition of EMD was performed in a 2 M H_2SO_4 bath.
    - In comparison, the commercial EMD (Erachem EAB-111) tested had a ramsdellite content of 59%, structural water content of 2.6 wt%, and BET surface area of 42 m^2 g_{EMD}^{-1}.
- The 2 M H_2SO_4 EMD had a smaller pore size (~2.7 nm) compared to other EMD samples synthesized or the commercial sample (~4.9 nm), leading to a higher BET surface area.

- Increasing the acid concentration beyond 2 M H_2SO_4 led to mixtures of EMD and other types of manganese oxide phases.
- Varying the current density of the EMD electrolysis at the optimum acid concentration had little to no effect on the physical characteristics of produced EMD.
- Higher acid concentrations (> 2 M H_2SO_4) and current densities (> 0.0125 A cm^{-2}) decreased the current efficiency of EMD synthesis and furthermore led to destruction of the titanium anode during the electrodeposition.

5.1.2 Impact of Mild Electrolyte Conditions on the Physical Properties of EMD

Electrodeposited MnO_2 was also achieved under much milder conditions (pH ~ 3) using 0.6 M $MnSO_4$ + 2 M $ZnSO_4$ and a nickel anode (at ambient pressure and room temperature). The electrodeposition process was performed either potentiostatically with a cell voltage of 2.5 V_{cell}. The product obtained was named “neutral” EMD or NEMD. NEMD’s structure was found to be very similar to that of acidic EMD. It also had a structural water content of 4.4 wt%, and a very high surface area of 230 m^2 g^{-1}. The electrolysis process, however, had a very low current efficiency of approximately 20% and the nickel anode severely corroded during the electrolysis process.

5.1.3 Electrochemical Behaviour of Various MnO_2 Phases in KOH or $ZnSO_4$ Electrolytes

A thorough study of the electrochemical behavior of various MnO_2 products, synthesized chemically or electrochemically, in KOH electrolyte as thick-film electrodes, was performed. Full-cell experiments using a zinc anode were performed with all MnO_2 products and half-cell

experiments using a Hg/HgO reference electrode, were performed on selected samples. The impact of the MnO_2 phase and/or physical characteristics on cycling behavior and performance, energy delivery and efficiency, and impedance was studied. Physical characterization of cycled MnO_2 cathodes was also performed to investigate the reason for cell failure. The following outlines the key findings:

- Compared to all the EMD samples (with the exception of NEMD) tested and synthesized, the 2 M H_2SO_4 EMD had the highest energy efficiency and best cycling performance over 100 discharge/charge cycles.
    - 2 M H_2SO_4 EMD had a 30% higher energy efficiency over the cycling period and 35% higher capacity at the end of the cycling period in comparison to the commercial EMD sample.
    - 2 M H_2SO_4 EMD had a slightly higher bulk resistance in comparison to the commercial EMD most likely due to its smaller pore size, however, it showed a lower charge transfer resistance due to its higher structural water content.
- Chemically synthesized ramsdellite MnO_2 had about 300% higher initial capacity in comparison to other chemically synthesized MnO_2 phases tested (birnessite and hollandite) when discharged to 1.1 V_{cell}, however, it had 40% less initial capacity compared to any other pure phase EMD sample.
    - The pure ramsdellite phase of MnO_2 had the best cycling performance compared to other MnO_2 phases tested.

    - After 100 cycles, the ramsdellite phase of MnO_2 showed the same final specific capacity as the 2 M H_2SO_4 EMD.
    - In comparison to the 2 M H_2SO_4 EMD, the pure ramsdellite phase MnO_2 also showed an improved energy delivery and efficiency during the cycling period (100 cycles).
- Thermogravimetric analysis of cycled EMD samples showed significant loss of structural water (20 wt% to 50 wt%) for all samples.
- X-ray diffraction of cycled EMD and ramsdellite MnO_2 showed the formation of lower capacity MnO_2 phases (birnessite and hollandite) and irreversible manganese oxide phases (hausmannite and hydrohetaerolite) for all samples.

A preliminary study of the electrochemical behavior of EMD and NEMD products in $ZnSO_4$ electrolyte, as thin-film electrodes, was also performed. Full-cell experiments, using zinc anodes were performed. NEMD had an initial capacity of 160 mAh g_{NEMD}^{-2}, which is 400% higher than EMD. NEMD was shown to hold a capacity of about 120 mAh g_{NEMD}^{-2} after 100 cycles at a C/2 rate compared to 40 mAh g_{EMD}^{-2} for conventional EMD.

5.1.4 In-Situ MnO_2-Zn Cell

In this thesis, a novel type of MnO_2/Zn cell was developed, which is composed of an active carbon cathode, zinc metal anode, and an electrolyte solution consisting of 2 M $ZnSO_4$ with added $MnSO_4$ salt. The assembled cell starts at a discharged state, but with progressive cycling, highly rechargeable EMD gradually grows on the carbon cathode. Such a cell has a specific capacity of

approximately 120 mAh g_{MnO2}^{-2}, and displays promising results for high rechargeability in the long term.

5.2 Recommendations for Future Work

Bismuth oxide (Bi_2O_3) additives in the cathode of KOH-based cells have been shown in literature to allow a reversible cycling of the second electron discharge of MnO_2 and improved rechargeability. Addition of bismuth oxide, reportedly, prevents the formation of irreversible manganese oxide phases and leads to formation of a bismuth-doped birnessite MnO_2 phase during the charge step [124]–[129]. This additive has gained renewed interest as there have been some recent studies on the use of metal ions, i.e., copper, lithium, etc., in combinations of a bismuth oxide additive to further stabilize the charged state of the MnO_2 cathode [117], [121]. These reports claim that the metal ions (i.e., Cu, Li, etc.) further stabilize the birnessite MnO_2 phase that forms during the charge step by intercalating in-between the birnessite layers [117], [121]. Despite the very high capacity of these cells (up to 600 mAh g_{MnO2}^{-1} for two electron discharge), the cell energy still requires further improvement. The cells with added bismuth and metal intercalants (e.g., copper) are discharged at an approximately average potential of 0.9 V_{cell}, which is 0.5 V lower than the theoretical potential of the full first electron discharge of MnO_2 (1.4 V_{cell}). In a previous study by Mehta *et al.*, the effect of bismuth additive was investigated in cells with a higher cut-off potential during discharge (1.1 V_{cell}), and it was shown to have very little effect during this high potential cycling regime [35]. If the results of these recent cited papers are confirmed, a significant improvement in the rechargeability of the MnO_2-Zn cells with KOH electrolyte has been made. Therefore, it is important to mention that in pursuit of a highly

rechargeable MnO_2-Zn batteries, utilization of commercial EMD with Bi_2O_3 and metal ion additives are important to investigate. For future work on this topic, it is recommended to investigate other metal ions that can act as intercalants (e.g. Ni, Co, V) and its effect on the cell potential. It would also be very interesting to see if other metal oxides other than manganese (e.g. TiO_2, FeO, V_2O_5, etc.) can be used as the cathode material to further improve cell energy.

5.2.1 Improving EMD Electrolysis Study

Although a thorough systematic approach was taken to study the effect of electrolysis parameters (acid concentration and current density), further improvement could be made. For example, the $MnSO_4$ concentration was held constant throughout the study while the acid concentration was varied. This meant that in order to vary the pH of electrolysis, careful measures were not taken to keep the conductivity of the electrolyte constant by varying the salt concentration. Furthermore, the effect of varying salt concentration on the electrolysis was not studied. Therefore, for future studies, the aforementioned factors should be considered. Furthermore, the following studies can be done to further improve the physical and electrochemical characteristics of EMD:

- Utilization of dopant metals (Ti, Co, Ni, etc.) or electrolysis electrolyte additives (surfactants) to synthesize a more stable EMD phase and improve its surface area and morphology.
- Carrying out the electrolysis in the presence of ultrasonic field to alter the deposition mode in an attempt to further enhance EMD's characteristics.

5.2.2 Further Analysis on KOH-Based Cells

One problem with RAM cells is its low power output. To study how this factor could be improved, the following study is recommended:

- Study the effect of MnO_2 (EMD and other phases) loading on it the cycling performance of the cathode at varying c-rate.
    - This could be done to improve the rate capability of the MnO_2 cathode.

The MnO_2's lattice expands and contracts during cycling due to proton insertion and deinsertion. This is one factor that could lead to capacity fade in RAM cells. Therefore, it is recommended to carry out an investigation on various MnO_2 phases and EMD samples to find any correlation between capacity fade and lattice size change and whether there is a relationship between various properties of MnO_2 (tunnel size, d-spacing, lattice size, etc.) and the extent of expansion/contraction.

5.2.3 Improving In-Situ MnO_2-Zn Cells

A number of further improvements for the in-situ MnO_2-Zn cells and NEMD synthesis are suggested here. At present the in-situ electrodes have a very low areal capacity of ~0.1-1 mAh cm^{-2} because of the very low MnO_2 loadings (~1-10 mg cm^{-2}). The regular EMD-based electrodes tested have a loading of up to 65 mg cm^{-2} and an areal capacity of up to 10 mAh cm^{-2}. Therefore, for future work on improving in-situ MnO_2-Zn cells, the following suggestions are made:

- Performing further characterization on the in-situ cells to understand the exact structural phases of MnO_2 deposited, and the phases that form during the cycling period.
    - This could be done by performing XRD (or Raman spectroscopy, etc.) at different potentials or performing measurements while the cell is cycling.
- The use of high surface area, highly activated carbon, or other porous, materials for the cathode current collector to increase the MnO_2 deposition.
    - It is worth mentioning that preliminary results of addition of small amounts of carbon black powder (in the form of ink) on the carbon paper current collectors displays both increased specific capacity and hence areal capacity.
- Investigating varying amount of $MnSO_4$ salt in the electrolyte solution and its effect on the amount of deposited MnO_2 and/or capacity retention.
    - Early preliminary results on saturating the 2 M $ZnSO_4$ electrolyte with $MnSO_4$ salts has shown an inhibition of MnO_2 deposition, however, an optimal concentration could be determined in the range of 0.1 M $MnSO_4$ and the saturation point (~ 2.5 M).
- Studying the effect of temperature on the kinetics of formation during the cycling period when MnO_2 deposition occurs.

5.2.4 Improving NEMD Synthesis

An important challenge with the synthesis of NEMD is the very low Faradic efficiency of the process (~20%) and the complete destruction of the nickel anode where the NEMD deposition takes place. The reason is that nickel corrodes at a much lower potential in comparison to Mn^{2+}

oxidation (see Equations 5.1-5.2). Titanium could not be used to deposit NEMD, most likely due to the passivation layer that forms at room temperature.

$Mn^{2+} + 2H_2O \rightarrow MnO_2 + 4H^+ + 2e^-$ E_{Ox} = -1.224 V_{SHE} **Equation 5.1**

$Ni \rightarrow Ni^{2+} + 2e^-$ E_{Ox} = 0.257 V_{SHE} **Equation 5.2**

For further work on NEMD synthesis, the following recommendations can be made:

- Coating a titanium electrode with a thin layer of conductive, stable material, i.e., gold.
- Continue using a nickel anode, but saturate the electrolyte solution with Ni^{2+} to limit anode corrosion or add a buffer to the electrolyte to increase the pH and limit corrosion.
- Attempt to use other metals plates (e.g. iron, lead, etc.) or alloys (e.g. stainless steel, brass, etc.) to deposit NEMD, which do not corrode as much.

5.2.5 Investigating Large Scale In-Situ MnO_2-Zn Cells

A thorough investigation of the gravimetric and volumetric energy density of the in-situ MnO_2-Zn batteries is required. Currently, the areal capacity of the in-situ MnO_2-Zn batteries is too low for commercialization. However, preliminary results from the new cycling method using time-limited galvanostatic charging method rather than a potentiostatic charging method shows that the areal capacity can be increased by 10 folds (from 0.1 to 1 mAh cm^{-2}). This mode of cycling method can further lead to a nominal cell voltage to 1.5 V_{cell} which is about 30 mV higher than

the previous method of making in-situ NEMD cells. New cycle methods may provide further improvements.

Table 5.1 displays some preliminary calculations for the volumetric energy and gravimetric capacity of the cathode of the in-situ and ex-situ NEMD cells. Analysis is done for various areal capacities. Calculations for the KOH based cell using 2 M H_2SO_4 EMD and the copper intercalated bismuth doped birnessite MnO_2 are also done. It is important to note that the calculations for the copper intercalated battery includes many assumptions taken from the original article.

As it can be seen from the table, by increasing the areal capacity of the NEMD cell from 1 mAh g^{-1}_{MnO2} to 5 mAh g^{-1}_{MnO2}, a commercialized battery can be produced with a volumetric energy comparable to bismuth doped birnessite MnO_2 cell. However, the cyclability of such a high areal capacity NEMD cell must be investigated further.

Table 5.1 Investigation of the specific energy and capacity of in-situ NEMD $ZnSO_4$ based cell with various areal capacities as compared to a 2 M EMD KOH based cell and the recently reported Bi/Cu-doped MnO_2 KOH based cell.

	In-Situ NEMD	Ex-Situ NEMD	2 M H_2SO_4 EMD	Cu/Bi Birnessite
Electrolyte	2 M $ZnSO_4$	2 M $ZnSO_4$	9 M KOH	9 M KOH
Nominal Voltage *(V)*	1.2-1.5	1.2	1.2	0.8
Cycles	At least 100	At least 100	100	5,000
No. of Cell for 12 V Cell Pack	8-9	9	10	15
Gravimetric Capacity of Cathode *(mAh g^{-1})*	120	100	75	617
Electrode Thickness *(mm)*	0.25	0.25	0.6	0.6 *(estimated)*
Volumetric Energy of Cell *(Wh L^{-1})*	6.1 *(0.1 mAh cm^{-2})*	4.8 *(0.1 mAh cm^{-2})*	200 *(10 mAh cm^{-2})*	320 *(24 mAh cm^{-2})*
with varying areal capacity	61 *(1 mAh cm^{-2})*	48 *(1 mAh cm^{-2})*		
	305 *(5 mAh cm^{-2})*	240 *(5 mAh cm^{-2})*		
Volumetric Energy of Cell *(Wh L^{-1})*	7.6 *(1 mg cm^{-2})*	4.8 *(1 mg cm^{-2})*	200 *(75 mg cm^{-2})*	320 *(40 mg cm^{-2})*
with varying areal loading	76 *(10 mg cm^{-2})*	48 *(10 mg cm^{-2})*		
	380 *(50 mg cm^{-2})*	240 *(50 mg cm^{-2})*		

References

[1] D. Downs and A. Meyerhoff, “Battery, Baghdad, 250 BCE,” *Smith Education*, 2014. [Online]. Available: https://www.smith.edu/hsc/museum/ancient_inventions/battery2.html. [Accessed: 12-Dec-2016].

[2] W. M. Sudduth, “The Voltaic Pile and Electro-Chemical Theory in 1800,” *Ambix*, vol. 27, no. 1, pp. 26–35, 1980.

[3] A. Boulabiar, K. Bouraoui, M. Chastrette, and M. Abderrabba, “A Historical Analysis of the Daniell Cell and Electrochemistry Teaching in Frnce and Tunisian Textbooks.,” *J. Chem. Educ.*, vol. 81, no. 5, pp. 754–757, 2004.

[4] Z. Rogulski and A. Czerwiński, “New cathode mixture for the zinc-manganese dioxide cell,” *J. Power Sources*, vol. 114, no. 1, pp. 176–179, 2003.

[5] “The Baghdad Battery,” *Aquiziam Mysteries*. [Online]. Available: https://www.aquiziam.com/ancient-electricity/baghdad-battery/. [Accessed: 24-Oct-2016].

[6] “Primary Lithium Cells,” *Varta Microbattery*. [Online]. Available: http://www.varta-microbattery.com/applications/mb_data/documents/sales_literature_varta/HANDBOOK_Primary_Lithium_Cells_en.pdf. [Accessed: 02-Nov-2016].

[7] C. Chakkaravarthy, A. K. A. Waheed, and H. V. K. Udupa, “Zinc-Air Alkaline Batteries - A Review,” *J. Power Sources*, vol. 6, no. 3, pp. 203–228, 1981.

[8] K. R. Bullock, “Lead/acid batteries,” *J. Power Sources*, vol. 51, no. 2, pp. 1–17, 1994.

[9] J. M. Tarascon and M. Armand, “Issues and challenges facing rechargeable lithium batteries.,” *Nature*, vol. 414, no. 6861, pp. 359–367, 2001.

[10] A. K. Shukla, S. Venugopalan, and B. Hariprakash, “Nickel-based rechargeable batteries,” *J. Power Sources*, vol. 100, pp. 125–148, 2001.

[11] R. Bussar, M. Lippert, G. Bonduelle, R. Linke, G. Crugnola, J. Cilia, K. D. Merz, C. Heron, and E. Marckx, “Battery Energy Storage for Smart Grid Applications,” *Eurobat*, 2013.

[Online]. Available: https://eurobat.org/sites/default/files/eurobat_smartgrid_publication_may_2013.pdf. [Accessed: 12-Nov-2017].

[12] G. Fuchs, B. Lunz, M. Leuthold, and D. U. Sauer, "Technology Overview on Electricity Storage - Overview on the potential and on the deployment perspectives of electric storage technologies," *Institute for Power Electronics and Electrical Drives (ISEA), RWTH Aachen University*, 2012. [Online]. Available: https://www.researchgate.net/profile/Dirk_Sauer/publication/299425278_Technology_Overview_on_Electricity_Storage_-_Overview_on_the_potential_and_on_the_deployment_perspectives_of_electricity_storage_technologies/links/56f5bdca08ae81582bf21724.pdf. [Accessed: 20-Nov-2016].

[13] P. Somavat and V. Namboodiri, "Energy consumption of personal computing including portable communication devices," *J. Green Eng.*, vol. 1, no. 4, pp. 447–475, 2011.

[14] O. Travesset-Baro, M. Rosas-Casals, and E. Jover, "Transport energy consumption in mountainous roads. A comparative case study for internal combustion engines and electric vehicles in Andorra," *Transp. Res. Part D Transp. Environ.*, vol. 34, pp. 16–26, 2015.

[15] B. Urban, V. Shmakova, B. Lim, and K. Roth, "Energy Consumption of Consumer Electronics in U.S. Homes in 2013," *Fraunhofer USA Center for Sustainable Energy Systems*, 2013. [Online]. Available: http://www.ce.org/CorporateSite/media/environment/Energy-Consumption-of-Consumer-Electronics.pdf. [Accessed: 15-Dec-2016].

[16] H. Wang, X. Zhang, and M. Ouyang, "Energy consumption of electric vehicles based on real-world driving patterns: A case study of Beijing," *Appl. Energy*, vol. 157, pp. 710–719, 2015.

[17] T. Trigg, P. Telleen, R. Boyd, F. Cuenot, D. D'Ambrosio, R. Gaghen, J. F. Gagné, A. Hardcastle, D. Houssin, A. R. Jones, and H. Kaneko, "Global EV Outlook: Understanding the Electric Vehicle Landscape to 2020," 2013.

[18] S. Abada, G. Marlair, A. Lecocq, M. Petit, V. Sauvant-Moynot, and F. Huet, "Safety focused modeling of lithium-ion batteries: A review," *J. Power Sources*, vol. 306, pp. 178–192, 2016.

[19] N. Alias and A. A. Mohamad, "Advances of aqueous rechargeable lithium-ion battery: A review," *J. Power Sources*, vol. 274, pp. 237–251, 2015.

[20] M. A. Kiani, M. F. Mousavi, and M. S. Rahmanifar, “Synthesis of nano-and micro-particles of LiMn2O4: electrochemical investigation and assessment as a cathode in Li battery.,” *Int. J. Electrochem. Sci.*, vol. 6, pp. 2581–2595, 2011.

[21] A. Z. Weber, M. M. Mench, J. P. Meyers, P. N. Ross, J. T. Gostick, and Q. Liu, “Redox flow batteries: A review,” *J. Appl. Electrochem.*, vol. 41, no. 10, pp. 1137–1164, 2011.

[22] P. Alotto, M. Guarnieri, and F. Moro, “Redox flow batteries for the storage of renewable energy: A review,” *Renew. Sustain. Energy Rev.*, vol. 29, pp. 325–335, 2014.

[23] A. Biswal, B. Chandra Tripathy, K. Sanjay, T. Subbaiah, and M. Minakshi, “Electrolytic manganese dioxide (EMD): a perspective on worldwide production, reserves and its role in electrochemistry,” *RSC Adv.*, vol. 5, no. 72, pp. 58255–58283, 2015.

[24] A. Emadi, “A New Battery/UltraCapacitor Hybrid Energy Storage System for Electric, Hybrid, and Plug-In Hybrid Electric Vehicles,” *IEEE Trans. Power Electron.*, vol. 27, no. 1, pp. 122–132, 2012.

[25] D. P. Dubal, O. Ayyad, V. Ruiz, and P. Gómez-Romero, “Hybrid energy storage: the merging of battery and supercapacitor chemistries,” *Chem. Soc. Rev.*, vol. 44, no. 7, pp. 1777–1790, 2015.

[26] J. Daniel-Ivad, “Zinc-Manganese,” in *Encyclopedia of Electrochemical Power Sources*, vol. 5, 2009, pp. 497–512.

[27] M. Ghaemi, L. Khosravi-fard, and J. Neshati, “Improved performance of rechargeable alkaline batteries via surfactant-mediated electrosynthesis of MnO2,” *J. Power Sources*, vol. 141, no. 1, pp. 340–350, 2005.

[28] V. K. Nartey, L. Binder, and A. Huber, “Production and characterisation of titanium doped electrolytic manganese dioxide for use in rechargeable alkaline zinc / manganese dioxide batteries,” *J. Power Sources*, vol. 87, no. 1, pp. 205–211, 2000.

[29] B. Dunn, H. Kamath, and J. Tarascon, “Electrical Energy Storage for the Grid : A Battery of Choices,” *Mater. Grid Energy*, vol. 334, no. 6058, pp. 928–935, 2011.

[30] J. Cho, S. Jeong, and Y. Kim, “Commercial and research battery technologies for electrical energy storage applications,” *Prog. Energy Combust. Sci.*, vol. 48, pp. 84–101, 2015.

[31] “Metalary,” *Metalary*, 2016. [Online]. Available: https://www.metalary.com/. [Accessed:

14-Dec-2016].

[32] “Infomine,” *InfoMine Inc.*, 2016. [Online]. Available: http://www.infomine.com/. [Accessed: 16-Dec-2016].

[33] M. Winter, “Webelements,” *WebElements Ltd.*, 2016. [Online]. Available: https://www.webelements.com/. [Accessed: 20-Jan-2017].

[34] D. Larcher and J.-M. Tarascon, “Towards greener and more sustainable batteries for electrical energy storage,” *Nat. Chem.*, vol. 7, no. 1, pp. 19–29, 2015.

[35] S. Mehta, “Investigation of Capacity Fade in Flat-Plate Rechargeable Alkaline MnO2/Zn Cells,” 2016.

[36] I. Buchmann, “What’s the Best Battery?,” *Battery University*, 2017. [Online]. Available: http://batteryuniversity.com/learn/archive/whats_the_best_battery. [Accessed: 11-Jan-2017].

[37] K. Kordesch and M. Weissenbacher, “Rechargeable alkaline manganese dioxide/zinc batteries,” *J. Power Sources*, vol. 51, pp. 61–78, 1994.

[38] A. Stani, W. Taucher-Mautner, K. Kordesch, and J. Daniel-Ivad, “Development of flat plate rechargeable alkaline manganese dioxide-zinc cells,” *J. Power Sources*, vol. 153, pp. 405–412, 2006.

[39] S. A. Mehta, A. Bonakdarpour, and D. P. Wilkinson, “Impact of cathode additives on the cycling performance of rechargeable alkaline manganese dioxide–zinc batteries for energy storage applications,” *J. Appl. Electrochem.*, vol. 47, no. 2, pp. 167–181, 2017.

[40] H. Adelkhani and M. Ghaemi, “Influence of the solution pH on the nanostructural, and electrochemical performance of electrolytic manganese dioxide,” *J. Alloys Compd.*, vol. 481, pp. 446–449, 2009.

[41] M. Minakshi, “Improved performance of Bi2O3-doped MnO2 cathode on rechargeability in LiOH aqueous cell,” *J. Solid State Electrochem.*, vol. 13, no. 8, pp. 1209–1214, 2009.

[42] H. Pan, Y. Shao, P. Yan, Y. Cheng, K. S. Han, Z. Nie, C. Wang, J. Yang, X. Li, P. Bhattacharya, K. T. Mueller, and J. Liu, “Reversible aqueous zinc/manganese oxide energy storage from conversion reactions,” *Nat. Energy*, vol. 1, 2016.

[43] M. R. Bailey and S. W. Donne, “The Effect of Barium Hydroxide on the Rechargeable Performance of Alkaline γ-MnO2,” *J. Electrochem. Soc.*, vol. 159, no. 7, pp. A999–A1004, 2012.

[44] M. Minakshi, M. Blackford, and M. Ionescu, “Characterization of alkaline-earth oxide additions to the MnO2 cathode in an aqueous secondary battery,” *J. Alloys Compd.*, vol. 509, no. 20, pp. 5974–5980, 2011.

[45] H. Adelkhani, “The effect of acidity of electrolyte on the porosity and the nanostructure morphology of electrolytic manganese dioxide,” *Appl. Surf. Sci.*, vol. 258, no. 17, pp. 6232–6238, Jun. 2012.

[46] H. Adelkhani, M. Ghaemi, and S. M. Jafari, “Cycle life improvement of alkaline batteries via optimization of pulse current deposition of manganese dioxide under low bath temperatures,” *J. Power Sources*, vol. 163, no. 2, pp. 1091–1104, Jan. 2007.

[47] H. Adelkhani, “Functionalized Electrolytic Manganese Dioxide Nanostructure Prepared at Fixed pH for Electrochemical Supercapacitor,” *J. Electrochem. Soc.*, vol. 156, no. 10, pp. A791–A795, 2009.

[48] S. M. Davis, “Plating of High Quality Electrolytic Manganese Dioxide at 120-125 Degrees C. and 6X Normal Current Density,” *J. New Mater. Electrochem. Syst.*, no. 7, pp. 257–268, 2004.

[49] M. Devenney, S. W. Donne, and S. Gorer, “Application of combinatorial methodologies to the synthesis and characterization of electrolytic manganese dioxide,” *J. Appl. Electrochem.*, vol. 34, no. 6, pp. 643–651, 2004.

[50] M. Ghaemi, Z. Biglari, and L. Binder, “Effect of bath temperature on electrochemical properties of the anodically deposited manganese dioxide,” *J. Power Sources*, vol. 102, no. 1–2, pp. 29–34, 2001.

[51] A. J. B. Dutra and I. C. F. Almeida, “Electrolytic Manganese Dioxide Nucleation and Growth on Titanium Substrates,” *Mater. Sci. Forum*, vol. 570, pp. 114–119, 2008.

[52] M. Minakshi, P. Singh, D. R. G. Mitchell, T. B. Issa, and K. Prince, “A study of lithium insertion into MnO2 containing TiS2 additive a battery material in aqueous LiOH solution,” *Electrochim. Acta*, vol. 52, no. 24, pp. 7007–7013, 2007.

[53] M. Minakshi, D. R. G. Mitchell, M. L. Carter, D. Appadoo, and K. Nallathamby,

"Microstructural and spectroscopic investigations into the effect of CeO2 additions on the performance of a MnO2 aqueous rechargeable battery," *Electrochim. Acta*, vol. 54, no. 12, pp. 3244–3249, 2009.

[54] M. Minakshi, K. Nallathamby, and D. R. G. Mitchell, "Electrochemical characterization of an aqueous lithium rechargeable battery: The effect of CeO2 additions to the MnO2 cathode," *J. Alloys Compd.*, vol. 479, no. 1–2, pp. 87–90, 2009.

[55] M. Minakshi, P. Singh, M. Carter, and K. Prince, "The Zn–MnO2 Battery: The Influence of Aqueous LiOH and KOH Electrolytes on the Intercalation Mechanism," *Electrochem. Solid-State Lett.*, vol. 11, no. 8, pp. A145–A149, 2008.

[56] V. Raghuveer and A. Manthiram, "Improved rechargeability of manganese oxide cathodes in alkaline cells in the presence of TiB2 and TiS2," *J. Power Sources*, vol. 159, no. 2, pp. 1468–1473, 2006.

[57] V. Raghuveer and A. Manthiram, "Role of TiB2 and Bi2O3 additives on the rechargeability of MnO2 in alkaline cells," *J. Power Sources*, vol. 163, no. 1, pp. 598–603, 2006.

[58] Y. Wenjian, L. Juan, and Z. Xiaogang, "Enhanced electrochemical properties of manganese dioxde doped with Ag3BiOx," *Int. J. Electrochem. Sci.*, vol. 1, no. 4, pp. 181–188, 2006.

[59] V. Raghuveer and A. Manthiram, "Effect of BaBiO3 and Ba0.6K0.4BiO 3 additives on the rechargeability of manganese oxide cathodes in alkaline cells," *Electrochem. commun.*, vol. 7, no. 12, pp. 1329–1332, 2005.

[60] J. Pan, Y. Sun, P. Wan, Z. Wang, and X. Liu, "Preparation of NaBiO3 and the electrochemical characteristic of manganese dioxide doped with NaBiO3," *Electrochim. Acta*, vol. 51, no. 15, pp. 3118–3124, 2006.

[61] M. Manickam, P. Singh, T. B. Issa, S. Thurgate, and R. De Marco, "Lithium insertion into manganese dioxide electrode in MnO2/Zn aqueous battery: Part I. A preliminary study," *J. Power Sources*, vol. 130, no. 1–2, pp. 254–259, 2004.

[62] M. Minakshi, "Looking beyond lithium-ion technology - Aqueous NaOH battery," *Mater. Sci. Eng. B Solid-State Mater. Adv. Technol.*, vol. 177, no. 20, pp. 1788–1792, 2012.

[63] M. Minakshi and D. Meyrick, "Electrochemical energy storage device for securing future renewable energy," *Electrochim. Acta*, vol. 101, pp. 66–70, 2013.

[64] D. K. Kim, P. Muralidharan, H.-W. Lee, R. Ruffo, Y. Yang, C. K. Chan, H. Peng, R. A. Huggins, and Y. Cui, “Spinel LiMn2O4 Nanorods as Lithium Ion Battery Cathodes,” *Nano Lett.*, vol. 8, no. 11, pp. 3948–3952, 2008.

[65] S. Chen, J. Zhu, X. Wu, Q. Han, and X. Wang, “Graphene oxide-Mno2 nanocomposites for supercapacitors,” *ACS Nano*, vol. 4, no. 5, pp. 2822–2830, 2010.

[66] F. Cheng, Y. Su, J. Liang, Z. Tao, and J. Chen, “MnO2-Based Nanostructures as Catalysts for Electrochemical Oxygen Reduction in Alkaline Media,” *Chem. Mater.*, vol. 22, no. 3, pp. 898–905, 2010.

[67] M. Huang, F. Li, F. Dong, X. Zhang, and L. Li, “MnO2-based nanostructures for high-performance supercapacitors,” *J. Mater. Chem. A Mater. energy Sustain.*, vol. 3, no. 43, pp. 21380–21423, 2015.

[68] S. W. Joo, M. A. Cheney, P. K. Bhowmik, S. Moriuchi, M. Villalobos, and S. Qian, “The Effect of Stirring on the Morphology of Birnessite Nanoparticles,” *J. Nanomater.*, vol. 2008, no. 1, pp. 1–10, 2008.

[69] H. Bin Wu, J. S. Chen, H. H. Hng, and X. W. D. Lou, “Nanostructured metal oxide-based materials as advanced anodes for lithium-ion batteries,” *Nanoscale*, vol. 4, no. 8, pp. 2526–2542, 2012.

[70] G. Li, M. A. Mezaal, R. Zhang, K. Zhang, and L. Lei, “Electrochemical Performance of MnO2- based Air Cathodes for Zinc-air Batteries,” *Fuel Cells*, vol. 16, no. 3, pp. 395–400, 2016.

[71] M. M. Thackeray, C. S. Johnson, J. T. Vaughey, N. LiCurrent address: eVionyx Inc., Ha, and S. A. Hackney, “Advances in manganese-oxide ‘composite’ electrodes for lithium-ion batteries,” *J. Mater. Chem.*, vol. 15, no. 23, pp. 2257–2267, 2005.

[72] P. Ruetschi and R. Giovanoli, “Cation Vacancies in MnO2 and Their Influence on Electrochemical Reactivity,” *J. Electrochem. Soc.*, vol. 135, no. 11, pp. 2663–2669, 1988.

[73] P. Ruetschi, “Influence of Cation Vacancies on the Electrode Potential of MnO2,” *J. Electrochem. Soc.*, vol. 135, no. 11, pp. 2657–2663, 1988.

[74] Y. Chabre and J. Pannetier, “Structural and electrochemical properties of the proton / γ-MnO2 system,” *Prog. Solid State Chem.*, vol. 23, no. 94, pp. 1–130, 1995.

[75] H. Abbas and S. A. Nasser, “Hydroxyl as a defect of the manganese dioxide lattice and its applications to the dry cell battery,” *J. Power Sources*, vol. 58, no. 1, pp. 15–21, 1996.

[76] A. P. Malloy and S. W. Donne, “Surface characterisation of chemically reduced electrolytic manganese dioxide,” *J. Colloid Interface Sci.*, vol. 320, no. 1, pp. 210–218, 2008.

[77] C. Poinsignon, J. M. Amarilla, and F. Tedjar, “Electrochemical Reduction of β-MnO2, Ramsdellite, γ- and ε-MnO2,” *Solid State Ionics*, vol. 39, no. 15, pp. 649–653, 1994.

[78] S. Bodoardo, N. Penazzi, P. Spinelli, and M. Arrabito, “Influence of aluminium doping on the electrochemical behaviour of manganese dioxide,” *J. Power Sources*, vol. 94, no. 2, pp. 194–200, 2001.

[79] H. Tamura, K. Ishizeki, M. Nagayama, and R. Furuichi, “Incorporation of Impurity Metal Ions in Electrolytic Manganese Dioxide,” *J. Electrochem. Soc.*, vol. 141, no. 8, pp. 5–10, 1994.

[80] V. S. Kolosnitsyn, E. A. Minnikhanova, E. V. Karaseva, Y. K. Dmitriev, and M. M. Muratov, “Effect of Ca2+, Mg2+, Fe3+, and Al3+ ions on the deposition of electrolytic manganese dioxide from chloride solutions,” *Russ. J. Appl. Chem.*, vol. 78, no. 5, pp. 737–740, 2005.

[81] C. G. Castledine and B. E. Conway, “Effects of electrochemically incorporated bismuth on the discharge and recharge of electrodeposited manganese dioxide films in 9 M aqueous KOH,” *J. Appl. Electrochem.*, vol. 25, no. 8, pp. 707–715, 1995.

[82] W. Jantscher, L. Binder, D. A. Fiedler, R. Andreaus, and K. Kordesch, “Synthesis, characterization and application of doped electrolytic manganese dioxides,” *J. Power Sources*, vol. 79, no. 1, pp. 9–18, 1999.

[83] A. Biswal, B. C. Tripathy, T. Subbaiah, D. Meyrick, and M. Minakshi, “Electrodeposition of manganese dioxide: Effect of quaternary amines,” *J. Solid State Electrochem.*, vol. 17, no. 5, pp. 1349–1356, 2013.

[84] R. K. Ghavami, Z. Rafiei, and S. M. Tabatabaei, “Effects of cationic CTAB and anionic SDBS surfactants on the performance of Zn-MnO2 alkaline batteries,” *J. Power Sources*, vol. 164, no. 2, pp. 934–946, 2007.

[85] A. Biswal, B. Chandra Tripathy, T. Subbaiah, D. Meyrick, and M. Minakshi, “Dual Effect of Anionic Surfactants in the Electrodeposited MnO2 Trafficking Redox Ions for Energy

Storage," *J. Electrochem. Soc.*, vol. 162, no. 1, pp. A30–A38, 2014.

[86] S. Devaraj and N. Munichandraiah, "The effect of nonionic surfactant Triton X-100 during electrochemical deposition of MnO2 on its capacitance properties," *J. Electrochem. Soc.*, vol. 154, no. 10, pp. A901–A909, 2007.

[87] A. Biswal, B. C. Tripathy, T. Subbaiah, D. Meyrick, M. Ionescu, and M. Minakshi, "Effect of Non-ionic Surfactants and Its Role in K Intercalation in Electrolytic Manganese Dioxide," *Metall. Mater. Trans. E*, vol. 1, no. 3, pp. 226–238, 2014.

[88] F. Cheng, J. Zhao, W. Song, C. Li, H. Ma, J. Chen, and P. Shen, "Facile controlled synthesis of MnO2 nanostructures of novel shapes and their application in batteries," *Inorg. Chem.*, vol. 45, no. 5, pp. 2038–2044, 2006.

[89] H. You-ju, L. I. N. Yu-li, and L. I. Wei-shan, "Manganese Dioxide with High Specific Surface Area for Alkaline Battery," *Chem. Res. Chinese Univ.*, vol. 28, no. 5, pp. 874–877, 2012.

[90] M. H. Alfaruqi, J. Gim, S. Kim, J. Song, J. Jo, S. Kim, V. Mathew, and J. Kim, "Enhanced reversible divalent zinc storage in a structurally stable a-MnO2 nanorod electrode," *J. Power Sources*, vol. 288, no. 32, pp. 320–327, 2015.

[91] B. Lee, H. R. Lee, H. Kim, K. Y. Chung, B. W. Cho, and S. H. Oh, "Elucidating the intercalation mechanism of zinc ions into a-MnO2 for rechargeable zinc batteries," *Chem Commun*, vol. 51, no. 45, pp. 9265–9268, 2015.

[92] B. Lee, C. S. Yoon, H. R. Lee, K. Y. Chung, B. W. Cho, and S. H. Oh, "Electrochemically-induced reversible transition from the tunneled to layered polymorphs of manganese dioxid," *Sci. Rep.*, vol. 4, p. 6066, 2014.

[93] T. Shoji, M. Hishinuma, and T. Yamamoto, "Zinc-Manganese Dioxide Galvanic Cell Using Zinc Sulphate as Electrolyte. Rechargeability of the Cell," *J. Appl. Electrochem.*, vol. 18, no. 4, pp. 521–526, 1988.

[94] C. Xu, S. W. Chiang, J. Ma, and F. Kang, "Investigation on Zinc Ion Storage in Alpha Manganese Dioxide for Zinc Ion Battery by Electrochemical Impedance Spectrum," *J. Electrochem. Soc.*, vol. 160, no. 1, pp. A93–A97, 2012.

[95] C. Xu, H. Du, B. Li, F. Kang, and Y. Zeng, "Reversible Insertion Properties of Zinc Ion into Manganese Dioxide and Its Application for Energy Storage," *Electrochem. Solid-State Lett.*, vol. 12, no. 4, pp. A61–A65, 2009.

[96] C. Xu, B. Li, H. Du, and F. Kang, “Energetic zinc ion chemistry: The rechargeable zinc ion battery,” *Angew. Chemie - Int. Ed.*, vol. 51, no. 4, pp. 933–935, 2012.

[97] D. Xu, B. Li, C. Wei, Y. B. He, H. Du, X. Chu, X. Qin, Q. H. Yang, and F. Kang, “Preparation and characterization of MnO2/acid-treated CNT nanocomposites for energy storage with zinc ions,” *Electrochim. Acta*, vol. 133, pp. 254–261, 2014.

[98] M. H. Alfaruqi, V. Mathew, J. Gim, S. Kim, J. Song, J. P. Baboo, S. H. Choi, and J. Kim, “Electrochemically Induced Structural Transformation in a γ-MnO2 Cathode of a High Capacity Zinc-Ion Battery System,” *Chem. Mater.*, vol. 27, no. 10, pp. 3609–3620, 2015.

[99] E. Preisler, “Material Problems Encountered in Anodic MnO2 Deposition,” *J. Appl. Electrochem.*, vol. 19, no. 4, pp. 559–565, 1989.

[100] Q. Feng, K. Yanagisawa, and N. Yamasaki, “Hydrothermal Soft Chemical Process for Synthesis of Manganese Oxides with Tunnel Structures,” *J. Porous Mater.*, vol. 5, no. 2, pp. 153–161, 1998.

[101] R. M. McKenzie, “The Synthesis of Birnessite, Cryptomelane, and Some Other Oxides and Hydroxides of Manganese,” *Mineral. Mag.*, vol. 38, no. 296, pp. 493–502, 1971.

[102] M. M. Thackeray, M. H. Rossouw, R. J. Gummow, D. C. Liles, K. Pearce, A. De Kock, W. I. F. David, and S. Hull, “Ramsdellite-MnO2 for Lithium Batteries : The Ramsdellite to Spinel Formation,” *Electrochim. Acta*, vol. 38, no. 9, pp. 1259–1267, 1993.

[103] “Basic overview of the working principle of a potentiostat/galvanostat (PGSTAT) – Electrochemical cell setup,” *Metrohm Autolab*. [Online]. Available: http://autolabinstruments.com/download/Applicationnotes/Autolab_Application_Note_EC08.pdf. [Accessed: 09-Feb-2017].

[104] T. T. Kam, “Some Electrochemical Studies of Mercury-Mercuric Oxide Electrode with an Inner Electrolyte of 33 wt-vol% Sodium Hydroxide,” *Electrochim. Acta*, vol. 27, no. 5, pp. 553–555, 1981.

[105] M. Vukovi, “Voltammetry and anodic stability of a hydrous oxide film on a nickel electrode in alkaline solution,” *J. Appl. Electrochem.*, vol. 24, no. 9, pp. 878–882, 1994.

[106] “Agilent Impedance Measurement Handbook A guide to measurement technology and techniques,” *Agilent*, 2013. [Online]. Available: http://literature.cdn.keysight.com/litweb/pdf/5950-3000.pdf. [Accessed: 14-Dec-2016].

[107] “Corrosion Part 4 – Equivalent Circuit Models,” *Metrohm*, 2011. [Online]. Available: https://www.metrohm.com/en/applications/%7BF3B3FFBA-F24F-4810-A37D-85B8A1BB15EE%7D. [Accessed: 20-Jan-2017].

[108] M. Birkholz, “Principles of X-ray Diffraction,” in *Thin Film Analysis by X-Ray Scattering*, 2005, pp. 1–42.

[109] “Gas Adsorption Theory,” *Micromeritics Instrument Corp.*, 2015. [Online]. Available: http://www.micromeritics.com/Repository/Files/Gas_Adsorption_Theory_poster.pdf. [Accessed: 20-Jan-2017].

[110] P. Brouwer, *Theory of XRF*. Almelo, Netherlands, 2010.

[111] B. Prélot, F. Villiéras, M. Pelletier, A. Razafitianamaharavo, F. Thomas, and C. Poinsignon, “Structural–chemical disorder of manganese dioxides: II. Influence on textural properties,” *J. Colloid Interface Sci.*, vol. 264, no. 2, pp. 343–353, 2003.

[112] J. C. Groen, L. A. A. Peffer, and P. Javier, “Pore size determination in modified micro-and mesoporous materials. Pitfalls and limitations in gas adsorption data analysis.,” *Microporous Mesoporous Mater.*, vol. 60, no. 1, pp. 1–17, 2003.

[113] D. Qu, “Investigation of the porosity of electrolytic manganese dioxide and its performance as alkaline cathode material,” *J. Power Sources*, vol. 156, no. 2, pp. 692–699, 2006.

[114] C. C. Chen, J. H. Chen, C. G. Chao, and W. C. Say, “Electrochemical characteristics of surface of titanium formed by electrolytic polishing and anodizing,” *J. Mater. Sci.*, vol. 40, no. 15, pp. 4053–4059, 2005.

[115] J. Yang, X. Kang, L. Hu, X. Gong, D. He, T. Peng, and S. Mu, “Synthesis and electrochemical performance of Li2FeSiO4/C/carbon nanosphere composite cathode materials for lithium ion batteries,” *J. Alloys Compd.*, vol. 572, pp. 158–162, 2013.

[116] D. Qu, “The study of the proton diffusion process in the porous MnO2 electrode,” *Electrochim. Acta*, vol. 49, no. 4, pp. 657–665, 2004.

[117] G. G. Yadav, J. W. Gallaway, D. E. Turney, M. Nyce, J. Huang, X. Wei, and S. Banerjee, “Regenerable Cu-intercalated MnO2 layered cathode for highly cyclable energy dense batteries,” *Nat. Commun.*, vol. 8, no. May 2016, p. 14424, 2017.

[118] S. W. Donne, F. H. Feddrix, R. Glo, S. Marion, and T. Norby, “Water and protons in electrodeposited MnO2 (EMD),” in *Solid State Ionics*, 2002, vol. 153, pp. 695–701.

[119] S. W. Donne, G. A. Lawrance, and D. A. J. Swinkels, “Redox Processes at the Manganese Dioxide Electrode I. Constant - Current Intermittent Discharge,” *J. Electrochem. Soc.*, vol. 144, no. 9, p. 2949, 1997.

[120] B. Jiang, C. Xu, C. Wu, L. Dong, J. Li, and F. Kang, “Manganese Sesquioxide as Cathode Material for Multivalent Zinc Ion Battery with High Capacity and Long Cycle Life,” *Electrochim. Acta*, vol. 229, pp. 422–428, 2017.

[121] B. J. Hertzberg, A. Huang, A. Hsieh, M. Chamoun, G. Davies, J. K. Seo, Z. Zhong, M. Croft, C. Erdonmez, Y. S. Meng, and D. Steingart, “Effect of Multiple Cation Electrolyte Mixtures on Rechargeable Zn-MnO2 Alkaline Battery,” *Chem. Mater.*, vol. 28, no. 13, pp. 4536–4545, 2016.

[122] F. Kang, C. XU, B. Li, and H. DU, “Rechargeable Zinc Ion Battery,” US8,663,844.

[123] G. Y. Li, J. S. Lian, L. Y. Niu, and Z. H. Jiang, “Investigation of nanocrystalline zinc-nickel alloy coatings in an alkaline zincate bath,” *Surf. Coatings Technol.*, vol. 191, no. 1, pp. 59–67, 2005.

[124] M. Bode, C. Cachet, S. Bach, J.-P. Pereira-Ramos, J. C. Ginoux, and L. 1. Yu, “Rechargeability of MnO2 in KOH Media Produced by Decomposition of Dissolved KMnO4 and Bi(NO3)3 Mixtures I. Mn-Bi Complexes,” *J. Electrochem. Soc.*, vol. 144, no. 3, pp. 802–809, 1997.

[125] H. S. Wroblowa and N. Gupta, “Rechargeable Manganese Oxide Electrodes: Part II. Physically Modified Materials,” *J. Electroanal. Chem. interfacial Electrochem.*, vol. 238, no. 1–2, pp. 93–102, 1987.

[126] Y. F. Yao, N. Gupta, and H. S. Wroblowa, “Rechargeable Manganese Oxide Electrodes: Part I. Chemically Modified Materials,” *J. Electroanal. Chem. interfacial Electrochem.*, vol. 223, no. 1–2, pp. 107–117, 1987.

[127] M. A. Dzieciuch, N. Gupta, and H. S. Wroblowa, “Rechargeable Cells with Modified MnO2 Cathodes,” *J. Electrochem. Soc.*, vol. 135, no. 10, pp. 2415–2418, 1988.

[128] B. Sajdl, K. Micka, and P. Krtil, “Study of the Rechargeable Manganese Dioxide Electrode,” *Electrochim. Acta*, vol. 40, no. 12, pp. 2005–2011, 1995.

[129] L. T. Yu, “Rechargeabilily of MnO2 in KOH Media Produced by Dissolved KMnO4 and Bi(NO3)3 Mixtures,” *J. Electrochem. Soc.*, vol. 144, no. 3, pp. 802–809, 1997.

Appendix A：Electrolysis of EMD and NEMD

A.1 Electrolysis Cell Components

The following table and figure present the details of the cell components used for EMD and NEMD electrolysis. The cell hardware, condenser, temperature control system, Ti/graphite electrodes, and heat sources were used for the EMD synthesis. The cell hardware and Ni/Zn electrodes were used for the NEMD synthesis.

Table A.1 Specifications of parts used for the electrolysis cell.

Part	Specification
Cell hardware	• Plexiglass Lid • 600 mL Pyrex® beaker

Condenser	• Quickfit® Liebig
	  ○ Length = 40 cm
	  ○ Joint: ST/NS 24/29

Temperature control	• Type K PTFE thermocouple (Corning) • Accu-Lab thermometer (1223M78)
Electrodes	• 4 cm × 14 cm × 2 mm Ti plate (McMaster-Carr; 9039K21) • 4 cm × 14 cm × 6 mm graphite plate (McMaster-Carr; 9015K83) • 16 cm × 14 cm × 0.04 mm Ni foil (MTI; MF-NiFoil-25u) folded four times • 4 cm × 14 cm × 0.5 mm Zn foil (Dexmet)
Heat source	• Isotemp Fisher Scientific 20N0207 • Corning PC-620D hot plate.

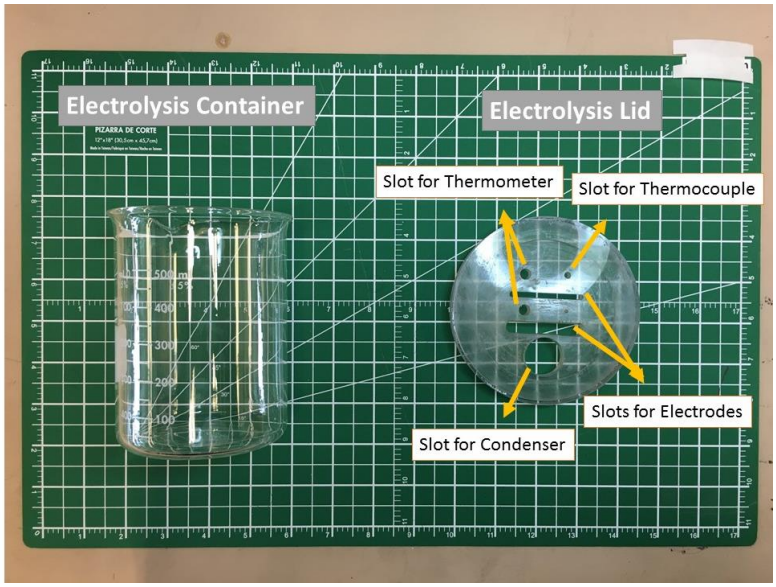

Figure A.1 Body of electrolysis cell (plexiglass lid and Pyrex® beaker).

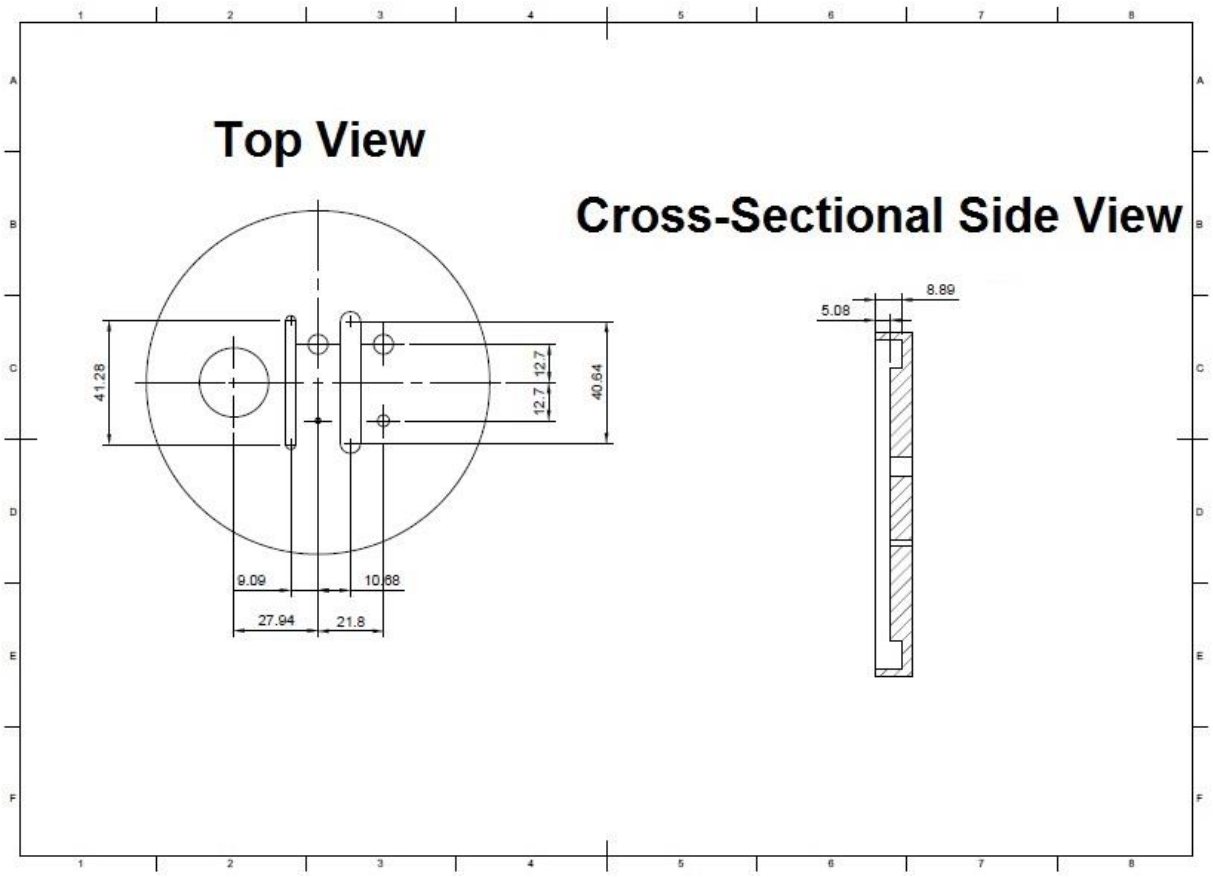

Figure A.2 Design of electrolysis cell plexiglass lid (all measurements are in mm).

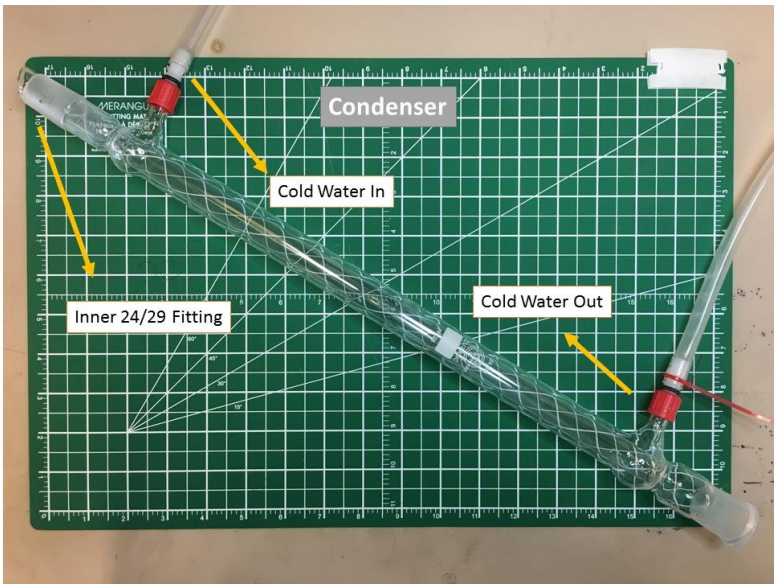

Figure A.3 *Condenser unit.*

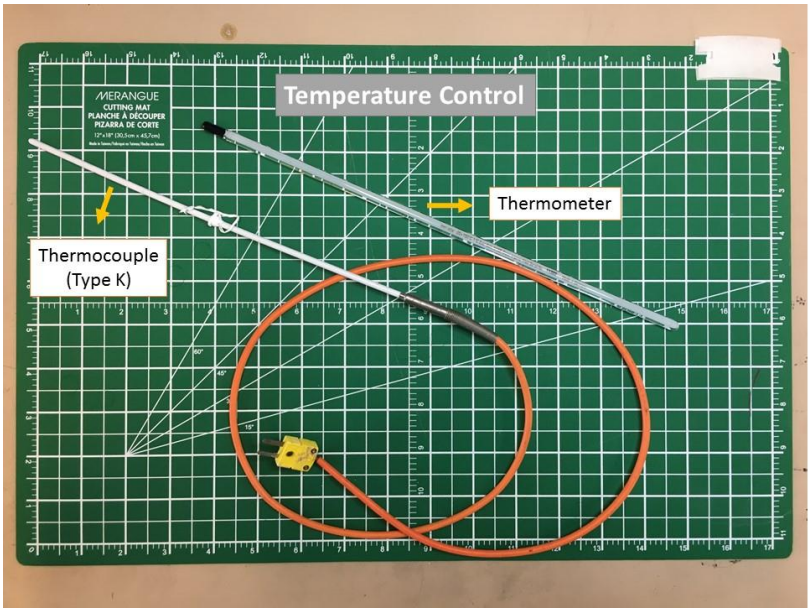

Figure A.4 *Temperature control system (thermocouple and thermometer).*

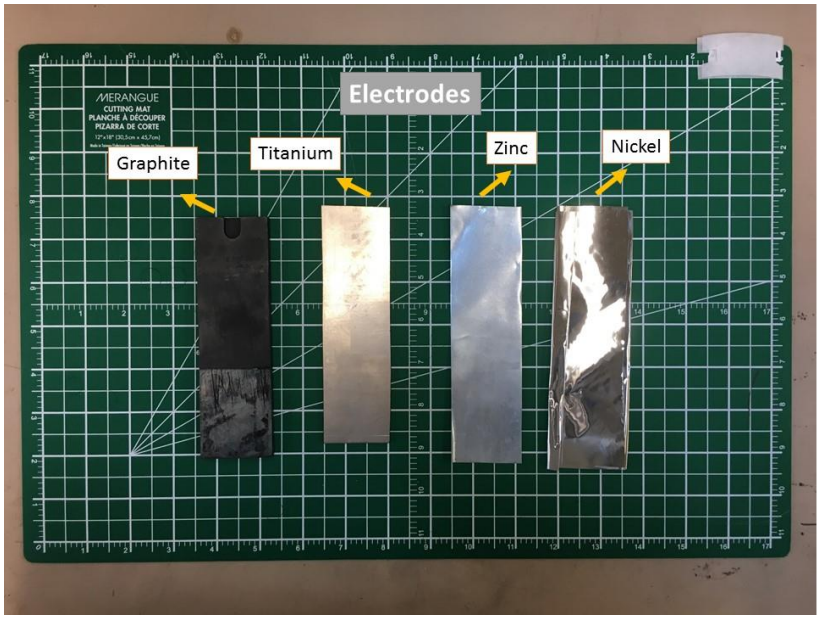

Figure A.5 Fresh electrolysis electrodes (Ti/graphite used for EMD and Ni/Zn used for NEMD).

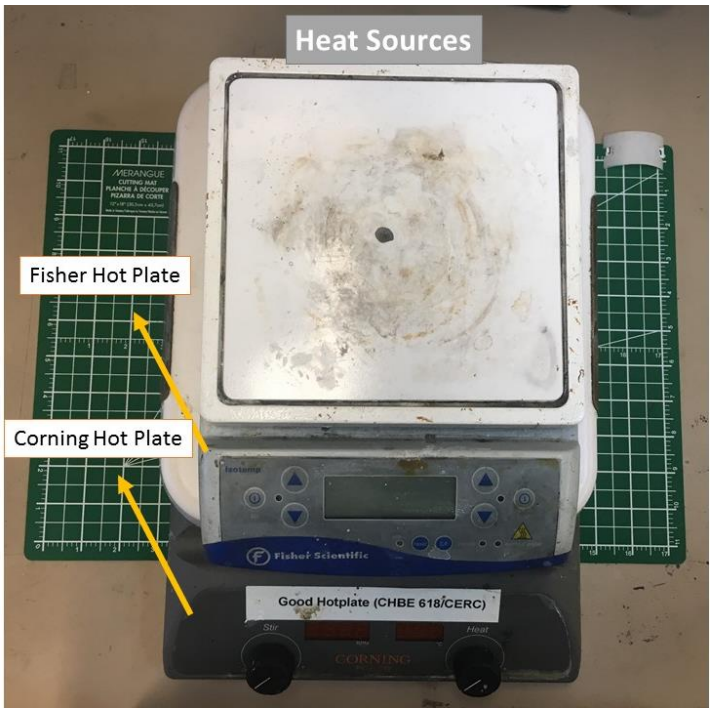

Figure A.6 Heat sources.

A.2 Preparation of EMD and NEMD Electrolyte Solutions

Table A.2 Chemicals used for the electrolysis reactions.

Chemical	Specification
Sulfuric acid	• H_2SO_4 (95.0%; Fisherbrand) ○ Concentration = 17.8 mol L^{-1}
Nitric acid	• HNO_3 (69.0%; Fisherbrand) ○ Concentration = 15.5 mol L^{-1}
Manganese sulfate	• $MnSO_4 \cdot H_2O$ (98%; Anachemia) ○ Molar mass = 169.0 g mol^{-1}
Zinc sulfate	• $ZnSO_4 \cdot 7H_2O$ (99%; Anachemia) ○ Molar mass = 287.6 g mol^{-1}

The following equation was used to calculate volume of stock acid solution required for each concentration of acid solution desired:

$$Vol_{required}\ [mL] = \frac{1000 \times Conc_{desired}\left[\frac{mol}{L}\right] \times Vol_{desired}\ [L]}{Conc_{stock}\left[\frac{mol}{L}\right]}$$

For each electrolysis run, 500 mL of solution was made inside a Kimble® 28014-500 KIMAX® 500 mL Class A volumetric flask with [ST] Glass Pennyhead Stopper. For neutral solutions, the desired salts were poured into the flask and then the appropriate amount of water (Type 1 Milli-Q®) was added and mixed. For acidic solutions, the measured stock acid solution was initially mixed with 200 mL of water. The salts and any remaining amount of water required was then added and mixed. All mixings were performed inside a fume hood.

A.3 EMD and NEMD Electrolysis Operation

The electrolysis cell was assembled, filled with the proper electrolyte solution, and placed inside a fume hood with a cold-water tap. A Solartron Analytical 1470E unit was used for galvanotactic operation (current density range: 0.0075 A cm^{-2} to 0.0125 A cm^{-2}). Synthesis was performed in 5 hour batches.

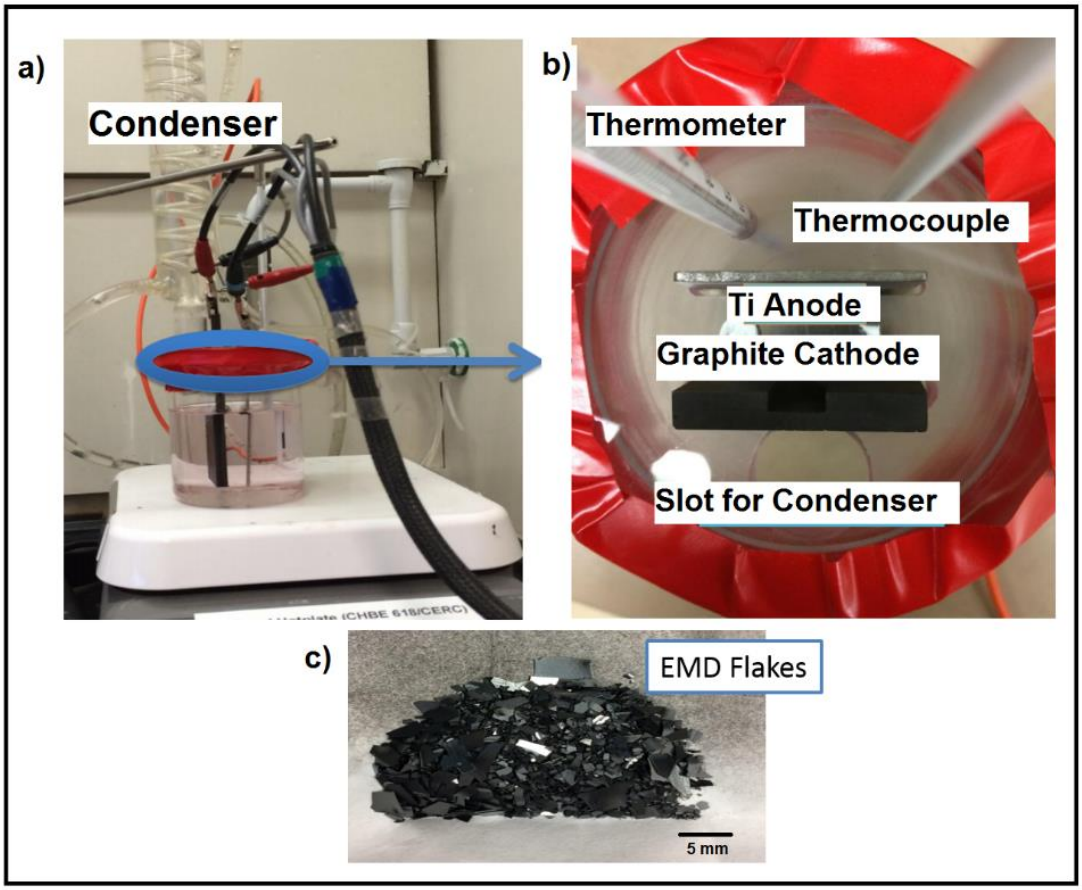

Figure A.7 a) Side view and b) top view of the apparatus; c) the unprocessed EMD product after being chipped off from the titanium anode.

The Ti electrode used to make the EMD was taken out of the hot solution so that the EMD layer deposited on the electrode could instantly crack and separate. The EMD was then easily chipped off from the electrode using a spatula. After a full electrolysis run, the Ti electrode was sanded with a coarse sandpaper (e.g. P50) to get rid of the excess EMD and then polished further using a fine sandpaper (e.g. P120).

The NEMD was formed as loose, fragile chips on top of the Ni electrode and so it could be removed by spraying water on it out of a wash bottle. The Ni electrode could only be used for one electrolysis run due to the rapid corrosion of the electrode.

Both EMD and NEMD were made into powders using an agate mortar and pestle and washed with a vacuum filter. The acidic EMD samples were washed until the EMD/water suspension reached a pH of at least 6 or 7 as tested BDH® litmus papers with pH graduation of 1.0.

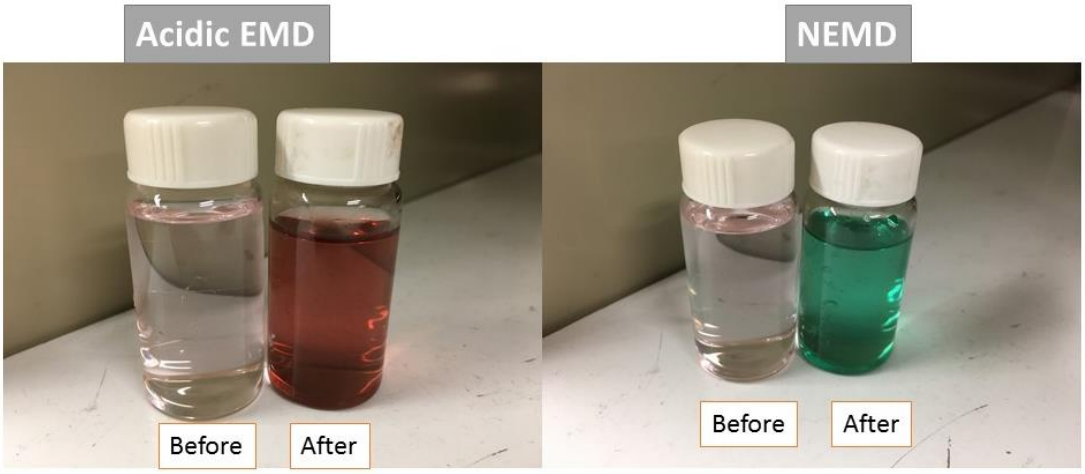

Figure A.8 Electrolysis electrolyte after a typical acidic EMD or NEMD synthesis operation.

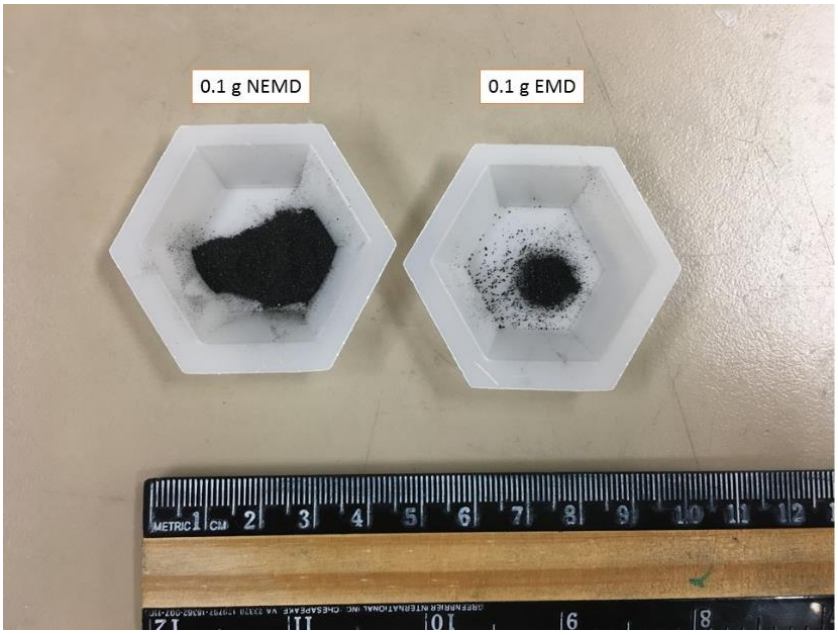

Figure A.9 Equal amounts of processed NEMD powder and typical acidic EMD powder.

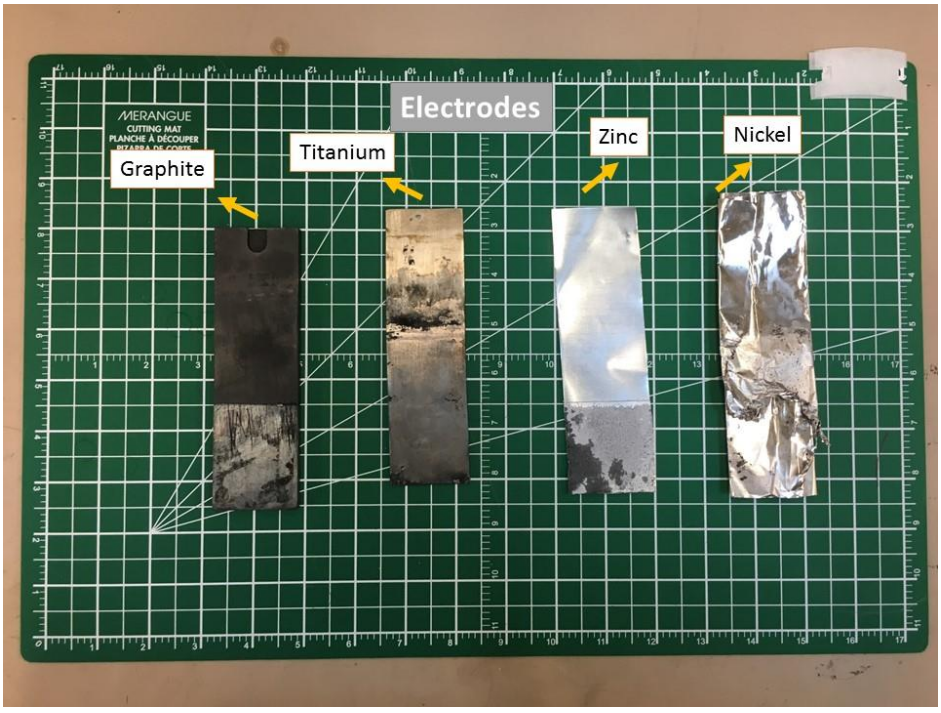

Figure A.10 Electrolysis electrodes after a typical synthesis run.

Appendix B : Chemical Synthesis of MnO_2 (CMD)

B.1 Parts and Hardware

The following table and figure present the details of the cell components used for synthesis of the ramsdellite, hollandite, and birnessite samples. The autoclave hydrothermal vessel and oven heat source was used to synthesize the ramsdellite and hollandite MnO_2 samples. The birnessite MnO_2 was synthesized at ambient pressure inside a Pyrex® beaker on top on the hot plate.

Table B.1 Specifications of parts used for the CMD synthesis.

Part	Specification
Reactor vessel	• Stainless steel autoclave body • 150 mL PTFE reactor chamber
Heat source	• VDO-23i Hydrion Scientific vacuum drying oven • Corning PC-620D hot plate

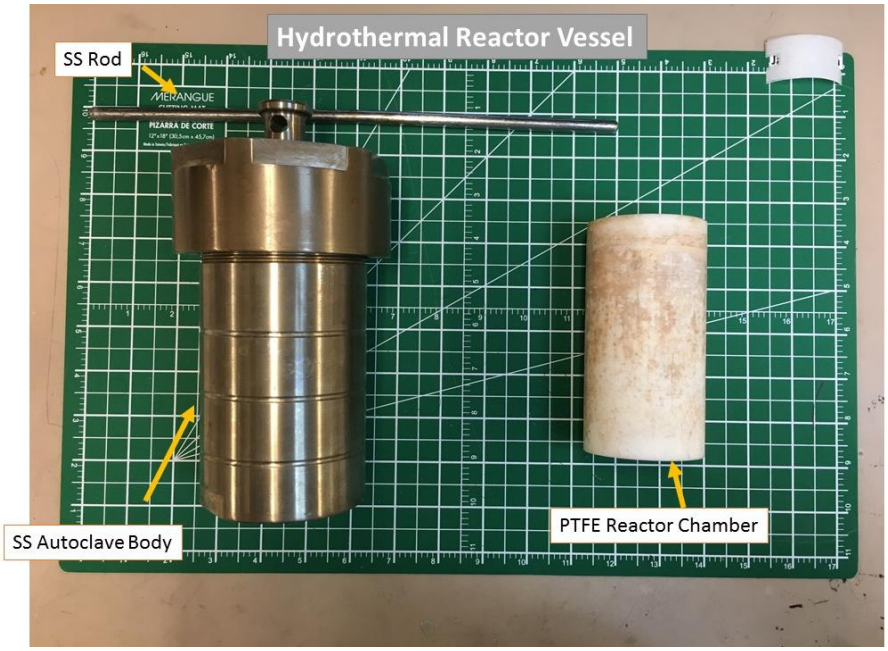

Figure B.1 Hydrothermal reactor vessel.

B.2 CMD Sample Preparation

Table B.2 Chemicals used for the CMD reactions.

Chemicals	Specification
Sulfuric acid	• H_2SO_4 (95.0%; Fisherbrand) ○ Concentration = 17.8 mol L^{-1}
Hydrochloric acid	• HCl (37.0%; Fisherbrand) ○ Concentration = 10.1 mol L^{-1}
Manganese sulfate	• $MnSO_4 \cdot H_2O$ (98%; Anachemia) ○ Molar mass = 169.0 g mol^{-1}
Zinc sulfate	• $ZnSO_4 \cdot 7H_2O$ (99%; Anachemia) ○ Molar mass = 287.6 g mol^{-1}
Potassium permanganate	• $KMnO_4$ (99%; Anachemia) ○ Molar mass = 158.0 g mol^{-1}
Lithium manganese oxide	• $LiMn_2O_4$ (99%; MTI)

For hollandite synthesis, the following procedure was followed:

1. Prepare three stock solutions: 1) 100 mL of 0.01 M manganese sulfate, 2) 100 mL of 0.3 M potassium permanganate, 3) 10 mL of 2 M sulfuric acid.
2. Transfer 90 mL of the 0.01 M manganese sulfate into a 200 mL Pyrex® beaker with a PTFE coated magnetic stirring bar and initiate stirring at 200 rpm.
3. Slowly add 20 mL of the 0.3 M potassium permanganate over a period of 10 minutes.
4. Slowly add 1.5 mL of the 2 M sulfuric acid dropwise over a period of 1 minute.
5. Let the mixture stir for an hour before transferring it into the PTFE reactor chamber.
6. Place the chamber inside the autoclave body, lock the cap manually and then tighten further by using a stainless-steel rod to turn the threated knob on top of the autoclave body
7. Heat content at 120 ^{o}C for 24 hours.
8. Cool content for an hour after reaction, separate settled precipitates from the liquid, and centrifuge the precipitates three times with fresh Type 1 Milli-Q® water using a Champion F-33D unit at 30,000 rpm for 5 minutes.
9. Pass the centrifuged content through a vacuum filter to separate out excess water and dry content at 60 ^{o}C for 24 hours.

For ramsdellite synthesis, the following procedure was followed:

1. Prepare 100 mL of 2.5 M sulfuric acid.
2. Transfer the acid solution into a 200 mL Pyrex® beaker with a PTFE coated magnetic stirring bar and initiate stirring at 200 rpm .
3. Slowly add 5 g of the lithium manganese ($LiMn_2O_4$) salt.
4. Follow steps 5-9 of the hollandite synthesis.

For birnessite synthesis, the following procedure was followed:

1. Prepare two stock solutions: 1) 250 mL of 0.4 M potassium permanganate and 2) 100 mL of 2 M hydrochloric acid.
2. Transfer all the 0.4 M potassium permanganate into a 600 mL Pyrex® beaker with a PTFE coated magnetic stirring bar, initiate stirring at 500 rpm, and heating at 400 ^{o}C on a hot plate.
3. Once the solution starts boiling, add all the 2 M hydrochloric acid dropwise over a period of 10 minute.
5. Boil for additional 10 minutes until a precipitate forms and follow steps 8-9 of the hollandite synthesis.

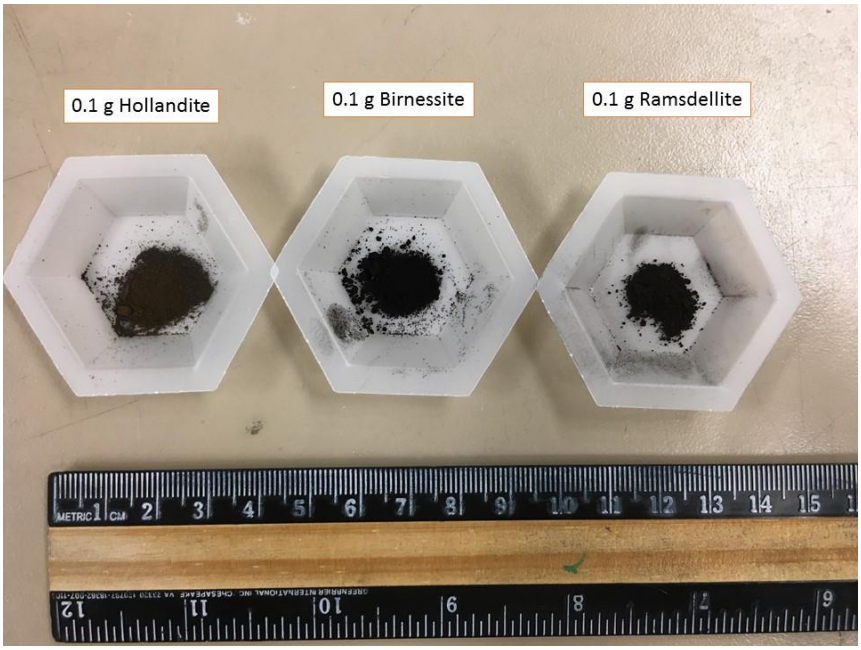

Figure B.2 Equal weights of processed hollandite, birnessite, and ramsdellite MnO_2 powders.

Appendix C : Making of Battery Cells

C.1 Preparations

Table C.1 Required materials for MnO_2/Zn electrodes and cell.

Chemicals	Specification
Potassium hydroxide	• KOH (85%; Fisherbrand) ○ Molar mass = 56.1 g mol^{-1}
Manganese sulfate	• $MnSO_4 \cdot H_2O$ (98%; Anachemia) ○ Molar mass = 169.0 g mol^{-1}
Zinc sulfate	• $ZnSO_4 \cdot 7H_2O$ (99%; Anachemia) ○ Molar mass = 287.6 g mol^{-1}
Carboxymethyl cellulose (CMC)	• CMC (MTI; EQ-Lib-CMC)
Carbomer	• Carbopol® (Lubrizol; Carbopol® 940)
Polyvinylidene fluoride (PVDF)	• PVDF (MTI; EQ-Lib-PVDF)
N-Methyl-2-pyrrolidone (NMP)	• NMP (MTI; EQ-Lib-NMP)
Indium Sulfate	• $In_2(SO_4)_3$ (99.9%; Indium Corp.) ○ Molar mass = 517.81 g mol^{-1}
Polyethylene glycol (PEG)	• Triton X-100 (Sigma-Aldrich)
Polytetrafluoroethylene (PTFE)	• PFTE (60%, Sigma-Aldrich; 9002-84-0)
Styrene-butadiene (SBR)	• 50% SBR glue (MTI; EQ-Lib-SBR)
Graphite	• TIMREX® KS44
Carbon black	• VULCAN® XC72R
Zinc	• Zn (Horsehead; 1239-024)
Zinc oxide	• ZnO powder (ZOCHEM; ZOCO 101)

Preparation of the electrolyte solutions:

- 9 M potassium hydroxide electrolytes were made in one litre batches in 1 L Nalgene® Class B polypropene volumetric flasks.
    - 505 g of potassium hydroxide salt was mixed with ~ 100 mL batches of Type 1 Milli-Q® water inside a fume hood until the solution was complete and well mixed.
- 2 M $ZnSO_4$ electrolytes were made in quarter litre batches in 250 mL KIMAX® Class A volumetric flasks.
    - 144 g of zinc sulfate salt was mixed with ~ 50 mL batches of Type 1 Milli-Q® water inside a fume hood until the solution was complete and well mixed.

- If 0.1 M manganese sulfate additive was required, 4.2 g of manganese sulfate salt was mixed with the zinc sulfate salt before addition of water.

Preparation of the electrode gels and binders:

- 1.7% CMC and 2.1% carbomer gels were made in one litre batches in 32 oz Uline jars (S-12757P).
  - 17 g of CMC powder or 21 g of carbomer powder was added to 1 L of Type 1 Milli-Q® water inside the jar and the solution was mixed at 1100 rpm for 8 hours using a Caframo BDC-2002 stirrer.
- 7% PVDF binders were made in 100 mL batches in 8 oz Uline jars (S-12755P).
  - 7 g of PVDF powder was added to 93 mL NMP solvent inside the jar and mixed at 500 rpm for 2 hours using a PVDF coated stirring bar.

Preparation of 1 M $In_2(SO_4)_3$ solution:

- 104 g of indium sulfate salt was mixed with 70 mL Type 1 Milli-Q® water and shaken until solution was homogenous.

C.2 Preparation of Cathode/Anode Electrodes

Preparation of thick-film cathodes:

1. Mix 8 g of desired manganese dioxide with 2 g graphite powder using a Spex 8000M Mixer/Mill® high-energy ball milling mixer for 10 minutes inside a (5004) tungsten carbide lined grinding vial set.
   a. For smaller batches of cathode mix (< 2 g), manganese dioxide and graphite were mixed using an agate mortar and pestle for 15 minutes.
2. Transfer 1 g of cathode powder mix into a 50 mL Pyrex® beaker and add 1 g of 1.7% CMC and 0.15 g of 50% SBR.
   a. Mix using a glass rod until suspension forms (5 minutes).
3. Add 2 g of additional powder mix and stir.
   a. If required, add small amounts of additional cathode powder mix or 1.7% CMC until a playdough consistency is reached.
4. Spread approximately 0.5 g of paste on 3.5 cm × 2 cm cut pieces of Dexmet 3 Ni 5-077 expanded mesh, covering only 2/3 of the mesh.
5. Roll each electrode to a thickness of 0.5 mm using a Pepetools (Pepe 187.00) flat rolling mill.

6. Press each cathode at 2 MPa for 2 minutes on one side and at 8 MPa for 8 minutes on the other side using an MTI laboratory press (YLJ-24).

Preparation of thick-film anodes:

1. Transfer 5 g zinc into a 50 mL Pyrex® beaker and add 2 g of 2.1% carbomer.
    a. Mix using a glass rod until suspension forms.
2. Add 2.75 g of zinc oxide and mix until incorporated.
3. Add 2 g of additional zinc and mix until incorporated.
4. Add 0.1 g of PEG, 0.22 g of 2 M indium sulfate, and 0.2 g PTFE and mix until incorporated.
    a. If required, add small amounts of additional 2.1% carbomer if mixture is too dry or dry mixture at 60 °C for 15 minutes if mixture is too wet until a playdough consistency is reached.
5. Spread approximately 1 g of paste on 3.5 cm × 2 cm cut pieces of tin-plated Dexmet 3 Brass 10-125 expanded mesh, covering only 2/3 of the mesh.
    a. Dexmet 3 Brass 10-125 expanded mesh pieces were tin-plated using Transene electroless tin plating solution at 80 °C for 15 minutes.

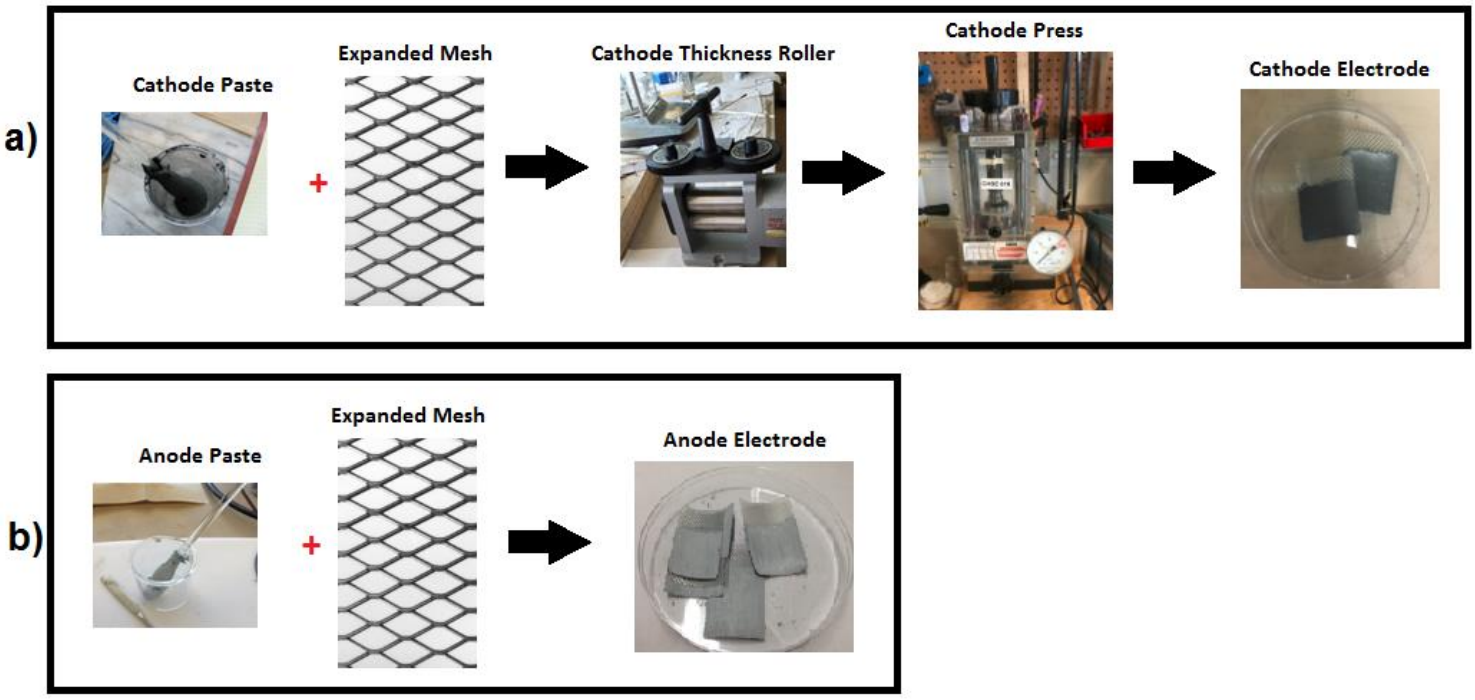

Figure C.1 a) The MnO_2 paste is first spread onto an expanded mesh and then processed through an adjustable thickness roller (0.5 mm) and hydraulic press (8 MPa) to produce the cathode electrode. b) The zinc paste is just spread onto an expanded mesh to produce the anode electrode.

Preparation of thin-film cathode:

1. Mix 0.7 g of desired manganese dioxide with 0.2 g carbon black powder using an agate mortar and pestle for 15 minutes.
2. Transfer the powder mix into a 50 mL Pyrex® beaker and add 1.5 g of 7% PVDF.
    a. Mix using a glass rod until suspension forms.
3. Add 3 g NMP and mix until homogenous suspension is formed.
4. Spread the suspension on a 20 cm x 5 cm piece of substrate slowly using a doctor blade set at thickness of 0.032 mm.
    a. Substrates used: Sigracet® 29BC carbon paper, Torayca® TGP-H-120 carbon paper, or Ni foil (MTI; MF-NiFoil-25u).
    b. Low shear rate is necessary for even coating of the substrate.
5. Let electrode dry overnight at room temperature.

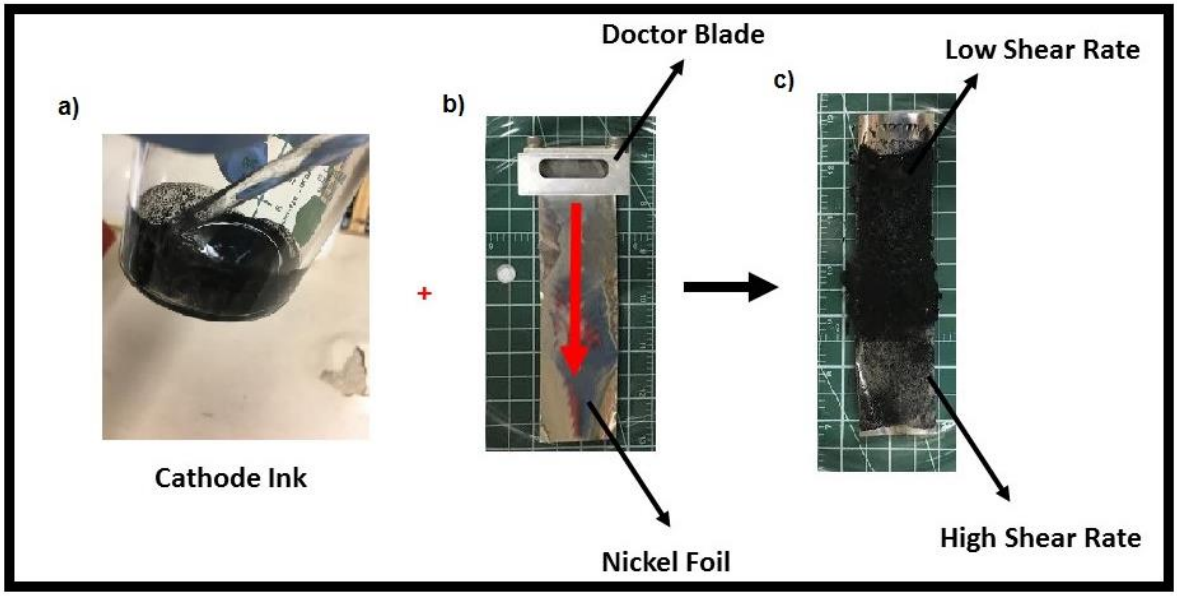

Figure C.2 a) The cathode ink is first produced and spread onto b) a piece of nickel foil or carbon paper using a doctor blade. c) The final product can only be consistent is spread at a low and steady shear rate (1 cm s^{-1}).

Preparation of large battery cells using thick-film electrodes:

1. Place the cathode at the bottom of the cell hardware and cover with 6 drops of 9 M KOH electrolyte using a syringe or transfer pipette.
2. Please 2 pieces of Neptco NWP150 separators (nonwoven polyimide sides facing each other) cut to the shape of the brass metal spacer and spread 8 drops of 9 M KOH on top each separator.
3. Place the anode on top of the separators and spread 6 drops of 9 M KOH.
4. Place an additional cut piece of separator (cellophane layer facing the anode), and place the tin-plated brass metal spacer on top of the anode and two 80 lb/in springs on top of the spacer.
5. Place a rubber o-ring on the groove of the bottom cell hardware and close the cell using the stainless steel enforced plastic cell top using wingnuts on the four corners of the cell.
6. Insert a 1/4-20 X 2'' nickel-plated stainless steel socket cap screw on the side exposing the cathode and a 1/4-20 X 2'' tin-plated brass steel socket cap screw on the side exposing the anode.
    a. All tin-plating were done similarly to how the Dexmet 3 Brass 10-125 was plated.
    b. All nickel-plating were done off-campus

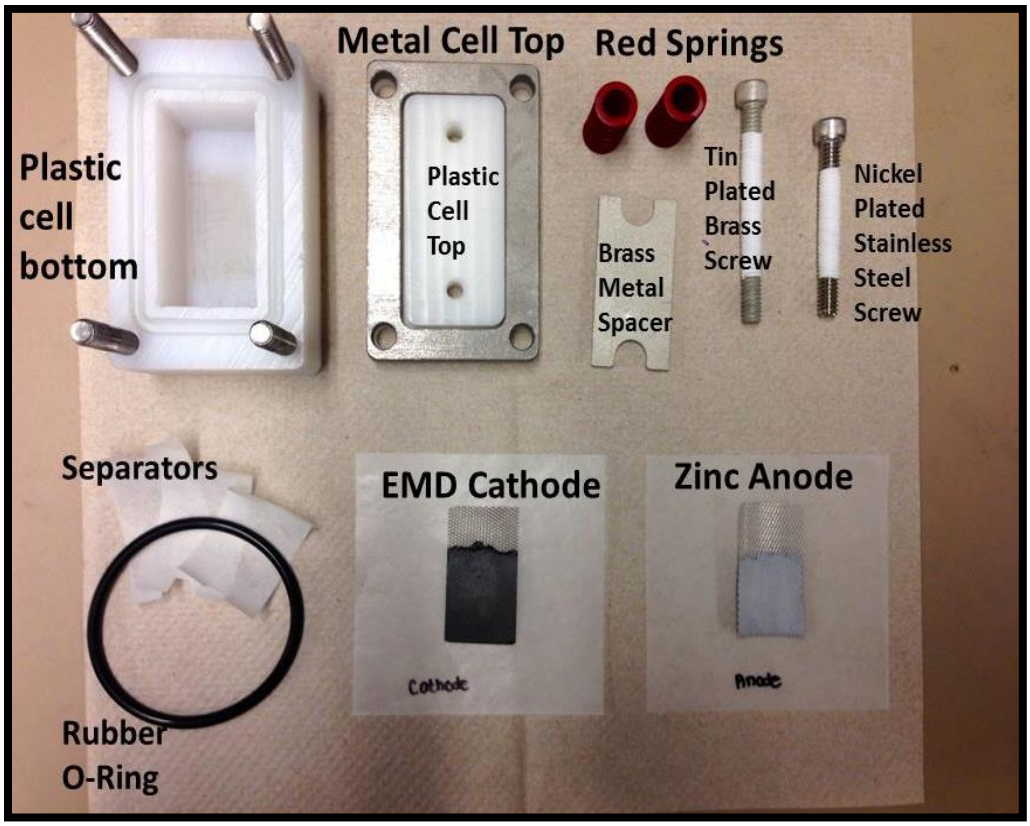

Figure C.3 Various parts of the large thick-film battery cell.

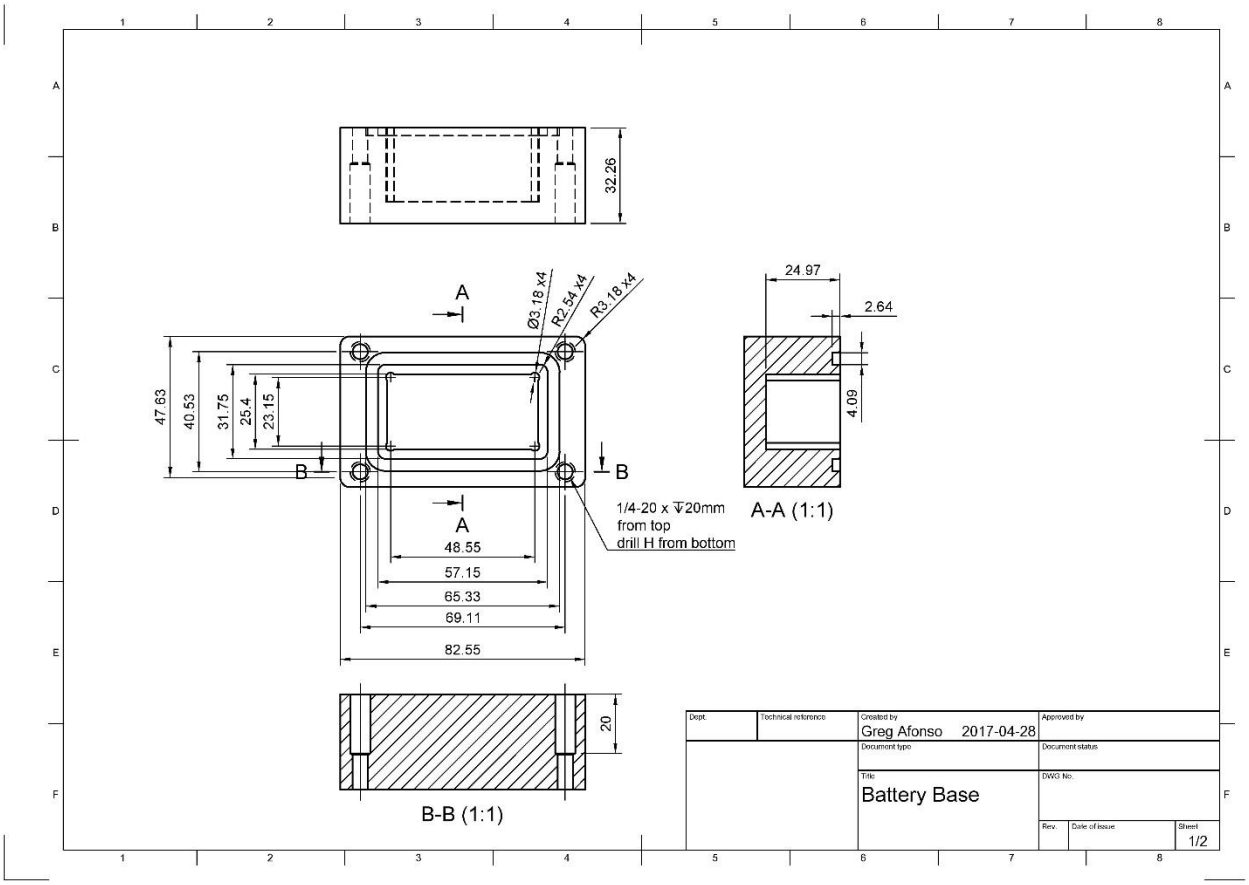

Figure C.4 Design of battery cell body (all measurements are in mm).

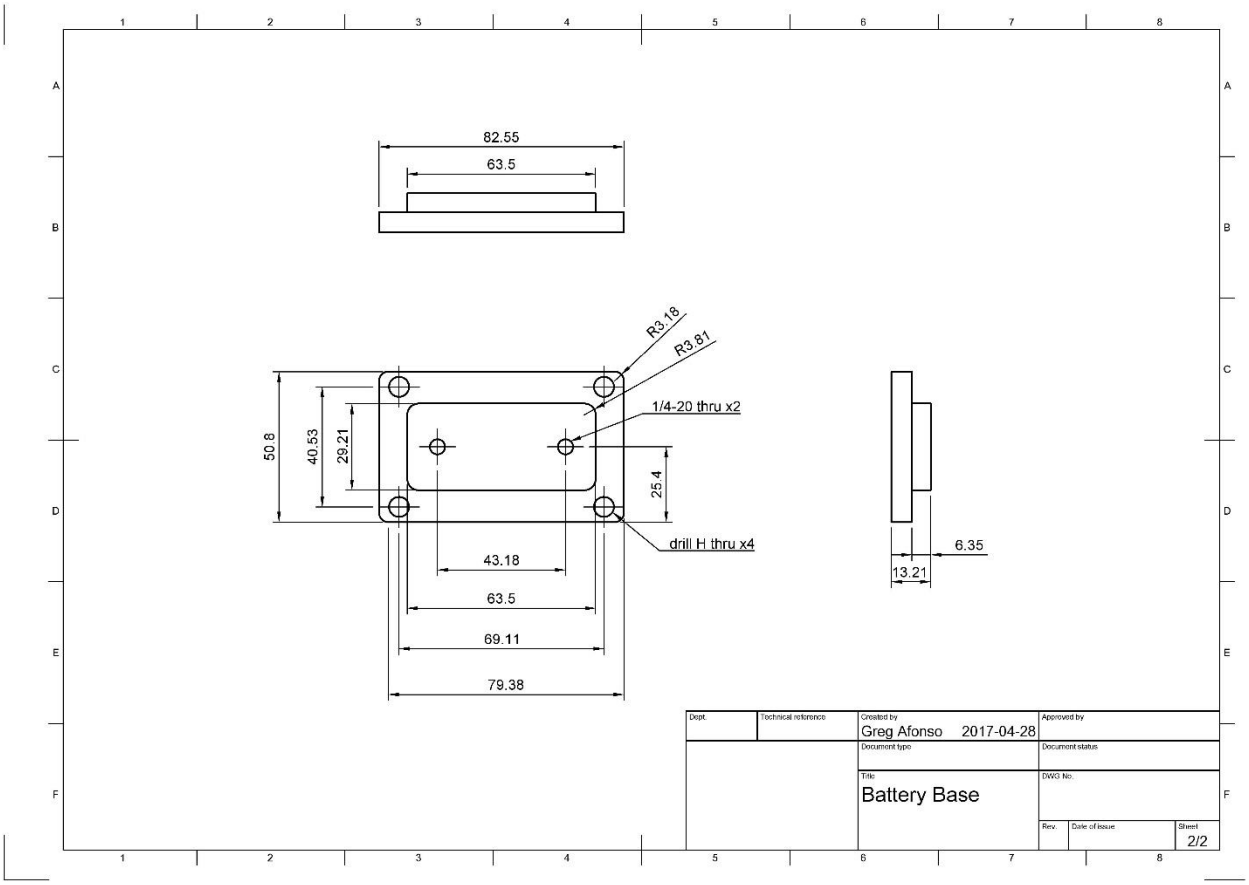

Figure C.5 Design of battery cell top (all measurements are in mm).

Preparation of coin battery cells using thin-film electrodes:

1. Cut one 1.5 cm piece of thin-film cathode and Zn foil (Dexmet) and two 1.7 cm pieces of Neptco NWP150 separators using Mayhew Pro 66004 hole puncher.
2. Place the cathode at the bottom of the bottom cell hardware and cover it with 2 drops of 2 M zinc sulfate electrolyte with a syringe or transfer pipette.
3. Place the 2 pieces of Neptco NWP150 separators (nonwoven polyimide sides facing each other) on top and spread 1 drop of the electrolyte on each separator.
4. Place the anode on top of the separator and place spacer, washer, and top cell hardware in that order.
5. Press the coin cell shut using a hydraulic crimper.

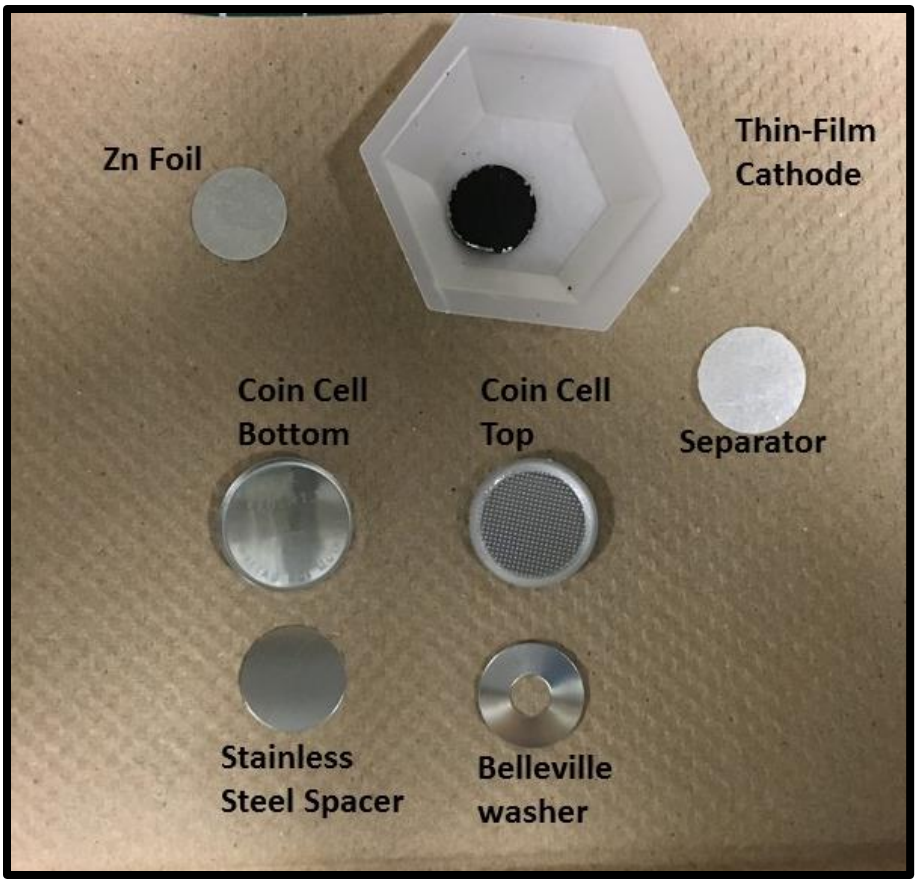

Figure C.6 Various parts of the coin thin-film battery cell.